

Quantum Size Effects in Ultrathin Metallic Islands: a Scanning Tunneling Microscopy/Spectroscopy Study

THÈSE N° 4570 (2009)

PRÉSENTÉE LE 22 DÉCEMBRE 2009

À LA FACULTÉ SCIENCES DE BASE

LABORATOIRE DE PHYSIQUE DES SURFACES

PROGRAMME DOCTORAL EN PHYSIQUE

ÉCOLE POLYTECHNIQUE FÉDÉRALE DE LAUSANNE

POUR L'OBTENTION DU GRADE DE DOCTEUR ÈS SCIENCES

PAR

I-Po HONG

acceptée sur proposition du jury:

Prof. O. Schneider, président du jury
Prof. W.-D. Schneider, directeur de thèse
Prof. H. Brune, rapporteur
Prof. K. Horn, rapporteur
Prof. D. Roditchev, rapporteur



ÉCOLE POLYTECHNIQUE
FÉDÉRALE DE LAUSANNE

Suisse
2009

**Quantum Size Effects in Ultrathin Metallic Islands:
a Scanning Tunneling Microscopy/Spectroscopy Study**

I-Po HONG

2009

To
my mother,
my wife,
and my lovely son.

Abstract

This thesis reports measurements concerning quantum size effects of single crystalline metallic islands by using low-temperature scanning tunneling microscopy (STM) and spectroscopy (STS). Different sample systems are presented in the following chapters.

In chapter 2, several aspects of quantum well states (QWS) of Pb ultrathin islands grown on Si(111) substrate are reported. The differential conductance spectra of QWS can be understood by discrete energy levels with linewidth broadening because of finite quasi-particle lifetime. Using low temperature scanning tunneling spectroscopy, we studied the linewidth of unoccupied quantum-well states (QWS) in Pb islands, grown on Si(111) on two different Pb/Si interfaces, of thicknesses between 7 and 22 monolayers. A quantitative analysis of the differential conductance spectra allowed us to determine the QWS lifetime broadening as a function of energy, showing agreement with 3D Fermi-liquid theory, as well as the electron-phonon (e-ph) contribution between 5 and 50 K. Layer-dependent *ab initio* calculations of the e-ph linewidth contributions are in excellent agreement with the data. Importantly, the sum of the calculated e-e and e-ph lifetime broadening follows the experimentally observed quadratic energy dependence.

In chapter 3, studies investigating reduction of the superconducting gap of ultrathin Pb islands are presented. The energy gap Δ of superconducting Pb islands grown on Si(111) was probed *in situ* between 5 and 60 monolayers by low-temperature scanning tunneling spectroscopy. Δ was found to decrease from its bulk value as a function of inverse island thickness. Corresponding T_c values, estimated using bulk gap-to- T_c ratio, are in quantitative agreement with *ex situ* magnetic susceptibility measurements, however, in strong contrast to previous scanning probe results. Layer-dependent *ab initio* density functional calculations for free-standing Pb films show that the electron-phonon coupling constant, determining T_c , decreases with diminishing film thickness.

In chapter 4, we present preliminary results on single electron tunneling and Coulomb blockade phenomena of metallic islands decoupled from a Ag(111) substrate by dielectric NaCl layers. Using low temperature STM/STS, the geometry of the metallic island can be determined unambiguously and the single electron tunneling properties are characterized. Using orthodox theory of single electron tunneling, the tunneling spectra can be reproduced qualitatively. Despite minor quantitative disagreement between data and simulations, the parameters of the double barrier tunneling junction, including the capacitances and the resistances of both junctions, as well as the residual charge, can be determined.

Key Words : tunneling, scanning tunneling microscopy (STM), scanning tunneling spectroscopy (STS), electron states and collective excitations, quantum wells, lifetime, mesoscopic and nanoscale systems, superconductivity, low- T_c films, electronic transport in mesoscopic systems, Coulomb blockade, single-electron tunneling, quantum dots, electronic structure, resonant tunneling.

Résumé

Cette thèse présente des mesures concernant des effets de confinement quantiques sur des îlots monocristallins par microscopie et spectroscopie à effet tunnel (STM/STS). Différents échantillons seront présentés dans les chapitres suivants.

Dans le chapitre 2, différents aspects des états de puits quantique (QWS) formés dans des îlots ultra-minces de Pb crûs sur un substrat de Si(111) sont rapportés. Les spectres de conductance différentielle des QWS peuvent être compris à l'aide des niveaux discrets de ces états élargis par un temps de vie fini. En utilisant la spectroscopie tunnel à basse température, nous avons étudié la largeur des niveaux inoccupés des QWS d'îlots de Pb, crûs sur Si(111) sur deux interfaces différentes, d'épaisseur entre 7 et 22 monocouches atomiques. Une analyse quantitative des spectres de conductance différentielle nous a permis de déterminer l'élargissement du temps de vie des QWS en fonction de l'énergie, qui est en accord avec la théorie 3D du liquide de Fermi, de même que la contribution électron-phonon (e-ph) entre 5 et 50 K. Des calculs *ab initio* dépendant du nombre de monocouches atomiques de la contribution e-ph au temps de vie des QWS sont en excellent accord avec nos données. La somme calculée de l'élargissement du temps de vie dû aux collisions e-e et e-ph suit la dépendance quadratique en énergie observée expérimentalement.

Dans le chapitre 3, une étude de la réduction du gap supraconducteur d'îlots de Pb ultra-minces est présentée. The gap en énergie Δ d'îlots de Pb a été mesuré *in situ* pour des épaisseurs variant de 5 à 60 monocouches atomiques par spectroscopie tunnel à basse température. Il a été trouvé que Δ diminue depuis sa valeur de volume en fonction de l'inverse de l'épaisseur des îlots. Les valeurs correspondantes de T_c , estimées en utilisant le rapport Δ sur T_c du volume, sont en accord quantitatif avec les mesures de susceptibilité magnétiques *ex situ*, mais en forte opposition avec les résultats précédents de spectroscopie tunnel. Des calculs *ab initio* dépendant du nombre de monocouches atomiques pour des films libres, montrent que la constante de couplage électron-phonon, déterminant T_c , diminue lorsque l'épaisseur du film diminue.

Au chapitre 4, nous présentons des résultats préliminaires d'effet tunnel à un électron et de phénomène de blocage de Coulomb sur des îlots métalliques découplés d'un substrat d'Ag(111) par quelques monocouches atomiques diélectriques de NaCl. En utilisant la

STM/STS à basse température, la géométrie des îlots métalliques peut être déterminée de manière non ambiguë et les propriétés d'effet tunnel à un électron caractérisées. À l'aide de la théorie orthodoxe de l'effet tunnel à un électron, les spectres tunnel peuvent être reproduits qualitativement. Malgré un désaccord quantitatif mineur entre les données et la simulation, les paramètres de la double barrière tunnel, incluant les capacités et les résistances des deux jonctions ainsi que la charge résiduelle sur l'îlot, peuvent être déterminés.

Mots Clés: effet tunnel, microscope à effet tunnel (STM), spectroscopie à effet tunnel, états électroniques et excitations collectives, puits quantiques, temps de vie, systèmes mésoscopiques et nanoscopiques, supraconductivité, films à basse T_c , transport dans les systèmes mésoscopiques, blocage de Coulomb, effet tunnel à un électron, boîte quantique, structure électronique, effet tunnel résonnant.

Abbreviations

Table 1: These are the most used abbreviation in this thesis.

STM	scanning tunneling microscope/microscopy, depending on the context
STS	scanning tunneling spectroscopy
Pb/Si	Pb islands on Si(111) substrate, which includes two cases below:
Pb/Si- 7×7	surface (or interface) of Pb layers growth on Si(111)- 7×7
7×7 interface	as above, see section 2.2
Pb $\sqrt{3}/Si$	surface (or interface) of Pb- $\sqrt{3} \times \sqrt{3}$ layer covers on Si(111)
$\sqrt{3} \times \sqrt{3}$ interface	as above, see section 2.2
Pb/NaCl/Ag(111)	Pb islands on NaCl layers on Ag(111) substrate
Ag/NaCl/Ag(111)	Ag islands on NaCl layers on Ag(111) substrate
$1D$	one dimensional or one dimension,
$2D$, $3D$	analogous to $1D$
2PPE	two photon photoemission
AES	Auger electron spectroscopy
DBTJ	double barrier tunneling junction
DFT	density functional theory
FER	field emission resonances
<i>in situ</i>	conditions for experiments done within UHV chambers
<i>ex situ</i>	not <i>in situ</i>
IPE	inverse photoemission
LDOS	local density of states
LEED	low energy electron diffraction

Table 1: *continued*

NFE	nearly free electron
ML	monolayer
QWS	quantum well states
QSE	quantum size effects
RT	room temperature
SEB	single electron box
SET	single electron transistor
SOC	spin-orbital coupling
UHV	ultra-high vacuum
UPS	ultraviolet photoelectron spectroscopy
d_{ts}	tip-sample distance
e	charge of an electron ($1.602 \cdot 10^{-19} C$)
$e-e$	electron-electron
$e-ph$	electron-phonon
Γ_{e-e}	part of linewidth due to electron-electron scattering
Γ_{e-ph}	part of linewidth due to electron-phonon scattering
$E_{F,s}$	Fermi level of the sample
$E_{F,t}$	Fermi level of the tip
$E_{vac,s}$	vacuum level of the sample
$E_{vac,t}$	vacuum level of the tip
k_B	Boltzmann's constant ($8.617 \times 10^{-5} eV \cdot K^{-1}$)
I_t	tunneling current
ϕ_s	work function of the sample
ϕ_t	work function of the tip
ρ_s	density of states of the sample
ρ_t	density of states of the tip
T_c	superconducting critical temperature
V_T	tunneling bias voltage

Contents

Abstract	I
Résumé	III
Abbreviations	V
Table of Contents	i
List of Figures	v
List of Tables	vii
1 Introduction and STM theory	1
1.1 Overview of the thesis	3
1.2 Brief introduction of STM and STS	4
1.2.1 Brief theory of STM and STS	4
1.3 Experimental setup	7
1.3.1 The STM	7
1.3.2 Experimental considerations for performing STS	8
2 Quantum Well States in Pb islands grown on Si(111)	11
2.1 Introduction to QWS: theory and review	12
2.2 Sample preparation and STM images of Pb islands	13
2.2.1 Pb/Si(111)- 7×7	14
2.2.2 Pb/Pb- $\sqrt{3} \times \sqrt{3}$ /Si(111)	16
2.3 QWS in Pb islands: STS data and modeling	18
2.3.1 STS results	18

2.3.2	Modeling and fitting of the dI/dV spectra	20
2.3.3	Discussion on the peak lineshape	22
2.4	Energy levels of the QWS	25
2.4.1	Band dispersion	26
2.5	Decay processes of QWS in metallic thin islands	27
2.5.1	Linewidth analysis	27
2.5.2	Scattering channels	29
2.5.3	Comparison of the Γ_{e-e} with previous work and discussion	32
2.6	Conclusions and outlook	34
3	Superconductivity in Ultrathin Pb Island Grown on Si(111)	37
3.1	Introduction to superconductivity in thin films	38
3.1.1	Earlier studies of size effects on superconductivity	38
3.1.2	Recent studies of size effects on superconductivity	39
3.2	STM images of superconducting Pb islands	40
3.3	Superconductivity in Pb islands grown on Si(111)	42
3.3.1	Results	42
3.3.2	Modeling of the conductance spectra	44
3.3.3	DFT calculations for ultrathin Pb films	46
3.3.4	QSE on the superconductivity in Pb ultrathin islands	47
3.4	Conclusions and outlook	51
4	Metallic Coulomb Islands	53
4.1	Introduction to Coulomb blockade and Coulomb staircase	55
4.2	The orthodox theory of Coulomb islands	57
4.3	Experimental details and STM images	63
4.3.1	Sample preparation and STM images	63
4.3.2	Spectra of the NaCl surfaces	65
4.4	STS of metallic Coulomb islands	66
4.4.1	From Coulomb blockade to Coulomb staircase	66
4.5	Conclusions and outlook	72
	Appendices	75
A	Table of Useful Parameters	75

CONTENTS	iii
<hr/>	
Bibliography	77
Curriculum Vitae	89
List of Publications	91
Acknowledgements	93

List of Figures

1.1	Schemetic view of the basic principle of STM	5
1.2	Schemetic view of our STM head	7
2.1	STM images of 7×7 interfaces, wetting layer (WL), and Pb islands on it . .	13
2.2	STM images of Pb islands on 7×7 interfaces	14
2.3	Schematic profile of Pb islands on the two interfaces	16
2.4	STM images of Pb- $\sqrt{3} \times \sqrt{3}$ layer on Si(111)	16
2.5	STM images of Pb islands on $\sqrt{3} \times \sqrt{3}$ interfaces	17
2.6	STS featuring QWS of Pb islands on both 7×7 and $\sqrt{3} \times \sqrt{3}$ interfaces . . .	19
2.7	Schematic energy diagram of the tunneling junction of the QWS system. . .	20
2.8	Simulated DOS and dI/dV spectra compared with STS data	21
2.9	Schematic diagram of Fermi sphere with confinement of electrons to a quan- tum well	23
2.10	Schematic diagram of density of states in various dimensions	24
2.11	QWS energy levels as a function of thickness	25
2.12	Extracted band dispersion and phase from the analysis of phase accumula- tion model.	26
2.13	Extracted reflectivity of the Pb-Si interface.	28
2.14	Inverse quasi-particle lifetime as a function of energy	29
2.15	DFT calculated QWS energy and Γ_{ee}	30
2.16	Comparison of experimental results and DFT calculations of Γ_{e-e}	31
3.1	A large Pb island grown on 7×7 interface	40
3.2	STS featuring superconducting gap of Pb islands on both interfaces	42

3.3	Raw dI/dV spectra and background correction.	43
3.4	Energy of phonon peaks extracted from the dI/dV spectra featuring superconducting gap.	44
3.5	Calculated DOS and $e-ph$ coupling constant of ultra-thin Pb films	47
3.6	Comparison of superconducting gap and deduced T_c with other works	48
4.1	Sketch and electric circuit of a Coulomb blockade system.	55
4.2	Depicted scheme of the the coulomb island in a DBTJ.	58
4.3	Using orthodox theory to simulate the tunneling spectra of Coulomb islands.	62
4.4	STM images of NaCl layers on Ag(111).	63
4.5	STM images of Pb islands on NaCl/Ag(111).	64
4.6	dI/dV spectra of a 2 ML NaCl layer on Ag(111).	66
4.7	Evolution of a Coulomb blockade to a Coulomb staircase with experimental STS data and simulation.	67
4.8	Coulomb staircase showing features of both C_{sub} and C_{tip} with varying Q_0 .	69
4.9	$C_{tip}(z)$. Change C_{tip} by varying tunneling current.	70

List of Tables

1	Abbreviation	V
2.1	Extracted parameters of various scattering channels contributing to quasi-particle lifetime	33
A.1	Useful Parameters and Values	75

Introduction and STM theory

Understanding the physics of metallic thin films and nanostructures with reduced size and dimension is important for particular aspects of industrial and scientific interests. When the size of the metal is reduced to the size comparable to the Fermi wave length of the electrons, the physics describing the dynamics is dominated by quantum mechanics instead of classical physics.

From the industrial point of view, the fabrication of the electronic circuits is approaching to the quantum regime. During the last decades, the world has witnessed the miniaturization of electrical circuits in the chips, or of unit memory in the magnetic storage devices. Strategies of miniaturization can be classified into two groups, "*top-down*" and "*bottom-up*". With the *top-down* approach, the smallest size of the structures of state-of-the-art lithography manufactured chip in the semiconductor industry is 28 nm at the moment.¹ In the magnetic storage devices industry, the storage density has reached more than 100 Gb per square inch [1]. With such a small structure and high storage density in the devices, soon the materials are going to reach the classical limits and entering the quantum regime [2]. In order to advance the limits, full comprehension of the physics for small structures is desperately needed.

The *bottom-up* approach is mainly demonstrated in the scientific research field. From the scientific point of view, the spectrum of electronic eigenstates of nanostructures consists of discrete energy levels, contrary to the continuous spectrum of its bulk counterpart. This separation of the energy spectrum causes the change of many physical and chemical

¹http://www.fabtech.org/news/_a/tsmc_touts_gate_last_hkmg_for_28nm_low_power_applications/

properties relative to bulk values. In the past, a direct study of these eigenstates has been impossible because of technical limitations, but this is no longer the case in the recent decades. In the course of the emergence of nanoscience and nanotechnology, researchers have discovered ways to build devices with very small size to study the quantum phenomena.

Since the invention of STM in 1982, the studies performed by scanning tunneling microscopy (STM) and atomic force microscopy (AFM) have shown that researchers have the ability to move atoms and construct nanostructures. Such an ability was highlighted by the studies by D. M. Eigler *et al.* in 1990, in which they moved Xe atoms to write letters [3]. This kind of ability enables us to test quantum mechanics theories in various boundary conditions. For example, one can make nanostructures of magnetic atoms. M. F. Crommie *et al.* [4] approached two magnetic atoms on a metal surface and observed the disappearance of Kondo effect because of the binding of the two atoms. A. J. Heinrich *et al.* [5] assembled spin chains of magnetic atoms on an insulating film and could clearly explain the phenomenon by a simple spin Hamiltonian from the Heisenberg model.

Another simpler way of the *bottom-up* approach is to utilize the preferences of nature to assemble nanostructures, in what is known as "*self assembly*". Regarding the self assembly of molecules, the construction of supermolecules has been demonstrated mainly on metal surfaces, which are described in the literature [2, 6]. With respect to the self assembly of atoms, the construction of nanoparticles or nanoscale islands with specific geometries has been observed as well.

This report is about the quantum phenomena of self-assembled metallic islands. Examples are the quantum size effects (QSE) of ultrathin metal films (chapter 2), how this QSE affect superconductivity (chapter 3), and Coulomb phenomena in small isolated islands (chapter 4).

As early as in 1960, Richard Feynman predicted ² the birth of nanoscience in his visionary talk. We have witnessed that his predictions come true one by one in recent decades. "There's plenty of room at the bottom", Feynman said. Indeed, there is a huge "playground" of quantum mechanics in the field of nanostructures as well.

Following Feynman's idea, in this thesis we use low-temperature STM to elucidate

²The talk is published in February 1960 in the Caltech alumni magazine "Engineering and Science"

physical properties of metals with reduced dimensions or reduced sizes. The aim of this work is to make a valuable contribution to the understanding of the rules of the "play-ground" of quantum mechanics.

1.1 Overview of the thesis

In chapter 2, we discuss the various aspects of quantum well states of Pb ultrathin islands grown on Si(111) substrate. Using scanning tunneling microscopy and scanning tunneling spectroscopy, we studied at temperatures of $T = 5$ K and 50 K the quasiparticle linewidth of quantum well states (QWS) in Pb nanocrystals on Si(111)- 7×7 and on Pb- $\sqrt{3} \times \sqrt{3}$ /Si(111) surfaces. An analysis of the measured linewidth within a model accounting for the tunneling process and electron reflection at the Pb-Si and Pb-vacuum interfaces, allows us to determine quantitatively the QWS quasiparticle lifetime, including defect and interface scattering, electron-phonon and electron-electron interaction.

In chapter 3, we studied the reduction of superconductivity in the ultrathin Pb island as a function of thickness. The differential conductance (dI/dV) spectra, obtained at 4.6 K and 3.0 K, clearly show the evolution of the superconducting gap as a function of film thickness. The results are discussed and compared to recent transport, magnetic susceptibility and also STS measurements, in order to clarify contradictory results in the literature. By performing layer-by-layer *ab initio* calculations, we found for thin layers a similar behavior of T_c , which is caused by a thickness dependent decrease of the electron-phonon coupling.

In chapter 4, we present small metallic islands decoupled from Ag(111) by NaCl layers studied by STM. The double barrier tunneling junctions are formed with the existence of the dielectric NaCl layers and the vacuum barrier. Metallic islands inside the double barrier show single electron tunneling and Coulomb blockade phenomena. The measured spectra can be explained by semi-classical orthodox theory. Overall, with the local probe capability, we believe this is a promising system with abundant physics to be discovered in it.

1.2 Brief introduction of STM and STS

The development of the scanning tunneling microscope (STM) by Binnig and Rohrer in 1982 opened up a new field in surface science, permitting a real space investigation of small structures atomically. The nomination of the Nobel Prize in 1985 only three years after their first invention explains the importance of this technique. The imaging mechanism of the STM is based on the quantum mechanical tunneling effect which enables electrons to cross a vacuum barrier between the tip and the sample. By applying a bias voltage and measuring the tunneling current, spatial resolution of sub-Angstrom in the z direction is achieved because the current is exponentially related to the distance between the tip and sample. The lateral resolution of the STM is limited by the tip radius and electronic structure of the tip. In a fairly good condition, lateral resolution of 1 \AA is regularly obtained. With this amazing capability, real space three dimensional images of individual atoms and molecules are obtained efficiently.

The capabilities of STM can be briefly divided into three categories: **1. Spatial resolution.** The first and most amazing ability. **2. Spectra on a local scale.** One can detect the electronic structure of the object in combination with its spatial resolution. **3. Manipulation.** One can use the tip as a hand to move atoms to construct structures. The first two abilities were fully used in this report.

After nearly three decades of development, STM has now become a mature technique for the field of nanoscience and nanotechnology. There exist already a selection of books and review articles in the literature, describing both technical aspects and scientific subjects, *e.g.* [7–13].³

1.2.1 Brief theory of STM and STS

The basic principle of STM is based on the tunneling current between the metallic tip and the conductive sample. If one applies a small bias voltage between the two electrodes, a flow of tunneling current goes through the vacuum barrier between the two electrodes. The value of the current, follows an exponential relation as a function of the distance

³The main part of the thesis concerning STM theory follows descriptions of the recent book of C.J. Chen [7]. For the theory of tunneling, E.L. Wolf's book [12] offers solid background. For the details of the experimental setup and considerations, M. Ternes's thesis [13] gives thorough descriptions and is referred to a lot in this report.

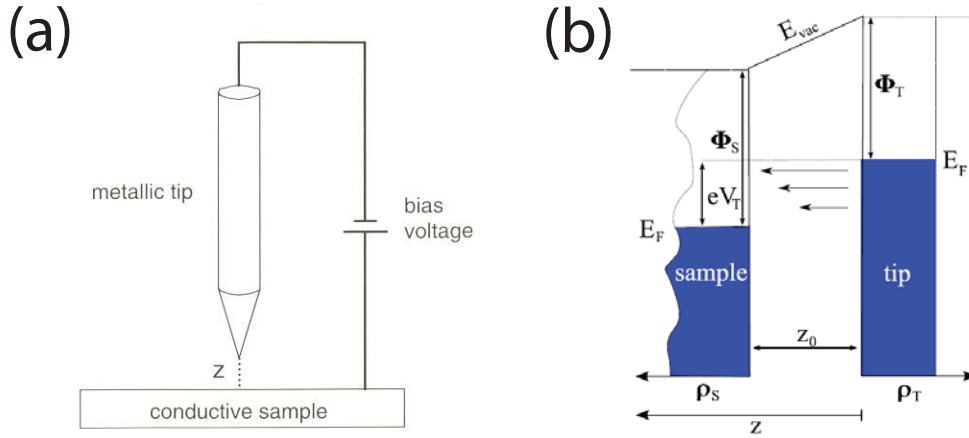


Figure 1.1: (a) Schematic view of basic principle of STM. (b) Schematic view of tunneling process. The DOS of the tip (ρ_T) is assumed to be flat, thus in this case, the DOS of the sample (ρ_S) is obtained through tunneling spectra. Tunneling bias voltage V_T is applied in the junction to help electron tunneling through the trapezoidal potential barrier. Source of the picture(a): [14], and (b): [13].

between the tip and sample (z), as shown in Eq. (1.1). One popular way to obtain the topography of the surface is the According to the relation between the current and the tip-sample distance ($I(z)$), one have a precise measure of the variation of z by monitoring the current value. In a popular way called "constant current mode", one keep the distance constant through the course of scanning by keeping the current constant. The tip-sample distance is controlled by properly controlling the deformation of the piezo tube which is driven a supplied voltage. Using the feedback electronics for the response of piezo voltage in order to keep the current constant, one obtains the topography image of the surface by recording the voltages applied to the piezos [7].

$$I(z) = I(0) e^{-2\kappa z}, \text{ where} \quad \kappa = \frac{\sqrt{2m(U - eV_T)}}{\hbar} \quad (1.1)$$

In the equation above, U represent a potential barrier height.

By leaving the feedback loop open, keeping the tip at a constant location and height, and by measuring the response of the tunneling current by adjusting the bias voltage, one can have access to the electronic structure of the sample. The theory of tunneling is already well established [12]. We will introduce briefly the theory used in this report in the following text. ⁴

Using Bardeen's theory of tunneling in the $1D$ case, the tunneling current as a function

⁴ The formalism here mainly follow [7, 13, 15].

of bias voltage is given in Eq. (1.2).

$$I_T(V_T) = \frac{4\pi e}{\hbar} \int_{-\infty}^{\infty} \left[\rho_s(\epsilon) \rho_t(\epsilon - eV_T) [f(\epsilon) - f(\epsilon - eV_T)] \times |M(\epsilon)|^2 \right] d\epsilon \quad (1.2)$$

, where $f(\epsilon)$ is the Fermi distribution function

$$f(\epsilon) = \frac{1}{1 + \exp\left[\frac{\epsilon}{k_B T}\right]} \quad (1.3)$$

Three factors determine the value of tunneling current: DOS of the sample (ρ_s), DOS of the tip (ρ_t), and the tunneling matrix element (M). It is assumed that the DOS of the tip is constant around the Fermi level for the PtIr tips we used in the measurements of the tunneling spectra. The tunneling matrix M is a complicated factor and will be discussed later. Still, for small bias voltage ranges, the tunneling matrix can be assumed to be constant because the energy dependance of the tunneling matrix can be neglected in the case of small $k_B T$ and small V_T . One can simplify Eq. (1.2) and reproduce the dI/dV as Eq. (1.4).

$$\frac{dI}{dV}(V_T) = \frac{4\pi e^2}{\hbar} \rho_s(E_F + eV_T) \rho_t(E_F) |M|^2 \quad (1.4)$$

In this case, the dI/dV is approximately proportional to the DOS of the sample (ρ_s). Therefore the DOS of the sample can be determined by measuring the tunneling spectra.

However many STS experiments employ an energy scale as large as $\pm 2\text{ eV}$ where the energy dependence of tunneling matrix can not be overlooked. If one assumes a constant potential barrier, the tunneling current can be written as Eq. (1.5) [7].

$$I_T(V_T) = \frac{4\pi e}{\hbar} \int_{-\infty}^{\infty} \left[\rho_s(E_F + \frac{1}{2}eV_T + \epsilon) \rho_t(E_F - \frac{1}{2}eV_T + \epsilon) [f(\epsilon) - f(\epsilon - eV_T)] \times |M(0)|^2 \times \exp\left(\frac{\kappa_0 \epsilon s}{\phi_{avg}}\right) \right] d\epsilon, \text{ where} \quad (1.5)$$

$$\kappa_0 = \frac{\sqrt{2m\phi_{avg}}}{\hbar} \quad (1.6)$$

Here, ϕ_{avg} is a common work function for both electrodes related to the average of $E_{F,tip}$ and $E_{F,sample}$.

In advance, one can assume a trapezoidal potential barrier to represent the vacuum between the two electrodes, and yield the tunneling current as in Eq. (1.7). The real potential barrier should be more trapezoid with rounded edges [12, 16], still we employed

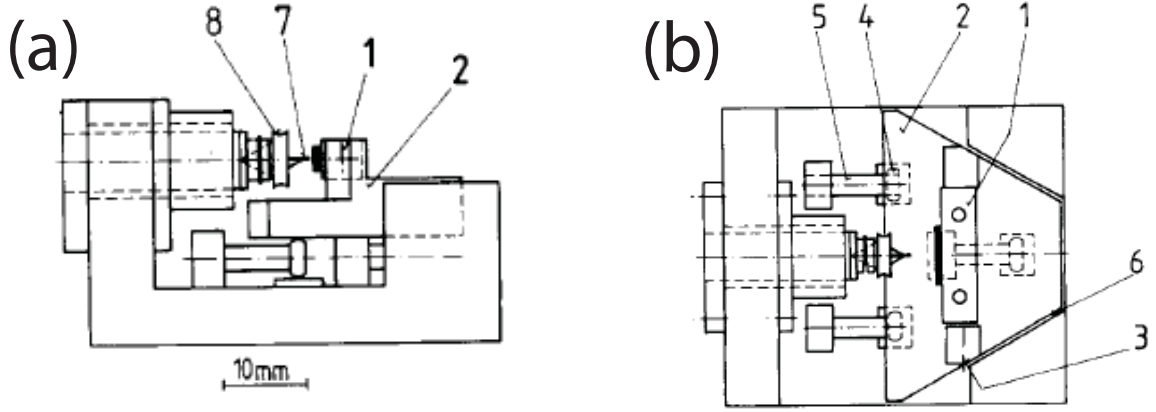


Figure 1.2: (a) Schematic side view of the STM head we use. (b) Schematic top view. The picture is reproduced from [17]. The numbers indicate the various parts. Few important elements: (1) sample holder, (2) slider for coarse approach, (3) screw to fix the sample holder, (4) rings attach to the three piezo tubes, (5) the three piezo tubes for coarse motion, (7) tip, and (8) tip holder.

Eq. (1.7) for our further analysis for its simplicity.

$$I_{wkb}(V_T) = \frac{4\pi e}{\hbar} \int_{-\infty}^{\infty} \left[\rho_s(\epsilon) \rho_t(\epsilon - eV_T) [f(\epsilon) - f(\epsilon - eV_T)] \times \exp \left(-\frac{2}{\hbar} \int_0^d \text{Re} \left\{ \sqrt{2m[\Phi_{avg} - \epsilon + (1 - \frac{z}{z_0})eV_T]} dz \right\} \right] d\epsilon \right]. \quad (1.7)$$

Here we assume both electrodes have the same work function Φ_{avg} . The schematic energy diagram of Eq. (1.7) is shown in Fig. 2.7. By using Eq. (1.7), we successfully simulated and fit the conductance spectra of Pb thin films featuring quantum well states. For the details, see Fig. 2.8 and the associated text.

1.3 Experimental setup

1.3.1 The STM

The measurements were performed in a homebuilt scanning tunneling microscope (STM) operated at 3.0 K, 4.6 K and at 50 K in ultrahigh vacuum (UHV) using cut PtIr tips. Design and performance of the STM is described by R. Gaisch *et al.* [17]. The STM head is represented in Fig. 1.2. The STM system is equipped with an inner and an outer dewar, with the outer filled with liquid nitrogen for thermal radiation screening. The STM head is attached to the inner dewar without a suspension to ensure thermal conductance. We operated the STM at 4.6 K and 3.0 K when filled the inner dewar with liquid helium, and at 50 K when the inner dewar is filled with solid nitrogen. 3.0 K is obtained by pumping

the inner dewar filled with liquid helium, and 50 K is obtained by pumping the inner dewar which transform the liquid nitrogen inside the dewar into solid nitrogen.

1.3.2 Experimental considerations for performing STS

dI/dV measurement were performed with an open feedback loop using the lock-in technique with modulation voltage ranging from $0.2 - 10 mV_{pp}$ at $300 - 1400 kHz$ frequency, and with tunneling current ranging from $100 pA$ to few nA .

In certain cases, it is necessary to calibrate the lock-in dI/dV to match the numerical differential dI/dV (calculated from measured $I(V)$). With this calibration, we can compare both measured $I(V)$ and dI/dV with their simulated counterparts simultaneously and still utilize the higher signal-to-noise ratio of lock-in dI/dV . We noted the calibrated dI/dV with real units ($1/G\Omega$) in the graph instead of arbitrary units.

The quality of the STS measurement relied on the energy resolution we have in the STM system. There are several techniques we employed to improve the energy resolution. Before further discussions, we assumed that vibration noise is well isolated and the electric grounding is done properly. The compactness and the rigidity of the STM head affect the overall performance as well. In this sense, the STM system we used is very powerful. Below are some important aspects we take into consideration.

We operated the STM at $T = 3.0 K$, $4.6 K$ or $50 K$. With finite temperature, one has to consider the thermal broadening with the factor $3.2 k_B T$ in a behavior following the Fermi-Dirac function (Eq. (1.3)). Mathematically, it can be considered as a convolution of ideal LDOS and a gaussian peak with full width at half maximum (FWHM) of $3.2 k_B T$ [13]. Equally, we can also treat it by adding the Fermi function in the integration of calculating the tunneling current as shown in Eq. (1.7).

By using the lock-in technique, we add a voltage modulation on the bias voltage signal. The response to the tunneling current is measured via a lock-in amplifier at the same frequency as the modulation. As a drawback of the lock-in technique, the modulation voltage is also a source of broadening which limits the energy resolution by the value of the modulation amplitude V_m . The additional broadening introduced by the bias voltage modulation can be taken into account by a proper convolution as shown in Eq. (1.8-1.9) [13, 18]. In Eq. (1.8), $I_{+mod}(V_T)$ shows the ideal tunneling current $I(V_T)$ convoluted with

a sinusoidal modulation. After the trivial calculations described in [13], the differential of Eq. (1.8) leads to Eq. (1.9). In Eq. (1.9), the modulation broadening is taken into account by convoluting the ideal spectra $dI/dV(V_T)$ with a hemisphere spectra having a radius of the modulation amplitude V_m . One consider F_m as the *instrumental resolution function* [18].

$$I_{+mod}(V_T) = \frac{1}{\pi} \int_{-\pi}^{\pi} I(V_T + V_m \cdot \sin(\omega\tau)) \cdot \cos(\omega\tau) d\tau \quad (1.8)$$

$$\begin{aligned} \frac{dI}{dV}_{+mod}(V_T) &= \left(\frac{dI}{dV} \otimes F_m \right)(V_T) \\ &= \frac{2}{\pi V_m^2} \int_{-V_m}^{V_m} \frac{dI}{dV}(V_T + \epsilon) \sqrt{V_m^2 - \epsilon^2} d\epsilon \\ &= \frac{2}{\pi} \int_{-1}^1 \frac{dI}{dV}(V_T + v \cdot V_m) \sqrt{1 - v^2} dv . \end{aligned} \quad (1.9)$$

Here we introduce a non-unit fraction v ($v = \epsilon/V_m$) for convenience of integration.

Another problem caused by the introduction of the modulation is that there is an additional oscillation noise in the tunneling current caused by crosstalk capacity resonating at the modulation frequency. The crosstalk capacitance, with a value around $2 pF$, mainly comes from the capacitance between the wires of tunneling current (as well as bias voltage) and the grounding/shielding tubes. Fortunately, one can filter this noise by the phase difference between the noise and the signal. We achieved the filtering by compensating the tunneling current signal with an additional sinusoidal signal at the modulation frequency that is 90° phase shifted with respect to the modulation signal. Technically, a phase shifter device can serve for this task, or a simple device supplying a 90° phase shift is sufficient as well.

However, if we intend to measure small features like superconductivity properties with spectral features not limited by thermal broadening, resolution below $1 meV$ is required. In this case, radio frequency noise (RF) has to be taken into account. RF noise is demonstrated [19] as a huge broadening factor for measuring the tunneling spectra of the superconducting gap if it is not properly filtered.

One solution for the RF noise is to keep the STM system within a Faraday cage. The conductor of the cage should be thick enough and any holes should be significantly smaller than the radiation's wavelength. This is a difficult task due to practical concerns in most

systems. On the other hand, one can filter the noise by putting a RF frequency filter in the wires. We can put a filter in the wire of the bias voltage, but unfortunately we could not do it for the tunneling current. However, the effects of the RF noise on the tunneling current wire is expected to be small because the wire is short under the exposure to RF noise before attached to the preamplifier. The remaining RF noise voltage present in the tunneling junction is modeled by an additional convolution to the ideal dI/dV . We assumed a Gaussian distribution for the RF noise. We treat this Gaussian broadening by Eq. (1.10) [20].

$$\begin{aligned} \frac{dI}{dV}_{+RF}(V_T) &= \int_{-\infty}^{\infty} \frac{1}{s\sqrt{\pi}} \exp\left[-\frac{(u - V_T)^2}{s^2}\right] \frac{dI}{dV}(u) du \\ &= A \cdot \int_{-\infty}^{\infty} \exp\left[-\frac{u^2}{2}\right] \cdot \frac{dI}{dV}\left(V_T + u \cdot \frac{s}{\sqrt{2}}\right) du \end{aligned} \quad (1.10)$$

Where s is the deviation amplitude of the Gaussian function, and the strength of the RF noise (σ_{RF}) can be defined as $s/\sqrt{2}$. By fitting with Eq. (1.10), the value of the strength of RF noise can be determined. In the studies of chapter 3, we found the amplitude of RF noise in our system is around $280 \mu V$ after installing the filter in the bias voltage wire.

In principle, given that the other sources of noise are negligible, we have the energy resolution of the tunneling spectra limited by $k_B T$ and modulation.

Quantum Well States in Pb islands grown on Si(111)

Electrons confined in a thin metal film on a surface form standing-wave eigenstates in the direction perpendicular to the surface. These discrete electronic eigenstates are known as quantum well states (QWS)[21, 22]. Their eigenenergies crucially depend on the film thickness, because the Fermi wavelength is typically $\sim 1nm$. Consequently, as a function of film thickness, the electronic density of states (DOS) is modulated in an oscillatory manner when a QWS passes through the Fermi level. The oscillatory behavior of the electronic properties at E_F affects many of the physical and chemical properties of a thin film, *e.g.*, the local work function [23], the chemical reactivity [24], the thin film thickness [25], the thermal stability [26, 27] or even the superconducting properties at low temperature [28, 29]. Since their discovery by electron tunneling by Jaklevic *et al.* [22], QWS have been extensively studied by various techniques such as scanning tunneling microscopy (STM), photoemission (PES) and two-photon photonemission (2PPE) [22, 30, 31].

We have performed a detailed study of QWS confined in Pb islands on a Si(111) surface. We were able to fabricate two different kinds of surfaces before we deposit Pb on them; the Si(111)- 7×7 surface [32] and Pb- $\sqrt{3} \times \sqrt{3}$ /Si(111) surface [33]. On those surfaces, we control the size and thickness of Pb nanocrystals by varying the amount of Pb coverage and the substrate temperature. Under ultra-high vacuum (UHV) conditions, we regularly obtained atomically flat thin films of Pb from 2 ML to larger thickness, as

well as nanocrystals with diameters of several hundreds of nanometers to less than 10 nanometers.

In this chapter, we will discuss the preparation of these Pb islands on the two different interfaces (section 2.2) and the STM images of the results. On this clean Pb ultrathin film, quantum mechanical properties [29] of the electrons confined between the interface and vacuum barrier [32] have been observed. Tunneling spectra performed on the Pb islands show prominent QWS features (section 2.3), which will be explained and modeled by discrete levels of QWS in a tunneling junction. The energy of the QWS as a function of film thickness is determined (section 2.4), which is in good agreement with previous DFT calculations [34]. Although Pb QWS studies are numerous, quasiparticle lifetime data are still scarce. Motivated by this fact, we successfully determined the QWS lifetime from STS spectra (section 2.5), and separated the contributions to the lifetime from various scattering channels: electron-electron, electron-phonon interaction, and interface scattering.

2.1 Introduction to QWS: theory and review

Making a crystalline thin film with few MLs thickness alone with macroscopic lateral sizes is a very challenging work. This is usually not possible on an insulating substrate because metal films grow in an amorphous or granular fashion. However, it was shown recently on semiconducting substrates that adsorbates can form extraordinary smooth films of a controlled number of atomic monolayers over a macroscopic area, through "electronic growth" [35] or "quantum growth" [36]. Recently, Barredo *et al.* used a Pb thin film on Si(111) to make a macroscopic atomic flat metal surface stabilized through quantum size effects (QSE) and claimed it be to "the smoothest surface ever made" [37]. This result demonstrates the reproducibility and robustness of the Pb film making atomically flat surface. This property happens because in this class of systems, the stability of the supported metal film is mostly determined by quantum sized effects (QSE), *i.e.* by the effects resulting from the quantization of the electronic states in the direction perpendicular to the film.

The origin of the QSE is the existence of quantum well states (QWS) in an ultra-thin metallic thin film. Electrons confined in a uniform thin film form standing-wave

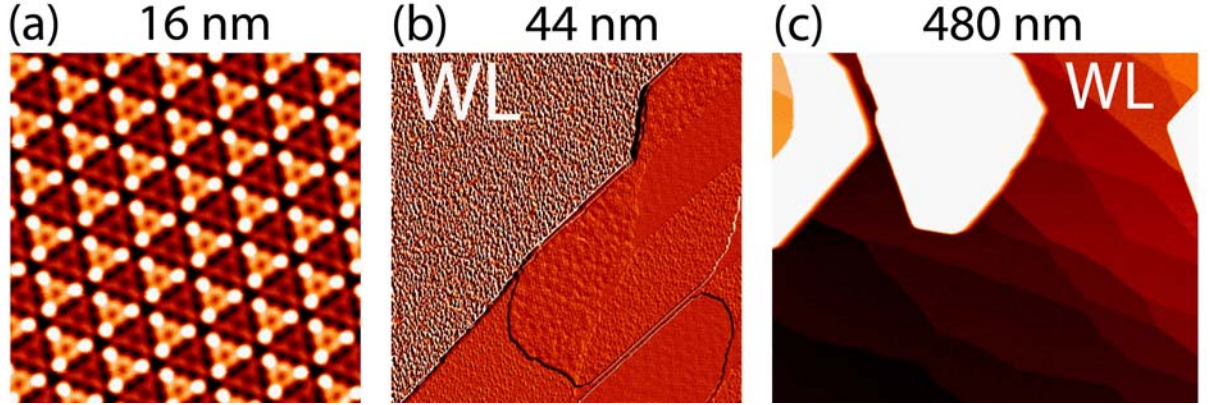


Figure 2.1: (a) Topographic images of a Si(111)- 7×7 surface. (b) Differential images of Pb wetting layers (WL) (upper left) and islands (lower right). The WL is rough and disordered indicated by the high contrast. Several thicknesses on the island are visible through the contrast change (c) Large scale overviews of the Pb islands on the 7×7 surface. Large Pb islands are observed setting on Si terrace covered by the Pb WL. $V_{bias} = -2.0 \text{ V}$, $I = 20 \text{ pA}$ for the three images.

eigenstates in the direction perpendicular to the film giving rise to discrete electron levels known as quantum well states (QWS). For a Pb thin film, because the ratio of half of the Fermi wave length to the thickness of one ML Pb is around 2 ML ($\lambda_F/2 \simeq 1.8 \text{ ML}$), one would expect oscillations of the electronic density of states (DOS) of Pb ultrathin film with every 2 ML. Because since 1.8 ML is not exactly 2 ML, over a sufficient wide thickness range, the phase of the bilayer oscillation will be reversed by a beating effects [34, 36, 38]. Consequently, as a function of film thickness, the DOS at the Fermi level (E_F) is modulated in an oscillatory manner when a QWS passes through the Fermi level. This oscillatory behavior of the electronic properties at E_F affects many of the physical and chemical properties of a thin film, in particular, it may also influence the superconducting characteristics (See Sec. 3.1.2).

The quantum phenomena of Pb ultrathin films attracted a lot of attention and excitement in the community because it was the one of the few systems [39] that under very well controlled experimental conditions, QSE could be observed very clearly. For example, this phenomena is observed in magic thicknesses of the metallic islands [35], oscillatory e - ph coupling constant [40], and oscillatory work function [41].

2.2 Sample preparation and STM images of Pb islands

In this section, we describe the preparation of the Pb islands on both 7×7 and $\sqrt{3} \times \sqrt{3}$ interfaces together with the STM images before and after the sample preparation. We

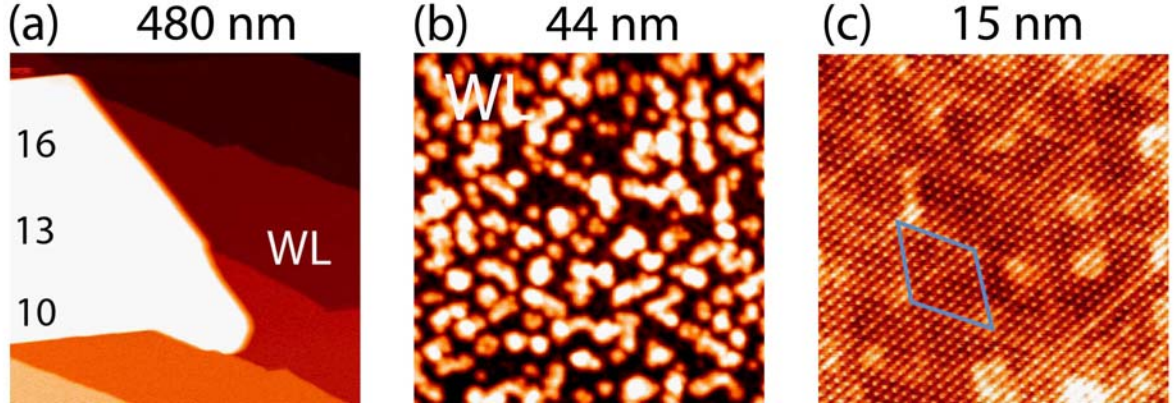


Figure 2.2: Topographic images (with indicated width) of Pb islands on a Si(111)- 7×7 . (a) large scale overviews of the Pb islands. The numbers on the islands (10, 13, 16) indicated are the thicknesses in ML of the island. (b) The disordered wetting layer (WL), which is $\simeq 1$ ML high at the base (black region) and $2 - 3$ ML high for the small clusters. (c) Atomic resolution of Pb surface with additional 7×7 structures observed through the Pb island. The 7×7 unit cell is indicated by a blue rhombus. Additional bright and dark dots suggest the presence of adatoms and vacancies at the interface.

could well identify the structures of the islands and the wetting layers by comparison with the literature.

2.2.1 Pb/Si(111)- 7×7

The preparation of Pb islands on Si(111)- 7×7 surfaces is described here. The Si(111) substrate (n doped, $\rho \sim 1\text{-}3 \text{ m}\Omega \times \text{cm}$ at 300 K) was prepared in a UHV chamber with a base pressure around 1×10^{-11} mbar. We clean the sample *in situ* employing heating cycles with a temperature $T \simeq 1470\text{K}$ for few seconds per cycle. Then we anneal the sample with $T = 1170 \text{ K}$ around a minute before decreasing the temperature slowly [42]. Keeping the pressure low (less than 1×10^{-9} mbar) during the procedure is the key for a clean surface. After the preparation, we get a clean 7×7 surface as Fig. 2.1(a) shows. Pb was thermally evaporated with a rate $\simeq 1 \text{ ML/min}$ on the Si(111)- 7×7 substrate kept at a controlled temperature favoring the growth of Pb islands with various thicknesses of a specific size. Evaporation of Pb on Si(111)- 7×7 leads to the formation of a ~ 1 ML high wetting layer (see Fig. 2.1(b)) followed by three-dimensional growth of Pb single crystals (see Fig. 2.1(b-c)) with their (111) axis perpendicular to the surface. The Pb source in a crucible with surrounding tungsten (W) filament is heated through the W wires. Because of the "electronic growth" properties of Pb [25], the Pb thin films can be grown in a layer-by-layer way.

The STM images in Fig. 2.2 show features of Pb islands grown on a Si(111)- 7×7

substrate. Large islands of several hundreds of nanometers are formed such as Fig. 2.2(a). As shown in Fig. 2.2(b), the Pb wetting layer (WL) formed on Si- 7×7 contains clusters of 1~2 ML high. Fig. 2.2(c) reveals atomic resolution of the surface Pb layer indicating that the surface of the island is atomically flat [32, 43]. In Fig. 2.2(c), the Si- 7×7 periodicity is clearly seen as the background superimposed on the atomically resolved image, where a 7×7 unit cell is indicated by the blue rhombus. Additional bright and dark spots in Fig. 2.2(c) are indications of adatoms and vacancies at the interface [43]. These spots are not from the surface of the island, otherwise atomic resolution on the island would be impossible. Studies of initial stages of Pb deposition on Si(111) [44, 45] confirmed that a number of Si atoms of the 7×7 reconstruction is replaced by Pb atoms before forming the first layer of Pb. Although the 7×7 lattice periodicity remains, some Pb atoms are involved to form an alloyed layer with Si atoms and some Si adatoms are pushed out, which is responsible for the observed adatoms and vacancies in Fig. 2.2(c) [43]. The high density of defects at the interface also causes a considerable linewidth broadening of the QWS spectra (see section 2.5).

As the accuracy of the z calibration is typically of the order of 5% of the measured height, the precision is better than 1 ML up to ~ 20 ML. Nevertheless, the determination of the thickness of the islands on both interfaces is straight forward and unambiguous. In addition to the height determination from STM profiles, we confirmed the thickness independently by measuring the QWS energies. The height of the wetting layer, which has to be taken into account in the island thickness count, is 1 ML for both interfaces (see section 2.4), which is not always clear in the literature. In the 7×7 case, although the wetting layer consists height distribution of several MLs, we can measure the height from the base flat area to the top of the island. The total thickness of the island is the measured thickness plus one ML for accounting the wetting layer.

There are certain thicknesses more favorable and more stable than others because they have a lower surface energy when a QWS passes through the Fermi level. Several STM and PES studies confirmed this phenomena already [25, 27, 38, 46–48]. The same effect is also responsible for the formation of a flat-top island [25, 36].

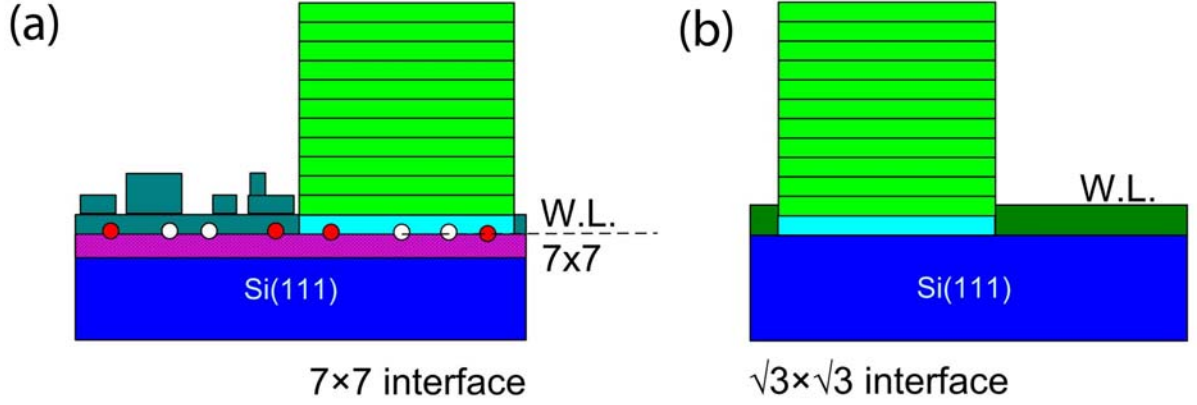


Figure 2.3: (a) Pb islands on a Si(111)- 7×7 surface. Notice that with the 7×7 reconstruction and some adatoms and vacancies (indicated with white and red circles) on 7×7 , the interface is quite disordered. (b) Pb islands on $\sqrt{3} \times \sqrt{3}$ interface. Without 7×7 and disorder, the interface is abrupt.

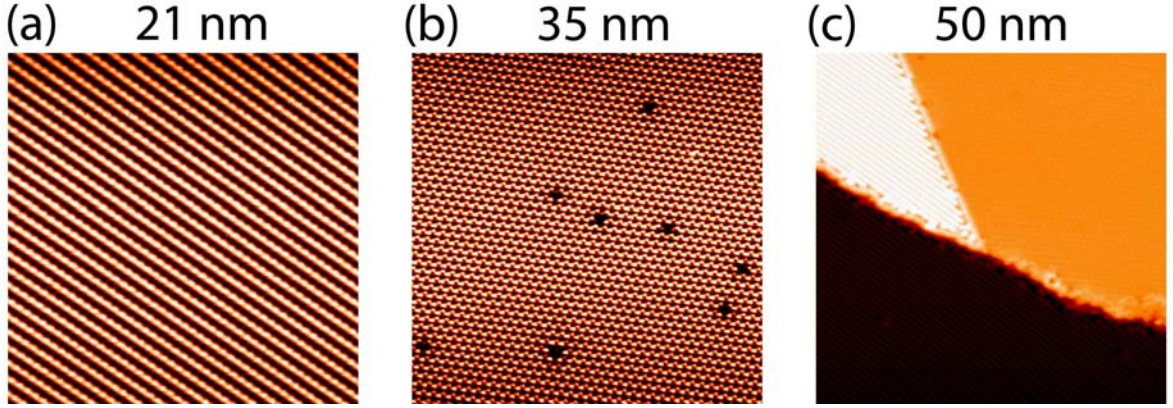


Figure 2.4: Topographic images of a Pb- $\sqrt{3} \times \sqrt{3}$ layer on Si(111). The images are taken at $T = 50 \text{ K}$. (a) Pb- $\sqrt{7} \times \sqrt{3}$ phase, a phase of Pb with $\sim 1 \text{ ML}$ coverage after annealing. (b) Pb- 3×3 phase, a phase of Pb with $\sim 1/3 \text{ ML}$ coverage. At RT, it would appear as $\sqrt{3} \times \sqrt{3}$ [49]. (c) A typical image after annealing. A mixture of Pb- $\sqrt{7} \times \sqrt{3}$ and Pb- 3×3 is often observed. Despite these two phases, they will both become the Stripe-Incommensurate (SIC) phase after further Pb deposition.

2.2.2 Pb/Pb- $\sqrt{3} \times \sqrt{3}$ /Si(111)

The Pb nanocrystals on the Pb- $\sqrt{3} \times \sqrt{3}$ interface were grown in a two-stage deposition process on Si(111)- 7×7 [33, 48]. These procedures are: (i) We deposit Pb ($\simeq 2 \text{ ML}$) on a Si(111)- 7×7 surface as mentioned before. (ii) Annealing the sample (at $T \sim 415^\circ \text{C}$) for 10 minutes transforms the surface reconstruction from the Si- 7×7 surface to a Pb- $\sqrt{3} \times \sqrt{3}$ surface. (iii) Subsequent deposition of Pb on Pb- $\sqrt{3} \times \sqrt{3}$ /Si(111) leads to the growth of Pb islands.

Figure 2.4 shows the topography after annealing. Fig. 2.4(a-b) shows the Si(111)-($\sqrt{7} \times \sqrt{3}$)-Pb (in short $\sqrt{7} \times \sqrt{3}$) and the Si(111)-(3×3)-Pb (in short 3×3) respectively. At room temperature, the structure corresponding to those two phase are also called $\sqrt{3} \times \sqrt{3}$ α phase and $\sqrt{3} \times \sqrt{3}$ β phase respectively. A surface with mixture of these two

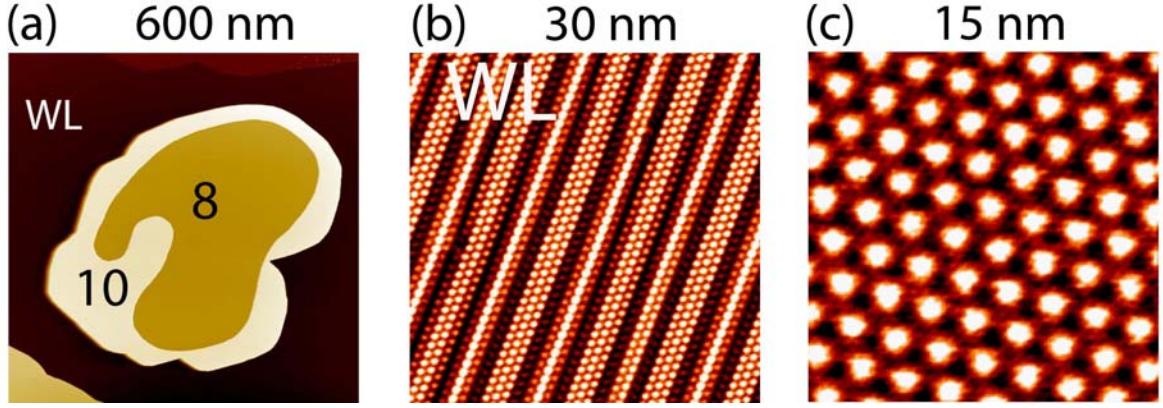


Figure 2.5: Topographic images of indicated size of Pb islands on a Pb- $\sqrt{3} \times \sqrt{3}$ interface. (a) large scale overviews of the Pb islands. The island thickness with respect to the wetting layer is indicated. (b) Wetting layer on the $\sqrt{3} \times \sqrt{3}$ interface. (c) Image taken on a 8 ML Pb islands shows Moiré pattern.

phases are common for Pb on Si(111) within a coverage of $1/3 \sim 4/3$ ML observed at low temperature, as we had observed in Fig. 2.4(c) at $T = 50K$. Despite the surface having these two different phases of Pb after the annealing procedure, the whole surface will transform to the same structure, striped incommensurate (SIC), shown in Fig. 2.5(b), after further deposition of Pb on the sample. Since the $\alpha\text{-}\sqrt{3} \times \sqrt{3}$, $\beta\text{-}\sqrt{3} \times \sqrt{3}$, or later the SIC phase are in a family of $\sqrt{3} \times \sqrt{3}$ structures, we call all of them within general as $\sqrt{3} \times \sqrt{3}$.

Figure 2.4(a) shows the Si(111)-($\sqrt{7} \times \sqrt{3}$)-Pb phase. The structure is the low temperature phase of Si(111)-(1×1)-Pb, which possesses 1.2 ML of Pb (in unit of Si coverage) [50, 51]. The phase transition temperature of Si(111)-(1×1)-Pb to Si(111)-($\sqrt{7} \times \sqrt{3}$)-Pb is around $-30^\circ C$ [52]. There is a disagreement in the literature for the Pb coverage of the $\sqrt{7} \times \sqrt{3}$ phase; some claim its coverage is of 1.2 ML [50, 51] some claim of 1.0 ML [52, 53].

In Fig. 2.4(b), we see the Si(111)-(3×3)-Pb phase, which is the low temperature phase of the Si(111)-($\sqrt{3} \times \sqrt{3}$)-Pb phase at RT with $1/3$ ML of Pb in unit of Si coverage (or 0.28 ML in unit of Pb coverage)[54]. The phase transition temperature of Pb- 3×3 to Pb- $\sqrt{3} \times \sqrt{3}$ is around 86 K [49].

The STM images in Fig. 2.5 show typical features of Pb islands grown on a Pb- $\sqrt{3} \times \sqrt{3}$ /Si(111) surface. After the second deposition of Pb, we observed regions with the Pb wetting layer (in SIC phase) [52, 55–57] (Fig. 2.5(b)) and the formation of 3D islands (Fig. 2.5(a)). When we mentioned the Pb- $\sqrt{3} \times \sqrt{3}$ /Si(111) surface (or $\sqrt{3} \times \sqrt{3}$ in short)

or the wetting layer (WL), we refer to the surface shown in Fig. 2.5(b), which is called striped incommensurate (SIC) phase of Pb, with a coverage of $4/3$ ML in the unit of Si coverage. There is an infinite number of phases of $\text{Pb}\sqrt{3}\times\sqrt{3}/\text{Si}(111)$ of coverage between 1.2 ML and $4/3$ ML, also known as "devil's staircase", confirmed by STM and diffraction measurements [46, 51]. The SIC phase is the phase of saturated Pb coverage ($4/3$ ML) among these infinite series of phases. We found this crystalline SIC layer everywhere around the Pb islands.

As Fig. 2.5(a) shows, large Pb islands of several hundreds of nanometers are observed. Numbers indicated on the island are thicknesses (in ML including the wetting layer). Pb islands grown on $\text{Pb}\sqrt{3}\times\sqrt{3}$ show a crystalline topography both on the island and on the WL (see Fig. 2.5(a-b)). The observed Pb islands are single crystal flat-top islands grown on top of the wetting layer. On top of these 3D Pb islands, Figure 2.5(c) shows a typical Moiré pattern. The Moiré patterns originate from an interfacial strain field caused by the difference between the Si and Pb lattice constant [58]. The interface under the Pb island has not necessarily the same structure as the wetting layer. The distortion of SIC structure occurs in the wetting layer very closed to the islands.

Between the Pb layer (or Pb island) and the Si substrate, the interface is similar to truncated Si(111) surface without the 7×7 reconstruction. The 7×7 reconstruction is removed during the annealing procedure. It is shown that the annealing treatment results a bulk-like termination of Si(111) interface upon which smooth Pb film can grown in a layer-by-layer way after the formation of the wetting layer [38, 47, 59–63]. Therefore, the $\sqrt{3}\times\sqrt{3}$ interface is much more ordered than the 7×7 interface. This fact strongly influence the linewidth of the QWS of Pb thin films.

2.3 QWS in Pb islands: STS data and modeling

2.3.1 STS results

For all differential conductance measurements, large Pb islands of thicknesses in the range 4 to 60 ML were chosen. dI/dV curves were recorded far enough from steps or island boundaries (at least several tens of nm) to avoid additional scattering contributions to the QWS linewidth.

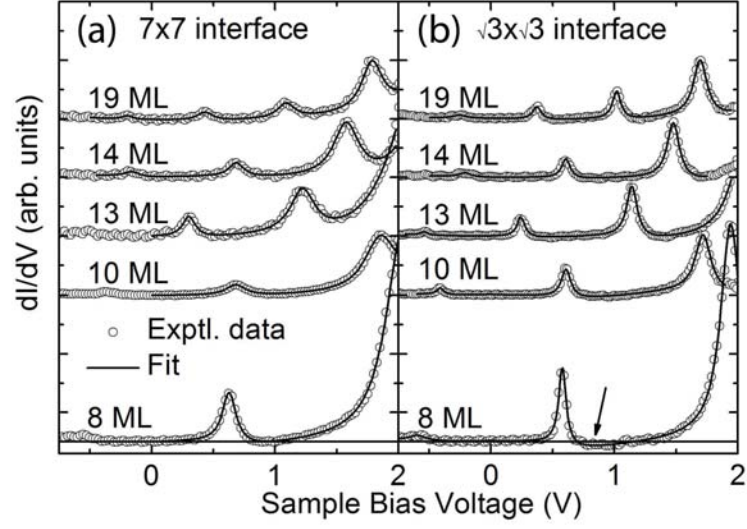


Figure 2.6: Differential conductance spectra (dots) taken at a temperature of $T = 5$ K on Pb islands of the indicated thickness on (a) the 7×7 and (b) the $\sqrt{3} \times \sqrt{3}$ interface. Full line: Least squares analysis (see text).

Figure 2.6 presents typical dI/dV spectra (dots) obtained at a temperature of $T = 5$ K on Pb islands of selected thickness between 7 and 18 ML. The full line connecting the data points is the result of a least squares analysis (see Section 2.3.2). The prominent maxima in these spectra reflect the existence of QWS formed in the Pb islands of various thickness [32]. A comparison between the spectra shown in Fig. 2.6(a) and (b), obtained on the two different interfaces, reveals a considerable narrowing of the QWS linewidth on the $\sqrt{3} \times \sqrt{3}$ interface.

In Fig. 2.6, two kinds of asymmetric features are observed in the spectra on the $\sqrt{3} \times \sqrt{3}$ interface and are described below. (i) The arrow beyond the QWS peak in Fig. 2.6(b) indicates the presence of a negative differential conductance (NDC) at increasing positive bias voltage. (ii) The QWS peaks measured at negative bias voltage behave differently from the ones observed at positive bias voltage; there is no NDC feature presented on the negative bias voltage side and generally the QWS peak height is smaller on a smaller exponential background. At a gap voltage below -0.5 V, the QWS intensity is even weaker because of the existence of the Si valence band below this energy [38].

All these observations reveal the high quality of our data and are well described within our model (see below). From the comparison of the results of density functional theory (DFT) calculations for the QWS energies of free standing Pb films [34] with our extracted peak energies, the height of the wetting layer is found to be 1 ML for both interfaces [64]

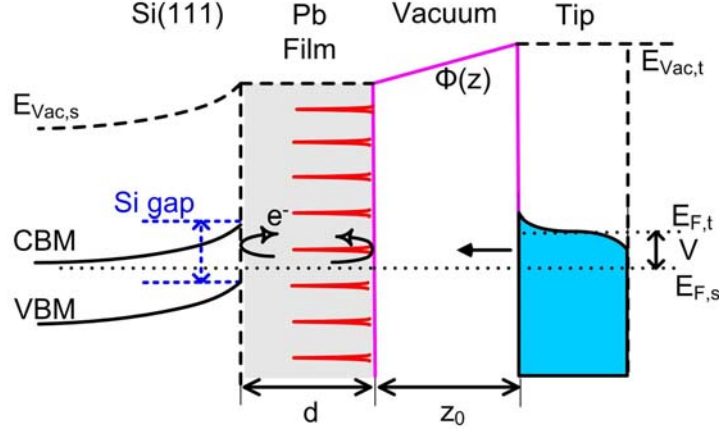


Figure 2.7: Schematic energy diagram of the tunneling junction used for our modeling of the QWS in thin Pb films.

(see section 2.4).

2.3.2 Modeling and fitting of the dI/dV spectra

To extract the intrinsic linewidth of the QWS peaks, the STS data are modeled based on the WKB approach [12, 32]. Figure 2.7 depicts a schematic energy diagram of the model. The density of states (DOS) of the sample (ρ_s) is simulated as a series of Lorentzian peaks representing the QWS DOS (Eq. (2.1)). In each QWS level n , the QWS energy levels is E_n with amplitude A_n , and the linewidth of the level is W_n . The DOS of the tip is assumed to be constant ($\rho_t \simeq 1$). Eq. (2.2) presents the Fermi-Dirac distribution taking into account of the temperature broadening. The tunneling current (I_{wkb}) is then written as Eq. (2.3).¹

$$\rho_s(\epsilon) = \sum_n \frac{A_n}{1 + \left[\frac{\epsilon - E_n}{W_n/2} \right]^2}, \quad (2.1)$$

$$f(\epsilon) = \frac{1}{1 + \exp \left[\frac{\epsilon}{k_B T} \right]}, \quad (2.2)$$

$$I_{wkb}(V_T) = \int_{-\infty}^{\infty} \left[\rho_s(\epsilon) \rho_t(\epsilon - eV_T) [f(\epsilon) - f(\epsilon - eV_T)] \times \exp \left(-\frac{2}{\hbar} \int_0^d \text{Re} \left\{ \sqrt{2m[\Phi_a - \epsilon + (1 - \frac{z}{z_0})eV_T]} \right\} dz \right) \right] d\epsilon. \quad (2.3)$$

The tunneling current (I_{wkb}) is represented as a convolution of the density of states of

¹The following approximations are made: The barrier width (z_0) is 10 Å. The tunneling barrier potential of vacuum has a trapezoidal shape. The work functions of both, sample and tip, are identical ($\Phi_a = 4 \text{ eV}$).

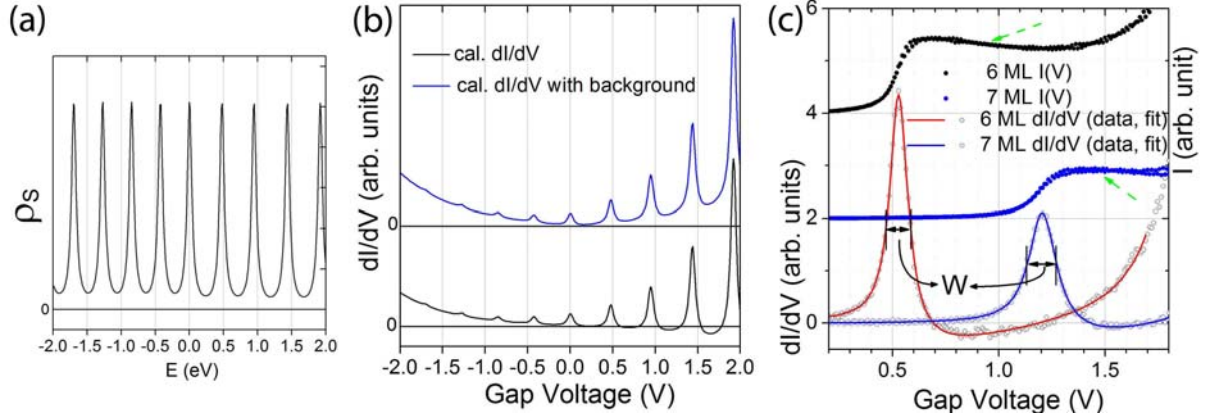


Figure 2.8: (a) Simulations of the density of states (DOSs) of the sample (ρ_s) is modeled by a series of Lorentzian peaks with equi-amplitude. (b) Simulated conductance by Eq. (2.4) without (black curve) and with the background term (blue curve). Without the exponential background, it is clear that the tunneling transmission coefficient causes the asymmetry of amplitude between positive and negative voltage range. Negative differential conductance (NDC) is shown at higher bias voltage. The blue curve is calculated by using Eq. (2.4) accounting for the contributions of the bulk states by addition of an exponential term. (c) Tunneling current and dI/dV data. The fitting agrees very well with the dI/dV data. NDC, indicated by the green arrows, is visible in $I(V)$ as well as in dI/dV .

the tip and the sample at finite temperature. The tunneling transmission coefficient is included in the exponential term of Eq. (2.3). Φ_a is the workfunction for both tip and sample, z the tip-sample distance, ϵ the energy, and V_T the tunneling bias voltage.

The contribution of bulk states other than the QWS to the tunneling current is modeled by an additional exponential term in the least squares analysis of the experimental dI/dV spectra. Consequently the fit function dI/dV of our modeling can be expressed as:

$$\frac{dI}{dV}_{Fit}(V_T) = \frac{dI_{wkb}(V_T)}{dV_T} + [A_{bkg} \cdot (e^{V_T/b} - 1)]. \quad (2.4)$$

This analysis Eq. (2.4) describes convincingly the STS data shown in Fig. 2.6(a-b) and in Fig. 2.8(c).

Figure 2.8 illustrated the intermediate steps in going from Eq. (2.1) to Eq. (2.4). Fig. 2.8(a) shows the DOS of the QWS system, which is calculated by Eq. (2.1) with equal amplitude of all the peaks. The DOS in Fig. 2.8(a) is used for the calculation of Fig. 2.8(b). There, we observed clearly the effect of the tunneling transmission coefficient on ρ_s . In particular, the model reveals that the asymmetries observed in the data originate from the tunneling process. Electrons with higher energy (close to 2 eV) have a higher tunneling probability because they "see" a lower tunnel barrier. The asymmetry between the positive and negative bias voltage is clearly seen in the black curve of Fig. 2.8(b).

The negative differential conductance (NDC) is also clearly seen before the addition of the exponential background. We fit the data as shown for the blue line of Fig. 2.8(b).

Figure 2.8(c) shows very good agreement between the experimental dI/dV data and the fit. The NDC feature is clear from the slope of the tunneling current in the graph.

In order to extract the intrinsic linewidth (Γ) from the fitted linewidth (W) and to eliminate the possible partial transmission of the electronic wave function to the substrate, we further employed the Eq. (2.5)-(2.6) into the analysis [39].

$$W = \Gamma \eta \frac{1 - \text{Re} \exp(-1/\eta)}{R^{1/2} \exp[-1/(2\eta)]}, \text{ with} \quad (2.5)$$

$$\eta = \frac{\ell}{d}. \quad (2.6)$$

Here, ℓ is the mean free path of the electron associated with the linewidth Γ , d is the film thickness, W is the STS apparent linewidth from the fit of Eq. (2.4), and R the reflectivity of the interface. Γ and R are fitted from sets of W and d , which are known from experiments. The extracted reflectivity (R) is very close to one (97-100%) in all the studied energy range. Exceptions only occur at very thin layers of energy above 1 eV, where R decreases by a few percent. This indicates an efficient confinement of the QWS between the interface and the vacuum. This is also consistent with our STS results on Si(111)- 7×7 showing a substrate band gap between -0.5 and +3.0 V. If other broadening mechanisms were absent, the quasiparticle lifetime would be

$$\tau = \frac{\hbar}{\Gamma}. \quad (2.7)$$

The extracted Γ s are the linewidth we used for further analysis (see section 2.5.1) where Γ can be separated into several terms (Eq. (2.9)). We consider Γ as an intrinsic linewidth (inverse lifetime) and that extrinsic broadening of the linewidth is taken out by the procedures of Eq. (2.4) and Eq. (2.5) or is negligible.

2.3.3 Discussion on the peak lineshape

The differential conductance measured in a tunneling spectra is proportional to the convolution of the DOS of the two objects separated by a barrier. Now we consider the case depicted in Fig. 2.7: the DOS of the tip is flat and the DOS of the ultrathin film possesses QWS. Consider this situation in k space, shown in Fig. 2.9. The DOS of a QWS system

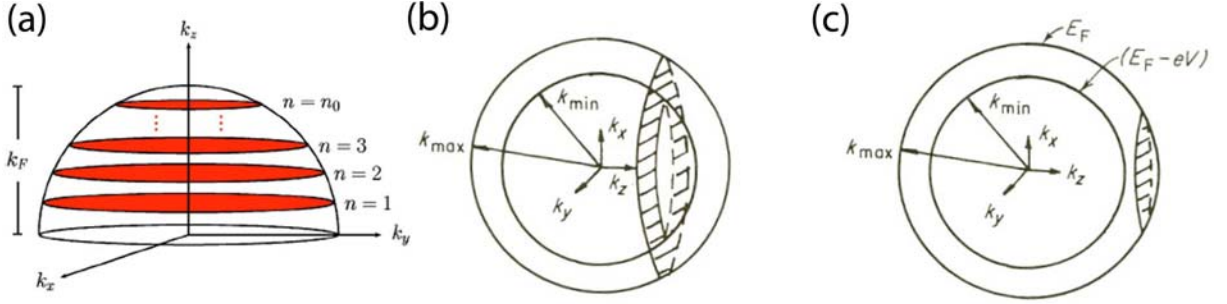


Figure 2.9: (a) Confinement of the electrons to a quantum well causes the Fermi sphere of allowed states to collapse to a discrete set of disks [47]. (b, c) Schematic shows k-space location of electrons eligible to tunnel from left to right in a junction under bias voltage [12]. (b) $k_z < k_{max}$ (c) $k_{min} < k_z < k_{max}$

along k_z is an assembly of discrete levels (Fig. 2.9(a)), however, the integral of DOS over all k direction as a function of energy is a step. In Fig. 2.10², the density of states of a two dimensional (2D) quantum well as a function of electron energy has a step shape. This kind of behavior has been confirmed in experiments on a two dimensional electron gas (2DEG) in a semiconductor quantum well [65]. On the contrary, Jaklevic *et. al.* [22] observed QWS showing a line shape of peaks in tunnel measurements in thin Pb films in a planar junction geometry. They attributed the appearance of the peak shape in the spectra to a voltage dependent transmission coefficient [66]. Here, we also observed peak shape in the tunneling spectra for QWS of Pb films. Jaklevic *et. al.* measured spectra resulting from standing waves in a Pb film consisting of several thicknesses, but here by using STM/STS, we could measure the spectra on a Pb film with a single thickness. However, we found by our simulations that their explanation [66] does not agree well with our results. Thus we disregard the argument of the voltage dependent transmission coefficient to explain the peak shape observed in our tunneling spectra. Here, we argue that we model the DOS of Pb thin films as an assembly of discrete QWS levels for the following reasons: (i) The high effective mass (m^*) of Pb associated to its band structure. (ii) The tunneling process favors the k_z direction with respect to planar direction; this preference can be described by a tunneling cone angle. We discuss these two factors as following.

(i) PES experiments reported an unusually high effective electron mass $m_{||}^*$ of Pb/Si(111) QWS subbands which are 5 to 10 times the free electron mass (m_e) [67]. By comparing the band structures measured by ARPES [67] and band calculations [68], one found that

²Source of the image: Wikipedia (density of states). http://en.wikipedia.org/wiki/Density_of_states

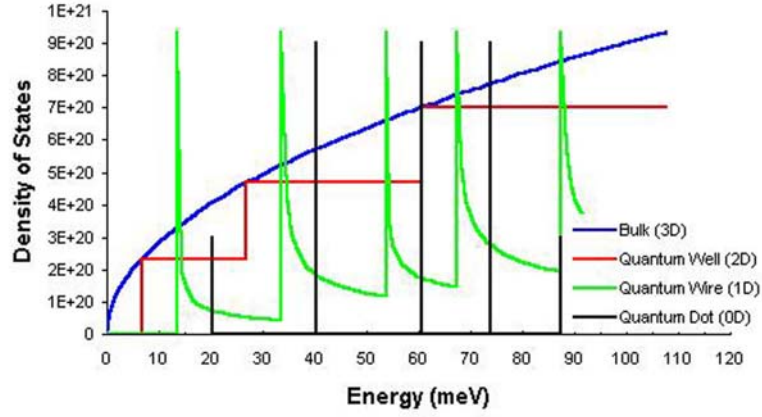


Figure 2.10: Density of states (DOS) of quantum dots (0D), one dimensional quantum wire (1D), two dimensional quantum well (2D), and 3D solids. Source of the image: see footnote 2.

the QWS band appears flat in the k_{\parallel} direction within the range of $\pm 0.2 - 0.4 \text{ \AA}^{-1}$. Considering k_F is 1.5 \AA^{-1} for Pb, the QWS flat band covers an angle around $\pm 8 - 15^\circ$. Furthermore, STM investigations also suggested m_{\parallel}^* around $10 m_e$ [43]. As a consequence, the tunneling probability for higher k_{\parallel} values strongly decreases.

(ii) The transmission coefficient decays exponentially as a function of the angle with respect to the normal tunneling direction. In planar junction experiments the cone angle, where the transmission decreases to $1/e$, is estimated to be around 8° [12, 69]. Neglecting factors depending on the tip shapes, we estimated ³ the cone angle of our Pb/vacuum/tip junction to be around $11 \sim 13^\circ$. A sharp tip in principle have an effect to decrease the angle.

Another consideration is the Schottky barrier of Si substrate. The existence of a Schottky barrier between Pb film and Si substrate has been confirmed by transport and PES measurements [59]. The barrier height is estimated to be between 0.9 to 1.1 eV [59]. The Schottky barrier and the vacuum barrier form a double barrier tunneling junction. Such a junction has the property of resonance tunneling, confining electrons with the consequence that electrons with k_{\parallel} wave vector components decay faster at each reflection. However, in our case of Pb/Si, the cover of the wetting layer everywhere will enhance the conduction between the Pb island and the substrate. Thus the good conductance will make the Schottky barrier factor much less important. Recently Schmeidel *et al.* [70] clearly observed the Coulomb blockade phenomena for Ag particles on bare Si(111)

³We estimated the cone angle of the Pb-Vacuum-tip junction by following [12, 69] with parameters: workfunction of Pb ($\Phi = 4 \text{ eV}$), junction width ($d_{ts} = 10 \text{ \AA}$), Fermi energy of Pb ($E_F = 9.47 \text{ eV}$).

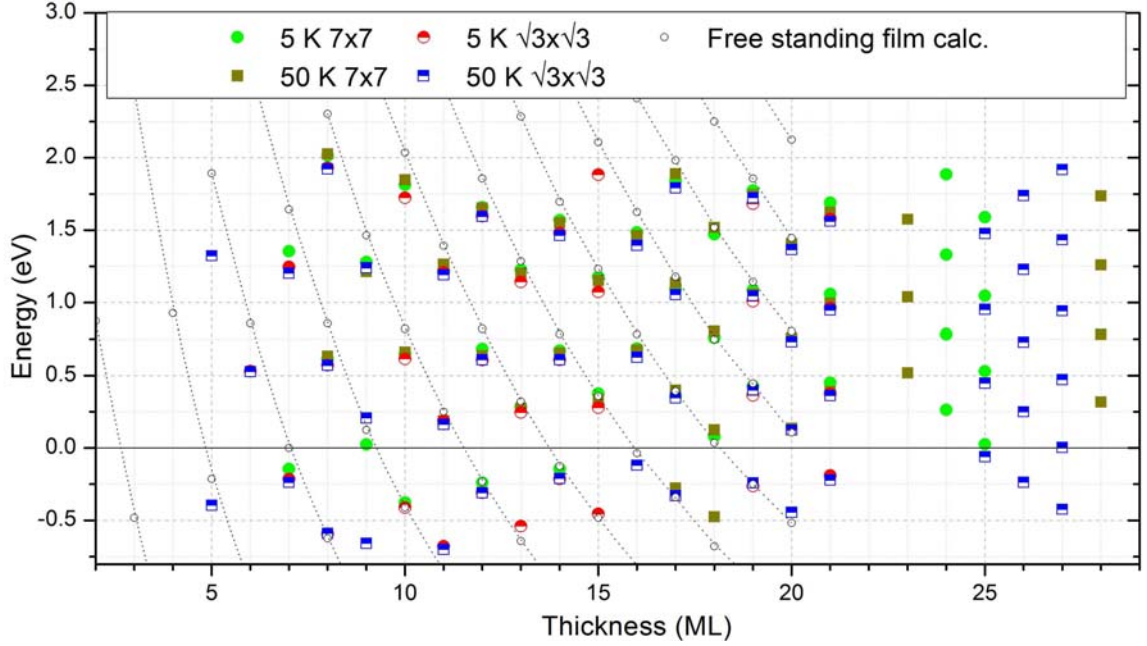


Figure 2.11: Quantum well states binding energies as a function of thickness. The free standing film DFT calculations result is taken from the work of Wei *et al.* [34]. The experimental results are very similar to the calculations, especially at higher thickness. For films with lower thickness, the results deviate from the the calculations, accounting for the effect from the substrate. Below energy of -0.5 eV , there is a Si valence band and QWS are not discernible.

surfaces and the disappearance of Coulomb blockade for Ag particles on the wetting layer. This confirms the existence of the Schottky barrier on a pure Si substrate and its reduction by a wetting layer.

On the other hand, lifetimes measured in STS are influenced by the electric field between tip and sample. The tip-induced field may cause an increase in inelastic scattering which reduces the lifetimes of, e.g., image state electrons on Cu(001) and Ag(001) surfaces by 50% [71]. However, the influence of this tip field effect is small here, because it is screened by the electrons of the metal thin film.

2.4 Energy levels of the QWS

By comparison of the topography and the results of STS spectra, we are able to determine the thickness of the Pb islands unambiguously. The calculated and measured QWS energy levels as a function of thickness are shown in Fig. 2.11. The measured QWS energies agree well with DFT calculations [32] for the occupied states and unoccupied states with thickness higher than 17 ML. For unoccupied states of thinner films, the measured energy is systematically lower than the free standing film calculations. The evolution of this

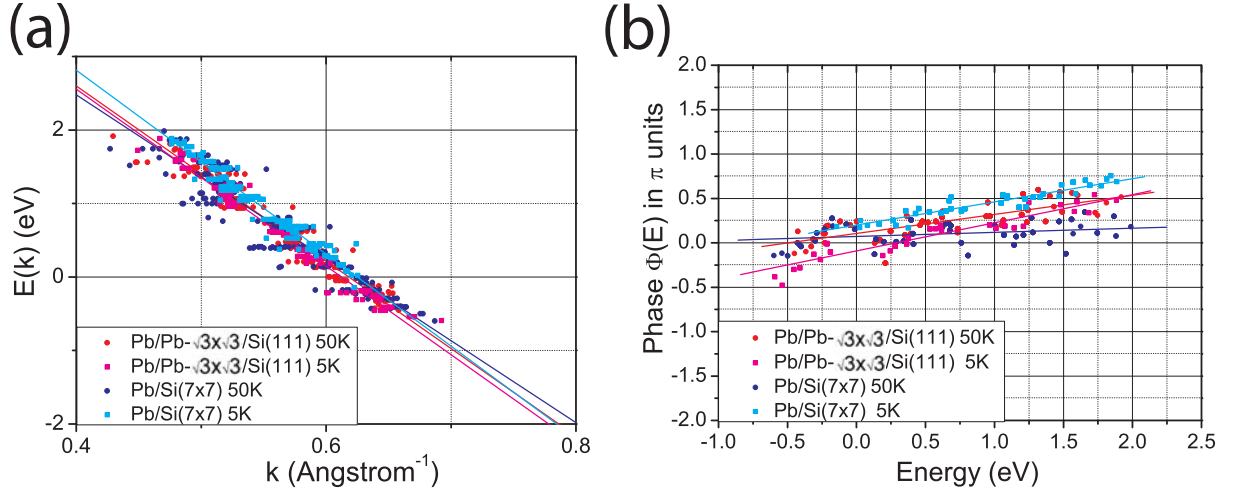


Figure 2.12: Extracted band dispersion and phase from the analysis of phase accumulation model by Eq. (2.8). (a) reconstructed band dispersion $E(k)$ along $[\Gamma L]$ direction. (b) Extracted phase shift.

deviation clearly accounts for the effects from the substrate which the calculations didn't include. Below an energy of -0.5 eV, the QWS interact with the Si valence band and thus the determination of the QWS energy is not obvious. In addition, as we showed previously, the QWS peaks appear smaller in the negative energy range because of the tunneling transmission coefficient (See Fig. 2.8).

2.4.1 Band dispersion

$$\begin{aligned} \Phi_B(E) + \Phi_C(E) + 2k(E)d &= 2\pi n, \\ 2k(E)(d_1 - d_2) &= 2\pi(n_1 - n_2) \\ , \Phi(E) &= \Phi_B(E) + \Phi_C(E). \end{aligned} \quad (2.8)$$

Using the phase accumulation model (or Bohr-Sommerfeld quantization rule) (as in Eq. (2.8)) [72], the reconstructed band dispersion $E(k)$ along the $[\Gamma L]$ direction and the energy dependent phase shifts are extracted from QWS energies. The results are shown in Fig. 2.12. In Eq. (2.8), by applying the quantization rules for a thickness d and quantum number n from Fig. 2.11, we can obtain the wave vector $k(E)$ in the perpendicular direction and the phase $\Phi(E)$ as a function of energy. An analysis of the reflectivity at 50 K and 5 K on both types of samples shows clearly the increased quality of the $\sqrt{3} \times \sqrt{3}$ interface, consistent with results from the linewidth analysis (Sec. 2.5). Our results for the dispersion relation are consistent with photoemission experiments [40] and the calculated m^* is consistent

with the bulk value.

2.5 Decay processes of QWS in metallic thin islands

The quasiparticle lifetime of QWS is of fundamental interest because it determines the mean free path of the electrons. Moreover, the lifetime width contains important information about the strength of many-particle interactions, reflected, *e.g.*, in the electron-phonon coupling constant fundamental for superconductivity [40].

However, the direct measurement of the intrinsic quasiparticle lifetime on the atomic scale is not straightforward [73, 74]. In photoelectron spectroscopy (PES), which is restricted to probe only the occupied states of a sample on a macroscopic scale, the measured linewidth of a QWS is proportional to the inverse lifetime of the state. In 2 photon photoemission (2PPE) experiments the lifetime of such a state is directly determined [75], however, multi-electron interaction in the excited state makes a quantitative analysis more difficult. On the other hand, scanning tunneling spectroscopy (STS) is able to measure the lifetime of an electronic state via its linewidth in the tunneling spectra for both, occupied and empty states on a local scale [76]. In spite of these experimental advantages, up to now STS studies of QWS lifetimes [77] have been scarce, due to the lack of k resolution in STS.

The contributions to the QWS quasiparticle lifetime, including defect scattering, interface scattering, electron-phonon interaction, and electron-electron interaction, are quantitatively determined in the following.

2.5.1 Linewidth analysis

We obtained linewidths from the STS spectra showing QWS peaks by fits according to Eq. (2.4) and Eq. (2.5). The reflectivity extracted by Eq. 2.5 is shown in Fig. 2.13. The reflectivity of all the data is very close to 100% ensuring the good confinement of electrons between the two interfaces. The linewidth is extracted with the inclusion of the broadening of tunneling transmission coefficient and of reflection. Using this analysis for our data obtained for various thicknesses and temperatures, we investigate the linewidth with more details. Due to the instrument, we measured at only two temperatures, 50 K

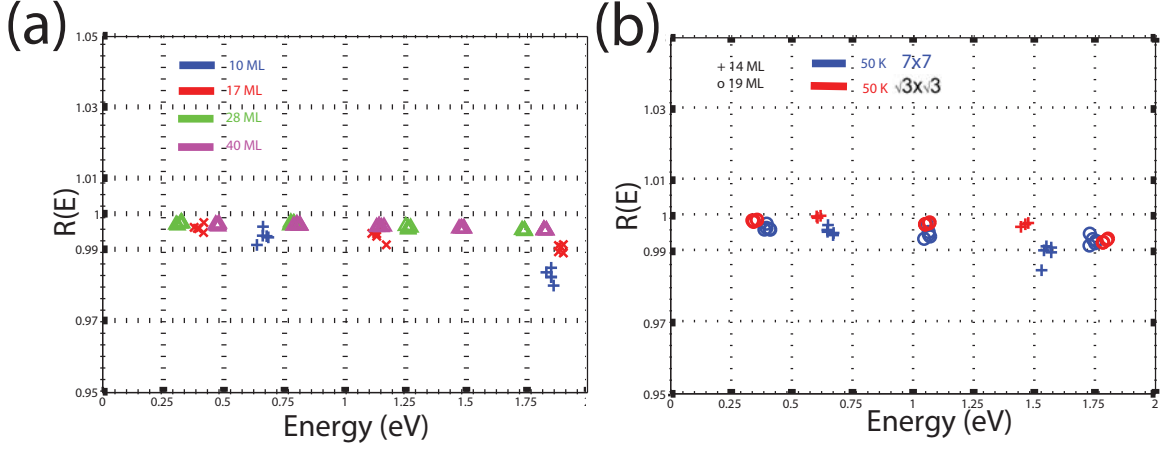


Figure 2.13: Extracted reflectivity from the thicknesses and QWS linewidths by Eq. 2.5. (a) Reflectivity of Pb islands with different thicknesses on 7×7 interface. (b) Reflectivity of Pb islands of 14 and 19 ML on 7×7 and $\sqrt{3} \times \sqrt{3}$ interfaces. The reflectivity is very close to 100% for all of the data.

and 5 K. We collected data from various thicknesses of Pb films, and at each thickness there are 1-4 QWS peaks available. Since each thickness does not share the same QWS energy, we could not separate the thickness dependence and energy dependence in our analysis for the data presented here. Nevertheless, Γ can be separated into several terms listed in Eq. (2.9) [30] as those terms describe different scattering channels, including: Γ_0 is independent of T and E (it describes defect and interface scattering), Γ_{e-e} describes the electron-electron interaction, and Γ_{e-ph} describes the electron-phonon interaction.

In Eq. 2.10, the linewidth has a parabolic relation with respect to the excitation energy ($E - E_F$) according to 3D Fermi liquid theory [78], where α is the electron scattering term. Equation 2.11 presents the Γ_{e-ph} term [30], where λ is the electron-phonon coupling constant, E_D the Debye energy, $f(E)$ and $b(E)$ the Fermi-Dirac and Bose-Einstein distribution. For $E \geq 50 \text{ meV}$, $\Gamma_{e-ph}(E, T) \simeq \Gamma(T)$. In Eq. (2.12), τ is the quasiparticle lifetime assuming no further extrinsic broadening of the linewidth. The linewidth (Γ) extracted within this model from the STS data at $T = 50 \text{ K}$ and $T = 5 \text{ K}$ and on both

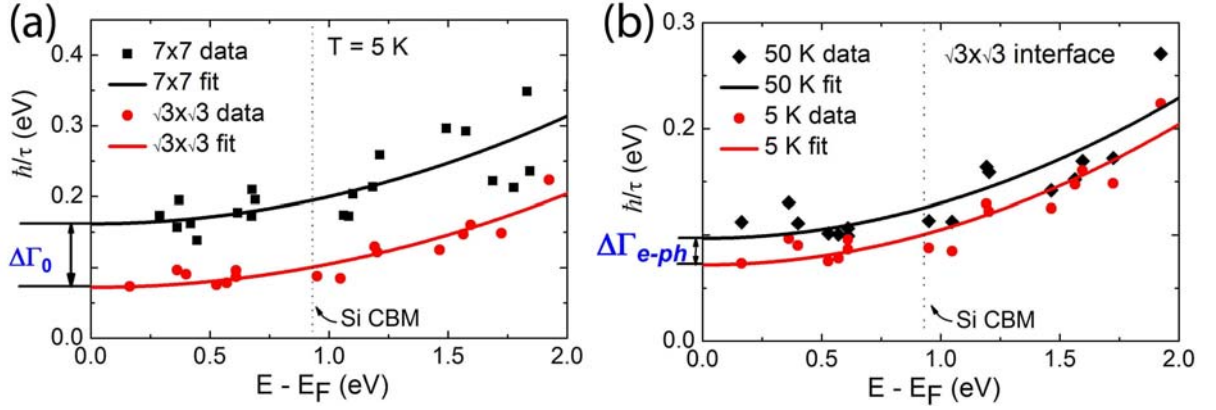


Figure 2.14: Inverse quasiparticle lifetime (squares and dots) of QWS on the two interfaces ($\sqrt{3} \times \sqrt{3}$ and 7×7) and two temperatures (50 K and 5 K). All of them show parabolic curves. (a) The difference of the interfaces (at the same temperature) yields $\Delta\Gamma_0$. (b) The difference of the two temperature (on the same interface) yields $\Delta\Gamma_{e-ph}$.

interfaces is presented as a function of energy in Fig. 2.14.

$$\Gamma(T, E) = \Gamma_0 + \Gamma_{e-e}(E) + \Gamma_{e-ph}(E, T), \text{ with} \quad (2.9)$$

$$\Gamma_{e-e}(E) = \alpha(E - E_F)^2, \quad (2.10)$$

$$\begin{aligned} \Gamma_{e-ph}(E, T) &= 2\pi\lambda \int_0^{E_D} \left(\frac{E'}{E_D}\right)^2 \left[1 - f(E - E') + 2b(E') + f(E + E')\right] dE' \\ &\approx \Gamma_{e-ph}(T), \end{aligned} \quad (2.11)$$

$$\tau = \frac{\hbar}{\Gamma}. \quad (2.12)$$

2.5.2 Scattering channels

Figure 2.14, shows the inverse lifetime as a function of energy ($E - E_F$). The observed parabolic behavior is in agreement with 3D Fermi liquid theory [79]. In Fig. 2.14, all the data curves show almost the same α value, which enables us to determine the difference of the two curves accounting for the interface and for the temperature effects. In Fig. 2.14(a), the $\Delta\Gamma_0$ is obtained by taking the difference between the two interfaces (7×7 and $\sqrt{3} \times \sqrt{3}$). In Fig. 2.14(b), the electron-phonon contribution is obtained by taking the difference between the two temperatures (50 K and 5 K). We obtain a value of about $\Delta\Gamma_{e-ph} = 25 \text{ meV}$ in Fig. 2.14(b), which is close to our estimation for bulk Pb within the Debye model. A Debye model [78] with bulk electron-phonon coupling constant $\lambda_{bulk} =$

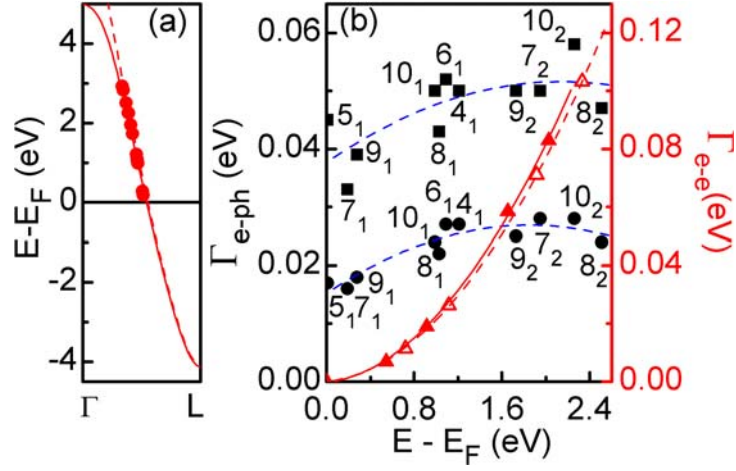


Figure 2.15: (a) Calculated dispersion of the electronic band crossing E_F along $\Gamma - L$ for bulk Pb without spin-orbit coupling (with SOC): dashed (solid) line. Dots: computed QWS energies. (b) Calculated Γ_{e-e} and Γ_{e-ph} for unoccupied QWS as a function of energy. Γ_{e-e} without SOC (with SOC): open (full) triangles. Γ_{e-ph} at 5 K (50 K): dots (squares) with their fit. In n_m ($n = 4, \dots, 10$; $m = 1, 2$) n is the film number of monolayers, and m is the QWS number counted from E_F . The calculations are performed in San Sebastián, Spain [64].

1.55 yields $\Delta\Gamma_{e-ph} = 23 \text{ meV}$.

In order to gain more insight from our experimental results, we collaborated with a group of theoretician based in San Sebastián, Spain [64]. We present first-principle calculations results for electron-electron (Γ_{e-e}) and electron-phonon (Γ_{e-ph}) contributions to the QWS linewidth (Fig. 2.15). Our theoretical estimation of Γ_{e-e} for QWS in Pb(111) films is based on an *ab initio* calculations of Γ_{e-e} for their parent bulk band that crosses E_F along the $\Gamma - L$ direction, perpendicular to the (111) plane [80]. We show that spin-orbit coupling (SOC) does not affect either band energies or Γ_{e-e} in the energy range of interest. Γ_{e-ph} is directly obtained from layer-dependent *ab initio* density functional calculations of free-standing Pb(111) films of 4-10 monolayer thickness. The latter calculations take full account of quantum-size effects on film electron and phonon band structures as well as on $e-ph$ coupling [64, 80, 81].

The results are summarized in Fig. 2.15 where the energy dependence of both contributions to the QWS linewidth, $e-e$ and $e-ph$ are shown together with the dispersion of the electronic band crossing the Fermi energy in the $\Gamma - L$ direction of bulk Pb. The energy dependence of QWS on film thickness indicated by full circles in the figure, follows the bulk band dispersion.

Figure 2.15(a) shows that the calculated QWS energies are almost lying on the parent bulk band. The calculated effective masses are very close to the free electron mass in

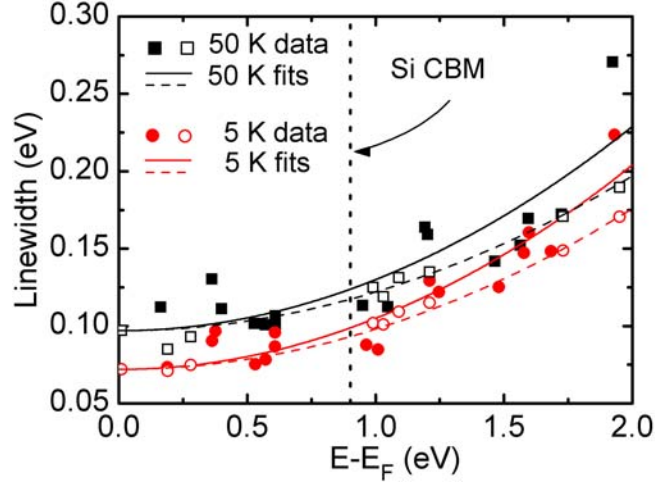


Figure 2.16: Linewidth versus energy of unoccupied QWS in Pb islands grown on $\text{Pb-}\sqrt{3}\times\sqrt{3}/\text{Si}(111)$ measured at 5 (50) K: full dots (full squares). The data are fitted according to 3D Fermi-liquid theory (continuous lines). Theoretical linewidth $\Gamma_{e-e} + \Gamma_{e-ph}$ at 5 (50) K: open dots (open squares) with corresponding fits (dashed lines). For easier comparison the theoretical data have been shifted vertically so that the theoretical fits coincide with the experimental ones at low energy. The linewidth difference $\Delta\Gamma_{e-ph} \simeq 25$ meV between the 50 and 5 K fit to the experimental data agrees very well with the corresponding calculated difference, yielding the QWS $e-ph$ coupling constant $\lambda \simeq 1.45 - 1.60$. Silicon conduction band minimum is indicated. The calculation is performed in San Sebastián, Spain [64].

the sense of vertical direction. Figure 2.15(b) shows $\Gamma_{e-e}(E)$ estimated for the bulk band structure using a bulk band energy equal to the QWS energy with and without SOC. A quadratic dependence $\Gamma_{e-e} = \alpha(E - E_F)^2$ is found, leading to $\alpha = 0.023 \text{ eV}^{-1}$ with SOC (0.021 without), which are very close to $\alpha = 0.02 \text{ eV}^{-1}$ obtained when treating bulk Pb as a free electron gas and assuming 3D Fermi liquid theory (with $r_s = 2.30 \text{ a.u.}$). Hence, in the probed energy range, the SOC effect on band (QWS) energies and on Γ_{e-e} is small. Figure 2.15(b) shows Γ_{e-ph} versus QWS energy calculated for 5 and 50 K. Given the relation $\Delta\Gamma_{e-ph} = \Gamma_{e-ph}(50\text{K}) - \Gamma_{e-ph}(5\text{K})$, we show the fit of calculated $\Delta\Gamma$ in dashed lines in Fig. 2.15(b). It varies with QWS energy, but the difference between the averaged Γ_{e-ph} , remains nearly constant, increasing from 23 meV (close to E_F) to 26 meV (at higher energies). Since the energy dependence of Γ_{e-e} is much stronger than that of Γ_{e-ph} , their sum $\Gamma_{e-e} + \Gamma_{e-ph}$, is fitted reasonably well by a quadratic equation with $\alpha=0.025 \text{ eV}^{-1}$ (0.026) at 50 (5) K (see Fig. 2.16).

As one can see from Fig. 2.15, the spin-orbit corrections effects are very small for Γ_{e-e} . The $e-e$ broadening caused by the spin-orbit splitting of the QWS [82] was estimated to be less than 10 meV. The similar conclusion was drawn experimentally [82] because the states with non-zero k_{\parallel} contribute very little to tunneling.

Figure 2.16 shows Γ versus energy measured at 50 and 5 K on Pb- $\sqrt{3} \times \sqrt{3}$ with the theoretical ($\Gamma_{e-e} + \Gamma_{e-ph}$). In Fig. 2.16, the sum of both contributions, $e-e$ and $e-ph$, exhibit a quadratic dependence on the QWS energy. Both experimental data sets are well fitted by 3D FL theory: $\Gamma(E) = \alpha(E - E_F)^2$, yielding the same value $\alpha = 0.033 \text{ eV}^{-1}$. The two fit curves to the experimental data between the 50 and 5 K gives $\Delta\Gamma_{e-ph} \simeq 25 \text{ meV}$. $\Delta\Gamma_{e-ph}$ yields an estimate of the average $e - ph$ contribution to the QWS lifetime, which is in excellent agreement with the theoretical $\Delta\Gamma_{e-ph} \simeq 23 - 26 \text{ meV}$. A similar analysis was conducted on the 7×7 interface, which showed a larger linewidth dispersion due to disorder at this interface (see Fig. 2.14(a)). Γ_0 is found to be about 90 meV larger on 7×7 (see Fig. 2.6). $\alpha = 0.028 \text{ eV}^{-1}$ at 50 K (0.037 at 5 K), $\Delta\Gamma_{e-ph} \simeq 26 \text{ meV}$, which is consistent with the values obtained on Pb- $\sqrt{3} \times \sqrt{3}$ and with the theoretical results.

The large $\Delta\Gamma_{e-ph}$ measured on both interfaces reflects a strong $e - ph$ coupling of the QWS in Pb thin films. A Debye model [78] with $\lambda_{bulk} = 1.55$ yields $\Delta\Gamma_{e-ph} = 23 \text{ meV}$, which is close to the measured averaged $\Delta\Gamma_{e-ph}$. The present *ab initio* calculations yields for most QWS $1.45 \leq \lambda \leq 1.6$. These values are larger than those computed for Pb thin films at E_F [81], but close to λ_{bulk} at E_F [78]. The excellent agreement between theoretical and experimental $e - ph$ coupling terms allows us to discriminate among the three contributions of Eq. (2.9). For 7-22 ML films the resulting electronic mean free path at E_F , $v_F\tau_0$ ($\Gamma_0 = \hbar/\tau_0$) can be estimated for both interfaces, yielding 3 – 4 nm for 7×7 and 11 nm for Pb- $\sqrt{3} \times \sqrt{3}$ ⁴.

Table 2.1(a), lists the terms contributing to Γ according to Eq. (2.9). Table 2.1(b) compares calculated (Fermi liquid theory) and experimental values for the parameter α for various materials. The $\Delta\Gamma_0$, the difference of Γ_0 between the 7×7 and the $\sqrt{3} \times \sqrt{3}$ interface, is about 90 meV. This $\Delta\Gamma_0$ found between the two interfaces reflect their different scattering properties, and this large interface scattering term emphasizes the crucial role of the interface for the determination of the QWS quasiparticle lifetime.

2.5.3 Comparison of the Γ_{e-e} with previous work and discussion

The extracted inverse lifetime (τ) shows a parabolic relation as a function of E as indicated by Eq. (2.10). The dependence of Γ to E^2 is consistent with 3D Fermi liquid theory. The

⁴Fermi velocities v_F are determined from the reconstructed band dispersion along $\Gamma - L$ [64].

Table 2.1: (a) The upper table shows extracted linewidth and its components at the two interfaces and at the two temperatures in this work. (b) The lower table compares our electron-electron scattering parameter to the parameters of other experiments.

(a) Material	$T(K)$	$\Gamma_0(meV)$	$\Delta\Gamma_{e-ph}(meV)$	$\alpha(eV^{-1})$
Pb/ $\sqrt{3}\times\sqrt{3}$ ^a	5	$\simeq 48$	24.6 ^b	0.033
	50	$\simeq 50$		0.033
Pb/ 7×7 ^c	5	$\simeq 139$	25.8 ^b	0.038
	50	$\simeq 142$		0.030
Pb Bulk ^d	5-50		23.2 ^b	0.020

(b) Elements	Calc. α ^d	Expt. α	Remarks
Pb	0.0200	0.0330	^a
Cu	0.0294	0.0385	STS on surf. state [83]
Ag	0.0399	0.0633	STS on surf. state [83]
Ag	0.0399	0.0260	PES on QWS [39]
Yb	0.0463	0.0463	STS on QWS [77]

^a Pb islands on $\sqrt{3}\times\sqrt{3}$ interface in this work.

^b $\Delta\Gamma_{e-ph} = (\Gamma_0 + \Gamma_{e-ph})(50K) - (\Gamma_0 + \Gamma_{e-ph})(5K)$.

^c Pb islands on 7×7 interface in this work.

^d Calculation of bulk from Debye Model or Fermi-liquid theory.

calculated parameter α is compared with experimental ones from various materials.

In table 2.1(b), we include a recent study of Yb/W(110) study done by Wegner *et al.*[77] presenting a study by STS on lifetime of QWS. In this study, the neglect of the interface and defects scattering term in the low-energy residual linewidth and a lack of temperature-dependent measurements, led the outcome to an erroneous determination of the $e-ph$ coupling constant ($\lambda \simeq 1.6 - 2.8$) [77]. In contrast, TR-2PPE measurements of the parent d -band in bulk Yb found $\lambda \simeq 0.4$ [84]. Moreover TR-2PPE results together with *ab initio* calculations reported a linewidth energy dependence far from being quadratic [84]. The complex band structure of Yb is mainly responsible for Yb films does not show Fermi liquid behavior. On the contrary, Pb films, having simple $s-p$ band structure, could fit into a Fermi liquid picture.

Recent 2PPE [75] investigations by Kirchmann *et al.* on unoccupied QWS in Pb islands on the $\sqrt{3}\times\sqrt{3}$ interface have revealed a fast decay lifetime (30-140 fs) (or equally inverse lifetime 22-4.7 meV) attributed to electron-electron scattering in the Pb film and a slow decay lifetime (130-900 fs)(or 5.1-0.73 meV) attributed to delayed filling of the states in the adlayer due to electronic relaxation in the Si(111) substrate. With our experimental α value of 0.033 and a QWS energy of 1 eV we obtain a value of 30 fs which

is in good agreement with their findings (20 fs at 1 eV QWS). The slow decay lifetime with a linewidth of a few meV is not accessible to STS, because it would correspond to a linewidth about a factor of 10 smaller than the experimentally observed one.

2.6 Conclusions and outlook

The present detailed STS study yielded insight into the electron dynamics of quantum well states. A careful lineshape analysis of the QWS allowed us to obtain quantitative information on the quasiparticle lifetime, the electron-electron and electron-phonon scattering as well as on the decisive influence of the interface between a metal thin film and the substrate on the linewidth. It is gratifying to note that the lifetimes found in the present investigations for the electron-electron scattering are in quantitative agreement with femtosecond time-resolved photoemission experiments. In principle, a quantitative comparison of lifetimes obtained by different experimental techniques requires a profound knowledge of the influence of the measuring process on the dynamical properties of quantum well states.

In conclusion, the combination of high-accuracy temperature-dependent STS experiments with *ab initio* calculations allowed us to identify individual QWS in single ultrathin metal islands, to separate consistently the different decay mechanisms of these electronic excitations and to determine the QWS electron-phonon coupling strength. These achievements open up an avenue toward detailed investigations of the decay processes of electronic excitations on a local scale, e.g. of individual supported molecules, clusters or other nanostructures.

For future work, we believe we have illustrated a reliable way to separate different scattering channels of the linewidth of QWS. Further studies to obtain a layer dependent relationship of the various scattering channels by STM/STS will offer valuable information on the electron dynamics of QWS. A variable temperature measurement for the linewidth of the QWS in a layer-by-layer way will be interesting it giving a *in situ* data of phonon coupling constant λ for each layer. Although there is PES data already [28, 40] in this aspect, STS data offer a comparison from a different point point of view. For the *e-e* scattering part, QWS energies and thicknesses are correlated and it's difficult to separate

the two variables. However, there is a coincidence of QWS energy at around 0.8 eV for several thicknesses of a Pb film (see Fig. 2.11), and a few other incidences else where. With careful experiments and larger amount of statistics, one might be able to find the layer dependent relations of the e - e scattering parameters by keeping the energy of QWS at a small variation.

Superconductivity in Ultrathin Pb Island Grown on Si(111)

The physical properties of conventional bulk superconductors have been studied for many decades and are understood in great detail [85]. On the other hand, the superconducting properties are expected to be modified as the superconductor evolves from a three-dimensional ($3D$) to a $2D$ or $1D$ system.

The fundamental question of how the superconducting properties of a material are modified if one of its dimensions is reduced down to a few atomic monolayers, has stimulated considerable theoretical and experimental interest since the 1960's [86–91]. Earlier experimental work on superconducting ultrathin films suffer from a lack of homogeneity of the thin film. At the thin-film limit, the behavior of the superconductivity accounts for connected grains of particles rather than for a crystalline ultrathin film [92].

Today with the emergence of nanoscience and nanotechnology, this question is of special relevance for possible technological applications in superconducting nanodevices. Recently, Pb films on a Si(111) substrate attracted much attention [93]. Using low-temperature deposition under ultra-high vacuum (UHV) conditions, layer-by-layer or bilayer-by-bilayer growth was achieved over macroscopic areas [28, 94]. These Pb films were protected by a capping layer to allow for *ex situ* resistivity [28] and magnetic susceptibility measurements [94]. A decrease of $T_c(d)$ with film thickness d as $-1/d$ was observed [94]. The data of Özer *et al.* allowed for an extrapolation to the known value of $T_c = 7.2$ K for bulk Pb. However, in contrast to these results, recent *in situ* STS investigations

on Pb/Si(111)- 7×7 islands reported no significant change in T_c upon thickness reduction [95, 96]. These contradictory experimental results called for an explanation.

Motivated by these contradictory results, we studied the low temperature properties of ultrathin lead islands on Si(111) employing low-temperature STM and STS. We have successfully produced single crystalline Pb islands of different size on the surface, and determine their size by STM. The QWS of the Pb island have been determined unambiguously by STS, and we can clearly determine the thickness of the islands by their height and their quantum well states in a layer-by-layer way. In order to probe the superconducting properties, low temperature investigations on this system at 4.6 K and 3.0 K were performed.

In this chapter, we report *in situ* STS measurements of the superconducting energy gap (Δ) of UHV grown single-crystal Pb islands on Si(111) in the thickness range 7-60 ML. Δ was found to decrease from its bulk value as a function of inverse island thickness. Corresponding T_c values, estimated using bulk gap-to- T_c ratio, are in quantitative agreement with *ex situ* magnetic susceptibility measurements [94], however, in strong contrast to previous scanning probe results [95]. Layer-dependent *ab initio* density functional calculations for free standing Pb films show that the electron-phonon coupling constant, determining T_c , decreases with diminishing film thicknesses.

3.1 Introduction to superconductivity in thin films

3.1.1 Earlier studies of size effects on superconductivity

The early model of Blatt and Thompson predicted an increase of the critical temperature (T_c) above the bulk value with decreasing film thickness [97]. However, if proper boundary conditions allowing for spill-out of the electronic wave functions in thin films are taken into account, a decreasing T_c with decreasing film thickness was predicted [88, 89, 98, 99]. Early experimental results usually showed a reduction in T_c for small film thickness [92]. However, the intrinsic origin of this behavior has been questioned because of structural disorder and by the non-uniformity of the metal films [92, 100]. Depending on the material, earlier experimental results showed either a decrease (Pb) or a increase (Al, Ga, Sn, In) in T_c on thin film thickness reduction [92, 101]. The reason of it is related to the

disorder in the film composed of metallic grains [92]. In contrast, pioneering experiments on crystalline Al films reported no T_c enhancement, allowing one to address thickness-dependent properties of crystalline superconducting films [102]. Therefore, there is a strongly different behavior of the critical temperature between a crystalline film and a thin film made of grains. The superconductivity of grain particles is associated to $3D$ confinement of the superconducting electrons. However, the problem we addressed here, superconductivity in a $2D$ crystalline ultrathin film, is more interesting because of its lack of clarity of the problem, the simplicity of the system and the abundance of theory.

3.1.2 Recent studies of size effects on superconductivity

Regarding the superconducting properties of ultrathin films, systems such as Pb/Si(111), allowed for the first time to address the intrinsic properties of crystalline thin films, of a controlled number of atomic monolayers in height but of macroscopic lateral sizes [28, 94]. Experiments performed before 1990, *e.g.* [103], reported a reduction of T_c with reduced film thicknesses. However later on, the suppression of superconductivity for the thinnest film was shown to be associated to the increasing role of disorder in these amorphous or granular thin films [92, 100, 104]. Hence with systems such as Pb/Si(111), we can take the advantage to study superconductivity in extremely clean, thin and uniform films, which makes a fundamental difference with earlier studies on amorphous and granular films [105].

There are several particular advantages for using Pb thin films as a candidate to study superconductivity at its thin film limit. Because the presence of QWS and obvious oscillation of the surface energy with every 2 ML, Pb thin films have strong tendencies to grow an atomically flat thin film on a macroscopic lateral scale [35] (see Sec. 2.1).

Photoemission experiments combined with transport measurements have recently reported that ultrathin lead films on Si(111) substrate show an oscillatory behavior of the superconducting transition temperature when the film thickness is increased by one atomic layer at a time [28]. From 30 ML to 15 ML T_c is found to gradually decrease from about 6.25 K to 5.0 K, whereas bulk $T_c = 7.2$ K.

A recent scanning tunneling spectroscopy (STS) measurements by Eom *et al.* [95], from 18 ML down to 5 ML, on the same system have found persistent quantum oscillations

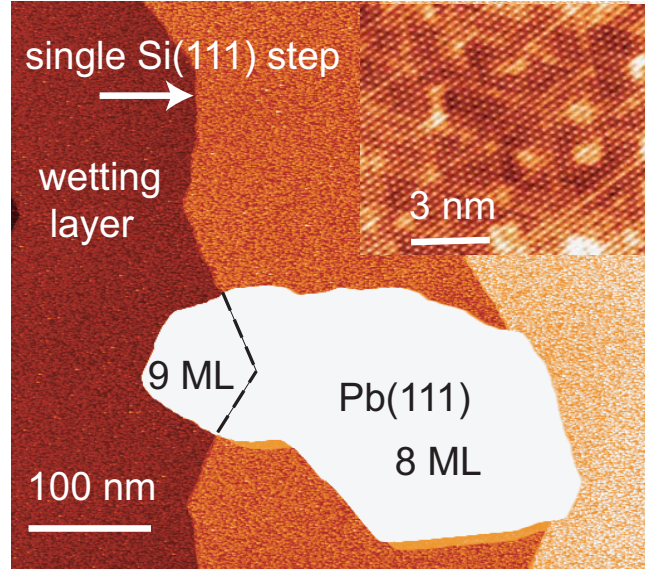


Figure 3.1: STM image of a flat-top Pb nanocrystal grown on Si(111)- 7×7 . The island extends over two substrate terraces. The dotted line locates the position of the substrate step separating the 9 ML thick from the 8 ML thick island. $V_{\text{bias}} = -1.0$ V, $I = 100$ pA. The inset shows a magnified view, revealing the Pb lattice with atomic resolution.

of T_c , (the relative variations are only of the order of 1% of T_c) around an average value of about 6.1 K, showing no sign of suppression of superconductivity for the smallest thickness studied. However, a recent susceptibility study [94] did not confirm such a thickness dependent behavior of the superconducting gap for 2D islands. In contrast to the results of Ref. [28], the latter shows reduction of T_c with reduced thickness. In addition, Eom *et al.* found gap values which were higher than the bulk ones.

On the other hand, lateral confinement of superconducting electrons in a nanostructures can be studied on small single crystalline Pb islands grown on Si(111). There are recent reports regarding superconducting properties with the lateral size of the Pb nanostructures and vortex confinement published by Nishio *et al.* [96, 106] and Cren *et al.* [107].

3.2 STM images of superconducting Pb islands

Cut PtIr wires were used as STM tips. All dI/dV measurements were performed with open feedback loop, using lock-in technique with a modulation voltage of 0.2 to 0.5 mV_{pp} at ~ 277 Hz, with a typical tunnel resistance of 15 $M\Omega$. The electrical connections to the STM chamber have been carefully RF filtered. STS is particularly sensitive to RF noise

when a spectroscopic resolution below 1 mV, as in the present case, is necessary [19, 108].

The preparation of the superconducting Pb islands is very similar to the preparation methods described in section 2.2. We have grown Pb islands on two different interfaces, 7×7 and $\sqrt{3} \times \sqrt{3}$ interfaces. We took advantage of the fact that the two interfaces favor different magic thicknesses [25, 58, 109, 110]. Indeed, certain thicknesses, which are not favored on the 7×7 interface, are formed on the $\sqrt{3} \times \sqrt{3}$ interface. The superconducting coherence length of bulk Pb is around $\xi_0 = 82 \text{ nm}$ (see Tab. A.1). For ultrathin Pb films, recent studies suggest a smaller coherence length than for bulk values. Özer *et al.* [94] determine $\xi_{GL}(0) = 23 \text{ nm}$ for a 9 ML Pb film, with a confirmation from Nishiro *et al.* ($\xi_{GL}(0) = 26 \text{ nm}$) [106] later. Cren *et al.* [107] also obtained $\xi_{eff}(4.3 \text{ K}) = 40 \text{ nm}$ on a 19 ML Pb island. We performed the measurement on islands with lateral dimensions much larger than the coherence length. This impedes measurement for every thickness because only some thickness are energetically favored. Part of the problem can be solved by growing islands on another interface as we mentioned earlier. We avoid to take data near the step edges or transition areas of thickness change on the islands to ensure the quality of the spectra.

Figure 3.1 shows a typical STM image of a flat-top Pb island extending over two substrate terraces separated by a single Si(111) step. This island consists of regions with a Pb thickness of 8 ML and 9 ML, respectively, in agreement with previous observations made on such quantum wedges [32]. The inset shows a magnified view of the Pb surface lattice with atomic resolution. The relative difference between the measured lattice constant and the bulk value is less than 10%. The observed superstructure, which is bias and Pb film thickness dependent, reflects the buried 7×7 interface [43].

The number of ML constituting each island was determined by addition of the apparent height with respect to the substrate and of the 1ML wetting layer. The energy onset of each QWS subband is characteristic of a given thickness, allowing for an independent Pb thickness determination [64]. The details of thickness determination are mentioned in Sec. 2.2.1.

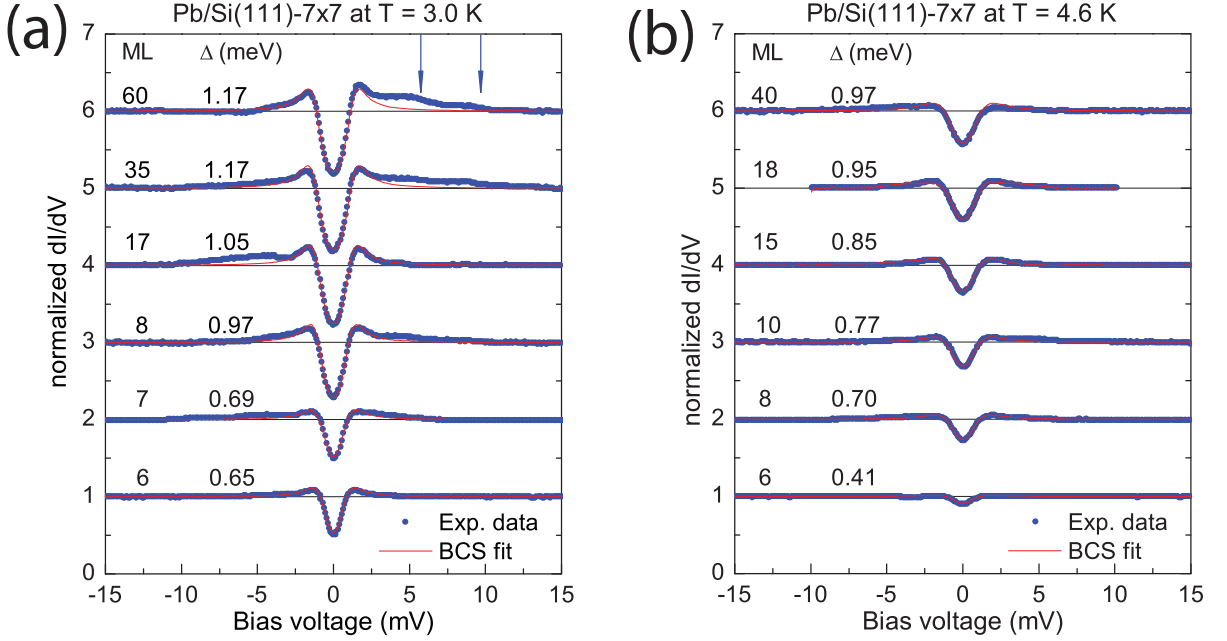


Figure 3.2: Experimental (circles) and calculated (continuous line) differential conductance spectra for tunneling between a PtIr tip and a large atomically flat Pb/Si(111)- 7×7 island of selected thickness. The spectra are vertically displaced for clarity. Continuous (red) lines: fitted conductance (see text), the quasiparticle gap Δ is indicated. (a) At 3.0 K, $\Delta_{Bulk}(3.0K) = 1.23 \text{ meV}$. (b) At 4.6 K, $\Delta_{Bulk}(4.6K) = 1.10 \text{ meV}$.

3.3 Superconductivity in Pb islands grown on Si(111)

3.3.1 Results

Figures 3.2(a) and (b) display the measured dI/dV spectra (circles), obtained by tunneling between the PtIr tip and the Pb island surface, for the indicated island thicknesses at temperatures $T = 3 \text{ K}$ and $T = 4.6 \text{ K}$. All the spectra shown in Fig. 3.2 are normalized to the normal state conductance (at $V_b = -15 \text{ mV}$). The spectra are vertically displaced for clarity. Both sets of spectra show a clear quasiparticle gap opening which increases from bottom to top. The slight asymmetry in the spectra below and above the Fermi energy E_F results from a nonlinear background conductance.

Each curve displayed in Fig. 3.2 is an average of more than ten individual dI/dV taken at various locations at the same individual island. On Pb islands grown on the 7×7 interface, the background conductance varies strongly from one location to another. This variation can be easily explained by the local disorder of the interface, which we see on the top of the island (see section 2.2.1) [32]. However, the spectral gap feature is preserved upon background correction. On both interfaces, we haven't observed striking

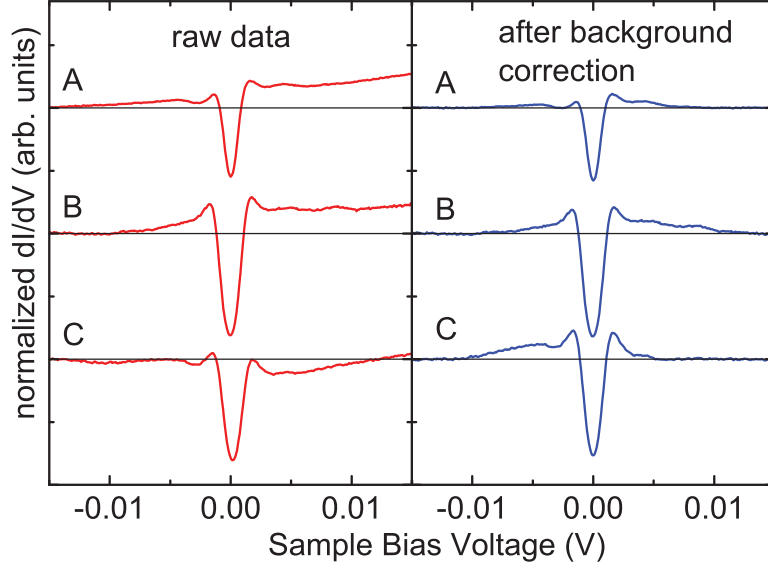


Figure 3.3: Raw dI/dV spectra of superconducting Pb island and the spectra after background correction. A, B and C spectra on the left and right column are the counter parts of the raw data and spectra after correction. In A and B, there are still tails of QWS cause a increase at the right side. In C, there is a pseudo gap as a background at larger energy scale than superconducting gap, which is consistent with the observation of Wang *et al.* [111]. Wang *et al.* explained the pseudo gap as a results of the electron-phonon scattering in a quantum well system.

local differences between spectra, agreeing with previous similar experiments [95, 96, 106].

The spectra in Fig. 3.2 have been corrected by subtraction of the background. We show raw data dI/dV spectra in Fig. 3.3(a) and the results after background correction in Fig. 3.3(b). The background is caused by the tails of QWS peaks (Fig. 3.3 A and B curve) or a pseudo gap (Fig. 3.3 C curve) as a results of the electron-phonon scattering in a quantum wells system. The observation of the pseudo gap was published by Wang *et al.* [111] recently. Two phonon modes, indicated by arrows in 3.2(a), are indicated in the spectra taken on the 60 ML films. Their energies correspond well to the values reported in the bulk Pb [112]. The phonon mode energies ($E_{ph} = E_{extrm} - \Delta$)¹ are 4.6 ± 0.2 and $8.5 \pm 0.2 meV$, which correspond well to the reported value [112](4.4 and 8.5 meV) for bulk Pb. In Fig. 3.4, we show the extracted phonon mode energy as a function of the thickness.

A thickness dependent phonon energy would be intriguing, but the conductance background and the weaker signals for thinner films make this analysis difficult. The closeness of a quantum well state to the Fermi level adds additional conductance background around E_F as well.

¹The phonon mode energy ($E_{ph} = E_{extrm} - \Delta$) is the value of the local extrema in d^2I/dV^2 (E_{extrm}) minus the value of the superconducting gap (Δ) [112].

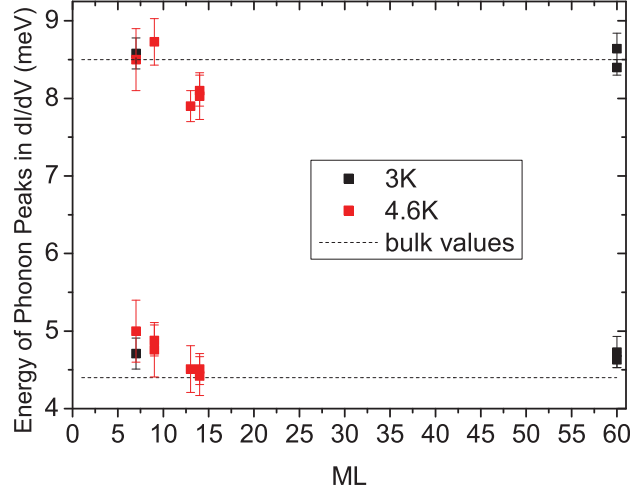


Figure 3.4: Energy of the phonon peaks extracted from the side peaks of the dI/dV spectra of the superconducting Pb islands. The extracted phonon mode energy are close the the bulk value. The observation of the phonon modes demonstrate the quality of the dI/dV spectra.

On the other hand, on the crystalline $\sqrt{3}\times\sqrt{3}$ interface, the dI/dV spectra are reproducible over the island at various locations (see Fig. 3.2(b)).

A quantitative analysis has been performed for the spectra obtained at 4.6 K and 3.0 K. The results, shown in figure 3.2(a) and (b) as red lines, describe convincingly the experimental data. The Δ value obtained for 40 ML at 4.6 K (0.97 meV) and 60 ML at at 3.0 K (1.17 meV) is close to the bulk value ($\Delta_{Bulk}(4.6\text{ K}) = 1.10\text{ meV}$ and $\Delta_{Bulk}(3.0\text{ K}) = 1.23\text{ meV}$). The observed relative reduction of the quasiparticle gap between 60 and 7 ML at 3.0 K (40 and 7 ML at 4.6 K) is $\sim 20\%$ ($\sim 30\%$). To this end the data for Pb islands with a thickness of 60 ML, practically at the bulk limit, are obtained at the lowest temperature available in our system ($T = 3.0\text{ K}$). The gap value (Δ) extracted from this analysis ($\Delta_{60ML}(3.0\text{ K}) = 1.17\text{ meV}$) is already very close to the bulk one at 3.0 K, $\Delta_{bulk}(3.0\text{ K}) = 1.23\text{ meV}$, which is the expected trend for thick Pb layers.

3.3.2 Modeling of the conductance spectra

In order to quantify the observed quasiparticle gap widths (Δ), a least squares analysis of the data is performed (red lines in Figure 3.2(a) and (b)) based on the standard expression for a tunneling junction between a normal metal and a superconductor [13]. We fit our spectra by Eq. (3.1-3.3). Eq. (3.2) is the ratio between the superconducting and the normal density of states (DOS) of quasiparticle excitations of the Pb sample (ρ_s). The

temperature broadening is described by the Fermi-Dirac distribution $f(E)$.

$$\frac{dI}{dV}(V) = -G_{nn} \times \int_{-\infty}^{\infty} \left(\frac{\rho_s(\epsilon)}{N(0)} \right) \times f'(\epsilon - eV) d\epsilon \quad (3.1)$$

G_{nn} is the Ohmic conductance of the junction.

$$\frac{\rho_s(\epsilon)}{N(0)} = \Re \left\{ \frac{|\epsilon|}{\sqrt{(\epsilon)^2 - \Delta^2}} \right\}, \quad (3.2)$$

$$f'(E) = \frac{\delta f(E, T)}{\delta E} \quad (3.3)$$

$f'(E)$ is the derivative of the Fermi-Dirac function.

The additional broadening introduced by the bias voltage modulation can be taken into account by a proper convolution as shown in Eq. (1.8-1.9) [13, 18]. The remaining RF noise voltage present in the tunneling junction was taken care of by an additional convolution, assuming a Gaussian distribution. We treat this Gaussian broadening by Eq. (1.10) [20]. The details are described in Sec. 1.3.2.

For strongly e - ph coupled superconductors, the lifetime of the quasiparticles may cause broadening of the superconducting tunneling spectra expressed in Eq. (3.4) below [113].

$$\rho_s(\epsilon) = \Re \left\{ \frac{\epsilon - i\Gamma}{\sqrt{(\epsilon - i\Gamma)^2 - \Delta^2}} \right\}. \quad (3.4)$$

In the case of a Pb bulk crystal, a BCS least-squares analysis of the tunneling spectra has been shown to require no Γ parameter [114]. Therefore, we did not consider this Dynes parameter (Γ) in our fitting. Intriguingly, one can think that the Γ factor causes similar effects as the RF noise in Eq. (1.10), although it would show different behaviors at lower temperatures [114]. We indeed employ Eq. (3.4) for preliminary estimations of the RF noise to save calculations time of multiple stages of integration in our fitting. We found a consistent Γ value for all the spectra, suggesting a consistent amplitude of RF noise present in our spectra.² We have got from various fit by Eq. 1.10 that our RF noise is a constant value, $\Gamma = 0.11\Delta_{bulk}(0\text{ K})$. We use Eq. (1.10) for the final determination of Δ and RF noise as it is exact, and we found a value for the RF noise here around $280\text{ }\mu\text{V}$.

² $\Gamma \sim 0.11\Delta_{bulk}(0\text{ K})$ was found for the analysis of the spectra measured at $T = 3.0\text{ K}$

3.3.3 DFT calculations for ultrathin Pb films

In order to unravel the mechanism responsible for the reduction of Δ with decreasing Pb film thickness, we have performed *ab initio* calculations³ of the electronic structure (bands and density of states), phonon spectra, and electron-phonon (*e-ph*) coupling properties such as the gradient of the one-electron potential, the spectral Eliashberg function, and the mass-enhancement parameter λ for free-standing Pb(111) films in the range of 4 to 10 ML and for bulk lead as well.⁴ We have also calculated the gap Δ and the critical temperature T_c by solving the full non-linear Eliashberg equations, and for comparison, the linearized gap equation of the Eliashberg theory [120]⁵. In both calculations the obtained T_c agree within $\pm 0.02 K$ for each Pb film thickness considered.

In contrast to the phenomenological Ginzburg-Landau theory [85] which can be applied only for film thickness larger than the coherence length of the sample, these *ab-initio* theoretical layer-dependent calculations of the critical temperature and of the energy gap take precisely into account quantum size effects on the electron and phonon band structure of the ultrathin Pb films. The evaluated ratio $2\Delta(0 K)/(k_B T_c)$ are within 2% of the 4.19 bulk ratio, except for the 4-layer Pb film where the deviation is close to 5%. We use the bulk ratio for determining the T_c from the measured gap Δ .

The results for the DOS and λ are summarized in Fig. 3.5. Between 4-10 MLs the variations in λ closely follow the variations in the electronic DOS at E_F and the variations in the theoretically determined T_c shown in Fig. 3.6. For the 5 ML film a quantum well state close to E_F results in a peak in the DOS, which causes the peak in λ . A corresponding maximum is also found for Δ and T_c (see Fig. 3.6). The comparison of the calculated values for the bulk and the 10 ML DOS at E_F and for λ suggests that also for thicknesses larger than 10 ML variations in the DOS at E_F are the main reason for variations in Δ

³The DFT calculations is performed by theoretic group based at San Sebastián of Spain[81].

⁴We use density functional perturbation theory in the local density approximation and pseudopotential approach with a norm-conserving scalar-relativistic pseudopotential. [115–118]. We employed periodically repeated vertically relaxed films of Pd(111) separated by 7 layers of vacuum. The lateral lattice constant was fixed to the theoretical bulk value of $a = 4.87 \text{ \AA}$. Valence states were expanded in plane waves up to a kinetic energy of 20 Ry. Surface Brillouin zone (SBZ) integrations were performed using 61 special points in the irreducible SBZ and the Gaussian smearing technique with a width of 0.2 eV. From the *ab-initio* *e-ph* coupling matrix elements we derived by Fermi-surface averaging the Eliashberg function $\alpha^2 F$, from which the average *e-ph* coupling parameter λ can be derived. Possible boundary effects on the superconducting state due to the small thickness are not included [119].

⁵The calculated $\alpha^2 F$ and the same effective Coulomb interaction parameter $\mu^* = 0.11$ for all slabs considered has been used.

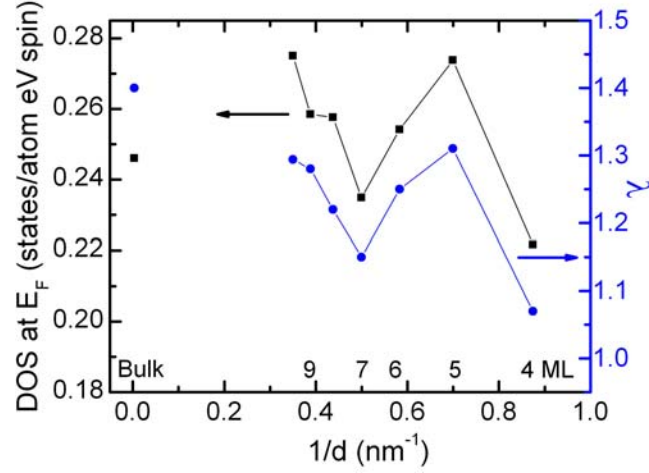


Figure 3.5: Calculated electronic DOS at E_F (squares) and electron-phonon coupling constant λ (dots) for 4-10 ML free-standing Pb thin films and for bulk Pb.

and T_c .

For all thicknesses studied theoretically, the largest contribution to the e - ph coupling originates from electronic states of p_z symmetry: both surface- and bulk-like p_z states contribute to λ . The states of in-plane symmetry, p_x and p_y , play a minor role in the e - ph coupling. The e - ph coupling matrix elements do not affect qualitatively the phonon DOS $F(w)$: the calculated Eliashberg function $\alpha^2 F(w)$ shows the same peak structure as the phonon DOS $F(w)$, all phonon modes contributing to λ . This result is in good agreement with the absence of significant changes in the measured phonon energies in the dI/dV spectra upon thickness reduction.

3.3.4 QSE on the superconductivity in Pb ultrathin islands

By measuring the STS spectra at 4.6 K and 3.0 K, we are able to observe the superconducting properties of these Pb nanocrystals for different thicknesses. The measurement of a superconducting gap in Pb of width of $2\Delta = 2.7 \text{ meV}$ required critical experimental condition to probe it with precision. By carefully choosing large crystals in the lateral dimension to avoid coherence length problems, by filtering the electronic noise, and by modeling the quasiparticle density of states (DOS), we found that the superconducting energy gap of Pb is reduced as a function of inverse island thickness (see Fig. 3.6). We interpret the reduction of T_c in terms of a reduced DOS at the Fermi energy and a corresponding change in the electron-phonon coupling constant.

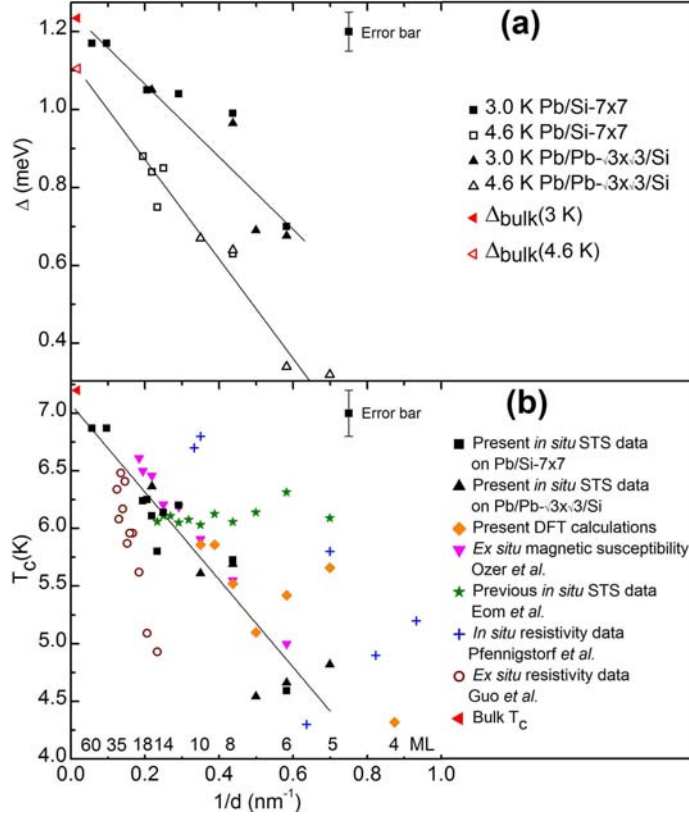


Figure 3.6: (a) Superconducting energy gap Δ as a function of inverse Pb island thickness $1/d$, extracted from BCS fits of the dI/dV spectra. Data for both crystalline (Pb/Pb- $\sqrt{3} \times \sqrt{3}$ /Si) and disordered (Pb/Si(111)- 7×7) interface are shown. Continuous lines are guide for the eyes. (b) Estimated critical temperature T_c as a function of $1/d$, using the bulk Δ/T_c ratio and assuming BCS temperature dependence of $\Delta(T)$. Thus this allows us to compare our experimental and DFT results with previous reports on T_c . We include results from Özer *et al.*[94], Eom *et al.*[95], Pfennigstorf *et al.*[121], and Guo *et al.*[28]. Continuous line is a fit to current STS data. For both (a) and (b), the error bars represent the experimental dispersion and uncertainty in the fit results.

To allow for a comparison with previous results found for T_c , we estimated the critical temperature (T_c) with the reasonable assumption that Δ follows the universal BCS temperature dependence for each thickness [85] and obeys the Pb bulk relation

$$2\Delta(0\text{ K}) = 4.19k_B T_c \quad (3.5)$$

T_c is derived from the fitted gap values and plotted as a function of the inverse thickness in Fig. 3.6(b). The continuous line in Fig. 3.6(b) is a linear fit to the STS data, leading to the relation

$$T_c(d) = 7.04 \times (1 - d_0/d) \quad (3.6)$$

with $d_0 = 1.88\text{ ML}$. Consequently, if we extrapolate our data to a thickness $\leq 2\text{ ML}$ the superconducting properties of Pb are expected to vanish. For comparison, we display the data from Özer *et al.* [94], Eom *et al.* [95], Pfennigstorf *et al.* [121], and Guo *et al.* [28]

together with the present data in Fig. 3.6. In a recent recent article , Qin *et al.* [122] observed superconductivity in a 2 ML Pb film. They determined T_c of the 2 ML film to be 4.9 K and 3.65 K for two different structures of Pb on Si(111). This result is consistent with our prediction that superconductivity of Pb thin film is still alive in a 2 ML film and is killed at 1 ML film.

We note that our results are in very good quantitative agreement with the data of Özer *et al.* [94], obtained *ex situ* on Ge capped Pb/Pb- $\sqrt{3} \times \sqrt{3}$ /Si(111). The present findings are also in qualitative agreement with the trend observed in *in situ* resistivity measurements of [121]. The quantitative deviation with this resistivity study is most likely caused by the inhomogeneity of the films. *Ex situ* resistivity measurements of [28] on Au capped Pb/Si(111)- 7×7 films show a much faster decrease of T_c with decreasing film thickness than in our case, probably a consequence of the inverse proximity effect induced in the Pb film by the Au capping layer [123]. The previous *in situ* STS results on Pb/Si(111)-(7×7 , Eom *et al.* reported an essentially constant T_c in this thickness range [95], are at variance of our data. However, in contrast to Eom's result, the results of ours [81] and the one of Weitering's *et al.* [94, 124] show a T_c to thickness relation following Eq. 3.6. Furthermore, our observed energy gap reduction is much larger in amplitude than the very small oscillations of T_c reported as a function of thickness by Eom *et al.*[95]; the oscillation amplitude is only 2% of the average T_c . While we can only speculate about the origin of the discrepancies between the results obtained by the previous STS measurements and the present ones, our experience with STS at low-temperatures at an energy resolution in the 1 meV range indicates that most probably residual radio frequency (RF) noise in the tunnel junction was present in the data of the former. In Eom's results, the peaks of the superconducting spectra appear broader than a genuine BCS spectra which is similar to the effects of the RF noise. A remaining RF noise can cause a determination of higher T_c than normal value which explains also that Eom's determined T_c is higher than ours and Özer's results. Therefore, we speculate that the reason of the discrepancies between the results is the pollution of RF noise in Eom's experiments. In conclusion still, much work remains to be done to elucidate the discrepancies between the measurements of superconductivity of the ultrathin film limit.

Although an oscillatory electron-phonon coupling constant of Pb thin films has been

reported [40], there is no clear signature of the role of the phonons in the reduction of T_c with decreasing material thickness. Consequently, more experimental and theoretical work will be necessary to elucidate the consequences of phonon confinement within nanostructures for the evolution of T_c in superconducting materials.

Figure 3.6 shows that the theoretical T_c are in agreement with the trend observed in the present STS data. The larger T_c found for the calculated 5 *ML* film is mainly ascribed to the presence of a quantum well state near E_F . This is consistent with the observation of an enhancement of T_c on a 5 *ML* Pb island on the $\sqrt{3} \times \sqrt{3}$ interface. Moreover, below a thickness of 6 *ML*, the interaction with the substrate is expected to increasingly modify the electronic band structure and thus the DOS at E_F , λ , Δ , T_c of these ultrathin films, an effect not included in the calculations for free-standing films. This could explain the difference between experimental and DFT calculated T_c for thicknesses below 7 *ML* in Fig. 3.6. Experimentally, this effect is clearly seen by the larger discrepancy arising at small film thickness between the calculated [34] and our measured QWS energies of Kirchmann *et al.*[41] and our results (see Fig. 2.11).

The origin of the increasing influence of the substrate on the DOS and λ with decreasing film thickness is the increasing role of the interaction of the substrate with the Pb film. With decreasing film thickness, the number of electrons and phonons also decreases resulting in the relative increase of the states modified by the Pb film/Si substrate interaction. An analogy is, with decreasing film thickness, the surface/interface to bulk ratio increases substantially at the thin film limit. This, in turn, cause modification in Δ , T_c , and λ . The thinner the film, the stronger the modification.

For thin Pb islands on Si(111) the experimentally observed reduction of the critical temperature (T_c) with decreasing film thickness (d) is consistent with first principle results of thickness dependent *e-ph* coupling constant λ . When d is close to the ultrathin Pb film limit, the variation of DOS at E_F plays a decisive role affecting both λ and T_c . The origin of the "oscillation" of T_c is the behavior of the electron density of states at E_F . For 4 *ML* film, the DOS at E_F is quite small. For 5 *ML* film, the DOS increase in a large amount due to a QWS arising at E_F . For 6 and 7 *ML*, T_c drops again. All the calculated quantities, which reflect the electron-phonon coupling, T_c , Δ , behave in a similar way.

3.4 Conclusions and outlook

For thin Pb islands on Si(111), the experimentally observed reduction of the superconductin energy gap with decreasing film thickness is consistent with the first principle results of a thickness-dependent e - ph coupling constant λ , where close to the ultrathin Pb film limit the variation of the density of states at E_F play a decisive role. Interestingly, both atomically smooth (Pb/Pb- $\sqrt{3} \times \sqrt{3}$) and disordered (Pb/Si(111)- 7×7) interface yield similar experimental behavior, in agreement with results showing that both systems are in the diffusive limit [94, 106].

For future work, investigating superconducting properties in lower dimensions and in small structures is an obviously interesting topic [105, 122]. The relations between superconductivity and the size and shape of the nanostructures can be revealed in a clear way that was not possible until recent years [96, 106, 107]. Demonstrating the ideas of superconducting vortex confinement and vortex motion has become possible in this system [106, 107]. One can also investigate the evolution of superconductivity from the clean limit to the dirty limit for a specific geometry of a superconducting nanostructure. Proximity effects can be measured in a cleaner condition in this system than the previous results [125–127]. This is a fast developing and challenging field for researchers well equipped with a ultra-low temperature STM.

Metallic Coulomb Islands

The observation of single electrons was demonstrated by R. A. Millikan in 1910 by oil-drop experiments, but it was not until the late 1980's that one could manipulate single electrons in a solid-state circuits. Although some important work concerning single electron manipulation had been done during these periods [128, 129], until recent decades, thin-film and semiconductor processing techniques were not advanced enough for the required precise positioning of electrode and particles. After the necessary fabrication technique had been established [130], a new field – single electron electronics – took off and attracted a large amount of attention due to its superior sensitivity and extreme low energy consumption. For general reviews of single electron tunneling of particles and quantum dots, please see [131–136]. Along with the experimental development, the theory of single electron tunneling has been also established [132, 135, 137].

At first we were motivated to investigate properties of superconducting nanocrystals with finite size. However, in the course of the study, we found that we arrived in a field that is important but not yet well studied by the STM community. We observed well defined metallic islands located on crystalline dielectric layers. Single electron tunneling in the Coulomb blockade regime has been well studied in planar junctions by embedding a particle in an insulating layer between two electrodes. A very good review article in this field was written by von Delft *et al.* [136]. Nevertheless, the size and shape of the particles were basically unknown. Utilizing the ability to determine geometry and to perform local spectra by STM/STS, it will be very fruitful to investigate the physics of quantum dots and single electron tunneling. Measuring insulated nanocrystals by STM

offers the tremendous advantage of giving information on the detailed geometries of the nanostructures and electronic properties at the same time. The dielectric layers can be grown with control in a layer-by-layer way [16, 138–140]. The thickness of the dielectric layers can be determined from the capacitance of the island. The thickness can also be verified by tunneling spectra featuring image potential states [16]. Previous studies of quantum dots in the Coulomb blockade regime by STM were measured on amorphous particles [141–143], particles covered by ligands/molecules/shells [144–149], and only very few on clusters/nanostructures [150–153]. Among these studies, the geometries of these nanostructures are either too small or to be determined by STM or are amorphous clusters without well defined shapes.

Based on the orthodox theory of single electron tunneling [85, 154, 155], we were able to simulate (or fit if circumstances allowed) the tunneling spectra and to extract all the parameters of the double barrier tunneling junction (DBTJ); those are the resistances of tip-island and island-substrate junctions (R_{tip} and R_{sub}), the capacitances of tip-island and island-substrate junctions (C_{tip} and C_{sub}), and the residual charge (Q_0) in the island (see Sec. 4.2). Thus the junctions were well characterized quantitatively.

In the work presented in this chapter, we produced Pb nanocrystals on NaCl/Ag(111) (see Sec. 4.3). The NaCl dielectric layer can be fabricated with thickness between 1 to several ML in a controlled layer-by-layer manner. With the well-defined Pb nanocrystals supported on well-defined insulating layers, we investigated single electron tunneling properties in this system (see Sec. 4.4). The tunneling spectra of metallic Coulomb islands clearly show single electron tunneling characteristics. For selected Pb nanocrystals on NaCl, the local I-V curves show a clear coulomb staircase, revealing that we could count every additional electron tunneling to or from the Pb island one by one.

The results of our measurement are promising. We can observe many features in the tunneling spectra, *e.g.* simple Coulomb blockade, multi-level Coulomb staircase, or the interplay of the two capacitances, depending on the parameters of the two junctions (see Sec. 4.4).

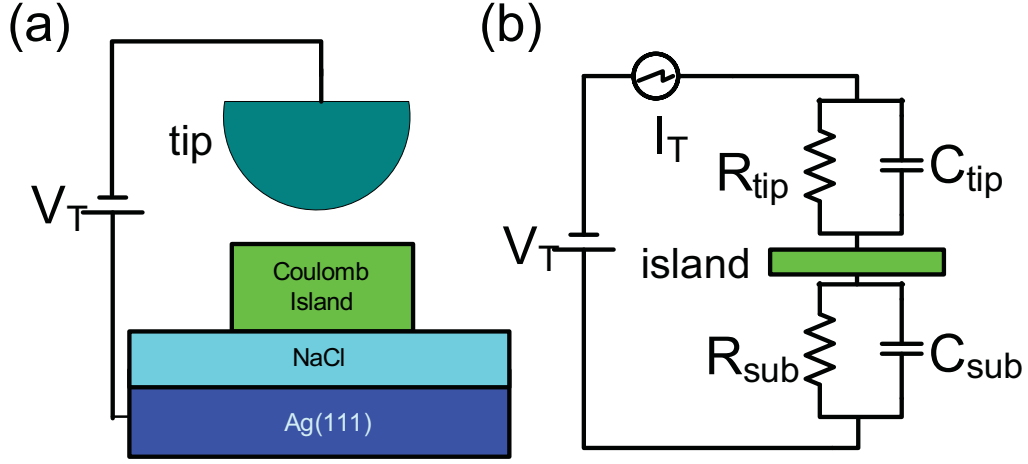


Figure 4.1: (a) Schematic diagram of the Coulomb blockade system. The Coulomb island is placed between the vacuum barrier and NaCl dielectric layers. (b) Schematic diagram of the double-junction circuit. Each junction can be represented by a set containing a capacitor and a resistor.

4.1 Introduction to Coulomb blockade and Coulomb staircase

Single electron devices utilizing the Coulomb blockade effects have attracted much attention since its discovery by Fulton *et al.* [130] in 1987. Focusing here on metallic rather than semiconducting systems, we realize a Single Electron Box (SEB) in a STM junction accompanied by an insulating barrier (NaCl layers) separating the metallic nanocrystals (Pb and Ag in this project) from the substrate (Ag(111)). One can see the schematic configuration of our experimental setup and electric circuit in Fig. 4.1. In Fig. 4.1(a), the two barriers, the vacuum between tip and island as well as the dielectric layers between island and substrate, constitute the double barriers of the DBTJ. In each barrier, one can represent the barrier by a combination of a capacitance and a resistance, as shown in Fig. 4.1(b). We do not have a gate electrode in our system comparing to which a planar junction [156] have. However, the non-zero residual charge (Q_0) acts like a gate voltage. Although one can not control it in a dedicated manner, Q_0 can be changed simply by a bias voltage pulse.

The "Coulomb blockade" or "Coulomb staircase" [130, 155] refers to modifications of the tunneling $I(V)$ curves which occur in junctions with capacitances sufficiently low, so that the Coulomb charging energy $E_C = e^2/2C$ of a single electron is large enough to play a major role. We show simulated conductance spectra in Fig. 4.3(a) and (b) for a Coulomb blockade and (c) and (d) for a Coulomb staircase.

Although bulk Pb is superconducting at the temperature where we perform our mea-

surement ($T = 4.6 K$), we can neglect the superconducting gap because the energy scale of the Coulomb gap is much larger than the superconducting gap. We shall restrict these effects to the tunneling junctions in the normal state without considering superconductivity in this chapter.

To clearly observe the Coulomb blockade or the Coulomb staircase in the junction, two conditions described below have to be met.

(i) Thermal broadening. The charging energy ($e^2/2C$) must be much larger than the thermal energy ($k_B T$), this condition implies that we must work with very small metal islands and/or at low temperature in order to observe the Coulomb blockade.

$$\Delta E_C = \frac{e^2}{2C_\Sigma} \gg k_B T \quad (4.1)$$

Assuming we work at $T = 4.2 K$, the thermal energy is $k_B T = 0.362 meV$. Therefore a total capacitance of $C_\Sigma \ll 443 aF$ ($aF = 10^{-18} F$) is needed. In general, the total capacitance has to be in the range of $10 \sim 50 aF$ to observe a tunneling spectrum with a clear Coulomb gap. Consider a 3 ML NaCl film with a height of 8.5 \AA (see Table A.1) and dielectric constant 5.9 (bulk value) (see Tab. A.1). In order to reach a capacitance value higher than $10 aF$, one needs an island with an area smaller than $163 nm^2$, that corresponds to a equilateral triangle with length $19 nm$ calculated by Eq. 4.2. There are rare examples of observing a Coulomb blockade with STM at room temperature [150]. Those cases concern usually very small metal clusters with approximately hundreds of atoms.

$$C = \epsilon \frac{A}{d} = \epsilon_0 \epsilon_r \frac{A}{d} . \quad (4.2)$$

(ii) Coupling resistance. The coupling resistance of each junction has to be significantly larger than the quantum resistance ($h/4e^2$) in order to keep charge fluctuations sufficiently small.

$$R \gg R_Q = \frac{h}{4e^2} \approx 6.5 k\Omega \quad (4.3)$$

Even if one already has the STM barrier as one of the barriers, fulfillment of both conditions simultaneously is a challenging experimental task for an STM measurement. The problem is related to two aspects; (i) the metal droplet and the insulating layers are usually rough and not well defined crystalline structures, and (ii) the STM has difficulties working on insulators. Fortunately in this lab, we have the expertises to fabricate ultrathin

insulating layers supported by a metal substrate for UHV STM measurements [16, 139]. Furthermore, the previous QWS studies (in Chapter 2) of Pb nanocrystals offer us a solid background for the microscopic characterization of the Pb islands.

4.2 The orthodox theory of Coulomb islands

Within the context of single electron tunneling, the "orthodox theory", a semi-classical theory, is widely recognized as an efficient way of explaining most of the experimental results. For a particular case, the theory was developed by Kulik and Shekhter [157]; later it was derived from more general approaches and generalized to other systems [85, 135, 154, 155]. The validation of the orthodox theory is based on the following three assumptions [137].

(i) Neglect of quantum confinement. The electron energy quantization inside the conductors is ignored, i.e., the electron energy spectrum is continuous. It can be described as (Eq. (4.4)), where E_k is the quantization energy of the Coulomb island.

$$E_k \ll k_B T . \quad (4.4)$$

Frequently it is also described as

$$E_k \ll \Delta E_c \text{ with } \Delta E_c \text{ shown in Eq. (4.1)}. \quad (4.5)$$

(ii) High Resistance. Coherent quantum processes consisting of several simultaneous tunneling events ("cotunneling") are ignored. This assumption is valid if the resistance of all the tunneling barriers of the system is much higher than the quantum unit of resistance R_Q (see Eq. (4.3)). Only in this condition the quantum-mechanical uncertainty of electrons is suppressed because of the high tunneling resistance (*i.e.* less tunneling events). Thus one can neglect the concurrent tunneling events and treat one electron at a time, which makes controllable single-electron manipulation possible.

(iii) Neglect of the tunneling time through the barrier. The tunneling time τ_t of an electron tunneling through the barrier is assumed to be negligibly smaller than other time scales (including the interval between subsequent tunneling events). For a typical tunneling event in a practical junction [137], τ_t is around 10^{-15} s . For a typical STM tunneling junction with 1 nA tunneling current, on average one electron tunnels per 10^{-10} s .

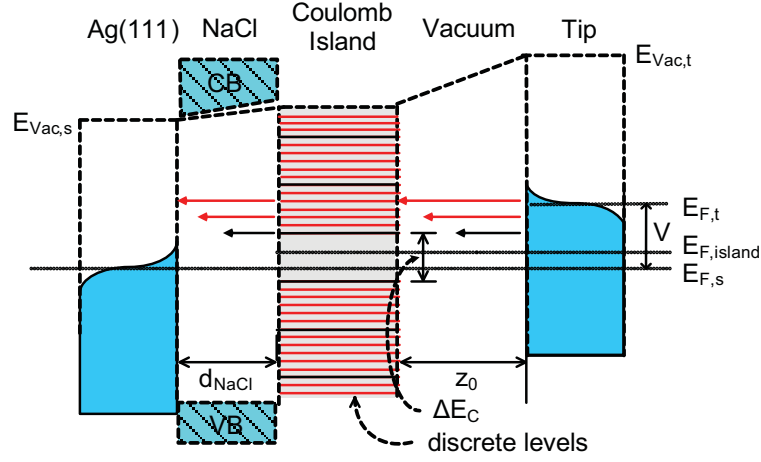


Figure 4.2: Schematic energy diagram of the double barrier tunneling junction (DBTJ) and a metallic Coulomb island between the junctions. Density of states (DOS) of the island consists with discrete energy levels of quantum confinement (red lines). Black lines indicate coulomb levels and $\Delta E_C = e^2/C_\Sigma$ is the Coulomb charging energy (see text), indicated by black lines. Fermi level of the island ($E_{F, \text{island}}$) is shifted because the decoupling between the island and the two electrodes ($E_{F, \text{island}}$ and $E_{F, s}$ are the Fermi level of the tip and sample respectively). Vacuum levels of the tip and the sample ($E_{vac, t}$ and $E_{vac, s}$) are also indicated.

Considering that the electronic lifetime of an electron in the states of the islands is around $10^{-13} - 10^{-15} \text{ s}$ (see Chapter 2), we conclude that electrons tunnel one at a time and we can neglect the interaction of the electrons tunneling simultaneously.

We mainly follow the approach documented in the literature ([85, 154, 155]) for our modeling. In the following paragraphs, the orthodox theory we used for our modeling will be briefly introduced. Assuming the DOS of tip and Ag(111) substrate is flat, the tunneling spectra can be used to investigate the electronic structure of the metallic Coulomb island. In this chapter, we have used Pb and Ag islands/clusters as materials for the Coulomb islands.

Consider that we have a double barrier tunneling junction (DBTJ) as shown in Fig. 4.2. The two barriers, the vacuum and the NaCl dielectric layers, separate the metallic Coulomb island from the two electrodes. One notices that with only the condition of DBTJ, we fulfill the condition (ii) described above. If the size of the island is small enough to let capacitance be sufficiently small (cf. Eq. (4.2)), then it makes the charging energy ΔE_c (Eq. (4.1)) large enough to overcome the thermal broadening in order to be observed.

In Fig. 4.2, we indicated the energy levels of the Coulomb island with two categories; the charging Coulomb energy ΔE_c (black line) and the discrete energy levels (red lines)

from the quantization of the energy levels (QWS) of the small island. For a bias voltage within the first Coulomb level around the Fermi level of the island, the tunneling is prohibited because of the Coulomb blockade. The tunneling spectra is shown in Sec. 4.4.

We therefore conclude here that the tunneling junctions we describe here are in the Coulomb blockade regime and the orthodox theory is valid.

Concerning condition (i), the quantized energy of the metallic island in our system can be separated into vertical (z) and lateral (x and y) directions in our ultrathin islands because we have flat top crystalline islands. In the vertical direction, the energy quantization yields the quantum well states (QWS), with ΔE around 1 eV at a thickness of 10 ML (see Fig. 2.11). Thus $E_{k,z}$ is much larger than $k_B T$. Although this contradicts condition (i), the characteristics of Coulomb staircases still show up in our spectra and we can treat the QWS as a background. On the other hand, energy quantization due to the lateral confinement ($E_{k,\parallel}$) appears to be much smaller than E_c in our system. Nevertheless, we can still see the lateral discrete energy levels ($E_{k,\parallel}$) in the STS spectra featuring a Coulomb staircase, observed as additional fine structures in the spectra.

Both types of energy levels due to vertical and lateral confinement are not included in the modeling here. A full account of these factors should include the density of states (DOS) of the island in a convolution integral with the tunneling matrix element. A review article of *Banin et al.* [158] describes in details this approach, which we did not adopt here.

NaCl serves as a dielectric spacer layer for separating the Coulomb islands from coupling with the metallic substrate. The obtained spectra are well within the band gap of NaCl. For the details of the bandstructure of NaCl, see Sec. 4.3.2.

The Fermi level of the island ($E_{F,isl}$) is aligned neither with the Fermi level of the sample ($E_{F,s}$) nor with Fermi level of the tip ($E_{F,t}$), but determined by the ratio of the capacitance as Eq. (4.7) shows.

$$C_{\Sigma} = \sum_i C_i \quad (4.6)$$

$$\begin{aligned} E_{F,isl} &= E_{F,s} + eV_t \frac{C_{tip}}{C_{\Sigma}} \\ &= E_{F,t} - eV_t \frac{C_{sub}}{C_{\Sigma}} \end{aligned} \quad (4.7)$$

We now consider the case shown in Fig. 4.1(b), the energy required to tunnel an electron from junction 1 (or junction 2) to the island from state (n) to $(n \pm 1)$ is shown below [85, 154].

$$\Delta E_1^\pm = \frac{e^2}{C_\Sigma} \left\{ \left[\frac{1}{2} \pm \left(n - \frac{Q_0}{e} \right) \right] \pm \frac{C_2 V}{e} \right\} \quad (4.8)$$

$$\Delta E_2^\pm = \frac{e^2}{C_\Sigma} \left\{ \left[\frac{1}{2} \pm \left(n - \frac{Q_0}{e} \right) \right] \mp \frac{C_1 V}{e} \right\} \quad (4.9)$$

Here in Eq. (4.8), for example, it requires energy $\Delta E_1^+(n)$ to tunnel an electron from junction 1 to the island, bringing the island from (n) to $(n + 1)$ electrons. Then, it takes $\Delta E_2^-(n + 1)$ of energy for the electron to tunnel out from the island via junction 2. In another way, it can also take energy $\Delta E_2^-(n)$ to tunnel out from the island via junction 2, bringing state (n) to state $(n - 1)$, and then with the energy $\Delta E_1^+(n - 1)$ one electron tunnels from junction 1 to the island, bringing the island back to state (n) . The sum of the two ΔE values for a full passage of charge is always exactly eV , so that the energy of the electron is always lowered by $|eV|$ overall.

In a particular case for the bias voltage lower than the threshold, there is not enough energy for the electron to overcome the static electric potential, and thus the Coulomb blockade occurs. The threshold voltage is

$$V_{th,1}^+ = \frac{-e}{C_2} \left[\frac{1}{2} + \left(n - \frac{Q_0}{e} \right) \right] \quad (4.10)$$

$$V_{th,2}^- = \frac{-e}{C_1} \left[\frac{1}{2} - \left(n - \frac{Q_0}{e} \right) \right] . \quad (4.11)$$

In Eq. (4.10), the value of Q_0 is also a factor to determine the threshold voltage. When Q_0 is $e/2$, there is no Coulomb blockade at all. Depending on the parameters, the smaller one of the threshold voltages $V_{th,1}^+$ and $V_{th,2}^-$ can determine the Coulomb gap or both threshold voltages can determine the gap asymmetrically [154].

Considering the finite temperature and dynamics of the tunneling, we can write the tunneling probability [85] in Eq (4.12). The tunneling rate in general is proportional to $1/R_j$ (the resistance of the j junction) and includes the considerations of finite temperature

and dynamics of charging and discharging.

$$\Gamma_j^\pm(n) = \frac{1}{R_j e^2} \left[\frac{-\Delta E_j^\pm}{1 - \exp\left(\frac{\Delta E_j^\pm}{k_B T}\right)} \right] \quad (4.12)$$

At a given bias voltage, the energy change by tunneling an electron through junction j is described in Eq. (4.8), thus one can define an ensemble distribution of the number of electrons at the Coulomb island as $\sigma(n)$ in Eq. (4.13). One can also understand $\sigma(n)$ as a probability density of electrons in the island. One can get $\sigma(n)$ by solving Eq. (4.13) and normalize it by Eq. (4.14).

$$\sigma(n) [\Gamma_1^+(n) - \Gamma_2^+(n)] = \sigma(n+1) [\Gamma_1^-(n+1) - \Gamma_2^-(n+1)] \quad (4.13)$$

$$\sum_{n=-\infty}^{\infty} \sigma(n) = 1. \quad (4.14)$$

Therefore, the tunneling current can be written as Eq. (4.15).

$$\begin{aligned} I(V) &= e \sum_{n=-\infty}^{\infty} \sigma(n) [\Gamma_2^+(n) - \Gamma_2^-(n)] \\ &= e \sum_{n=-\infty}^{\infty} \sigma(n) [\Gamma_1^-(n) - \Gamma_1^+(n)] \end{aligned} \quad (4.15)$$

This approach described here is the so-called "orthodox theory". We then can compare our experimental data to the simulated results generated by Eq. (4.15) (see Sec. 4.4).

A set of simulation results generated by Eq. (4.15) and its numerical differential is presented in Fig. 4.3. The evolution of a Coulomb blockade to a Coulomb staircase is shown in Fig. 4.3(e-f). In practice, C_{tip} would change with lower R_{tip} since the tip is closer to the island, although this factor is not considered here and the change of C_{tip} appears to be small (see Fig. 4.9). It corresponds well to the experimental results shown in Sec. 4.4 by changing the initial tunneling current for measuring the spectra (see Fig. 4.7).

Based on this theory, we can reproduce the general features of the measured spectra revealing Coulomb blockade properties. Furthermore, we can determine quantitatively every parameter in the double barrier system: the capacitance of both junctions, the resistance of both junctions, and the residual non-integer charge Q_0 in the Pb island. Considering the permittivity of NaCl, we can also determine the thickness of the under-

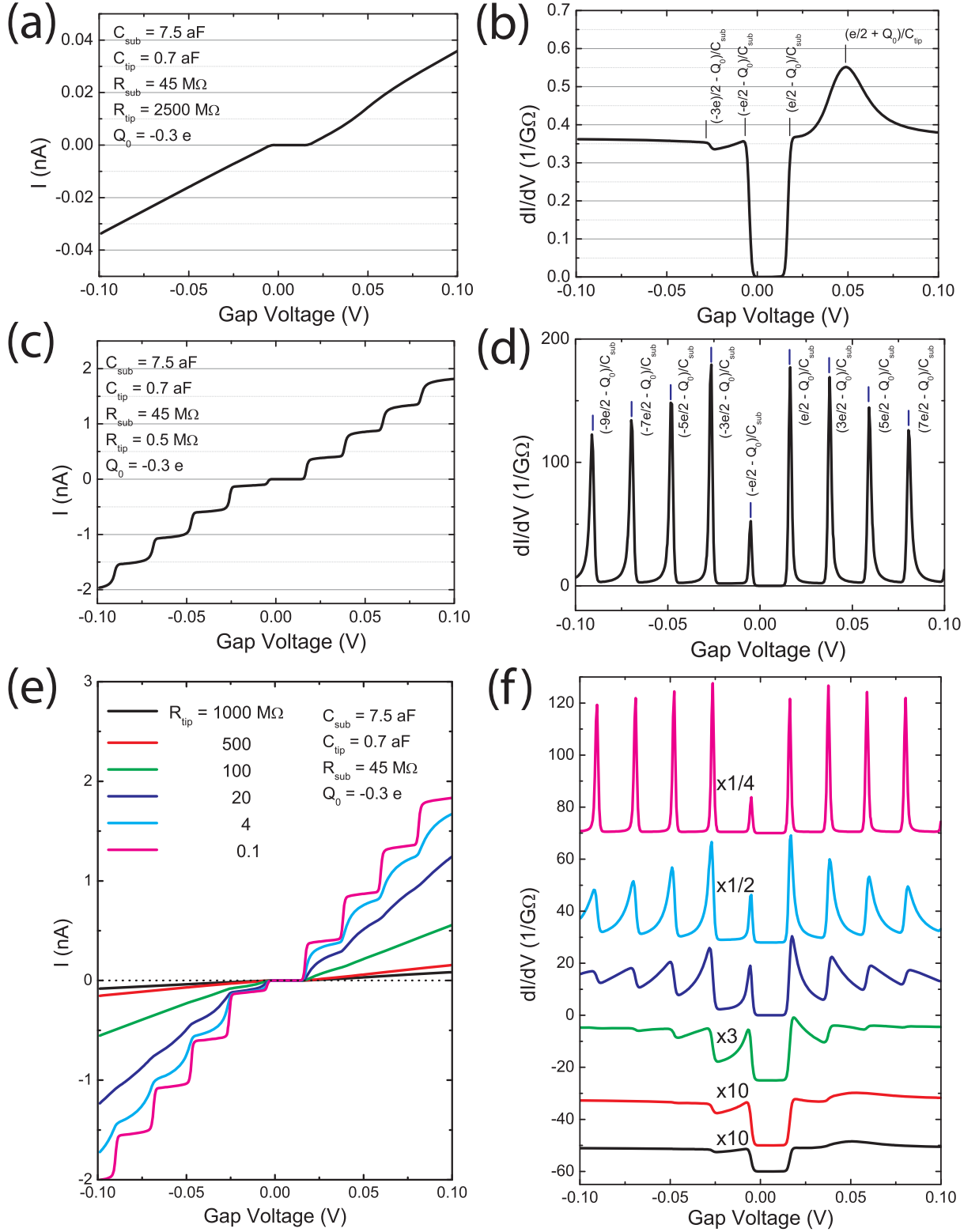


Figure 4.3: Simulation of tunneling spectra of a Coulomb island based on orthodox theory by using Eq. (4.15). Here, we change only R_{tip} , *i.e.* setup tunneling current (I_{set}), and fix the other parameters of the DBTJ. (a), (c) and (e) are curves of tunneling current and (b), (d), and (f) are their corresponding differential conductance. (a) and (b) indicate the case of high R_{tip} with appearance of Coulomb blockade of electrons with energy between the Coulomb gap. (c) and (d) illustrate the case of low R_{tip} , hence high tunneling current. (e) and (f) show the evolution of Coulomb blockade to Coulomb staircase, which can be achieved by approaching the tip by increasing I_{set} when measuring the spectra. This simulation corresponds well to the experimental data (see Sec. 4.4).

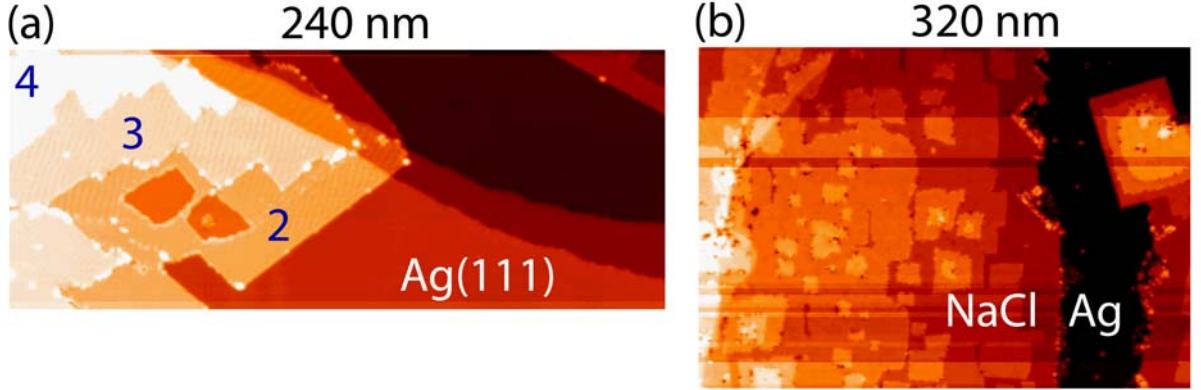


Figure 4.4: STM images of NaCl layers deposited on a Ag(111) substrate. The size indicated corresponds to the width of the image. (a) 2 – 4 *ML* of NaCl islands (thickness indicated by numbers) grown in a rectangular shape on Ag(111). Moiré patterns of 2 – 3 *ML* NaCl are visible. $V_{bias} = 2.5\text{ V}$, $I = 20\text{ pA}$. (b) An overview at higher coverage of NaCl on Ag(111). $V_{bias} = 3.2\text{ V}$, $I = 20\text{ pA}$.

lying insulator NaCl.

4.3 Experimental details and STM images

The experiments are performed on a homebuilt STM operated at 4.6 *K*. dI/dV measurements were performed with an open feedback loop using a lock-in technique with modulation voltage from 0.2 – 10 mV_{pp} at 300 – 400 *Hz* frequency with tunneling current ranging from 100 *pA* to few *nA*. In order to compare both $I(V)$ and dI/dV with the simulation results and using the superior sensitivity of the dI/dV spectra measured by lock-in amplifier, we scaled the lock-in dI/dV to match the numerical dI/dV . The numerical dI/dV curves were calculated by performing numerical differential of $I(V)$ curves. We noted the calibrated dI/dV with real units ($1/G\Omega$) on the y axis of graph instead of arbitrary units.

4.3.1 Sample preparation and STM images

As Fig. 4.1(a) shows, we produced small metallic islands on top of NaCl layers supported on a Ag(111) substrate. The Ag(111) single crystal substrate was cleaned by Ar sputtering and subsequent annealing. For deposition of NaCl, NaCl powder in a crucible of an evaporator was thermally heated to $T = 620^\circ\text{C}$ and was evaporated on the Ag substrate held at room temperature.

The NaCl layers grown on Ag(111) show the NaCl(100) surface because otherwise,

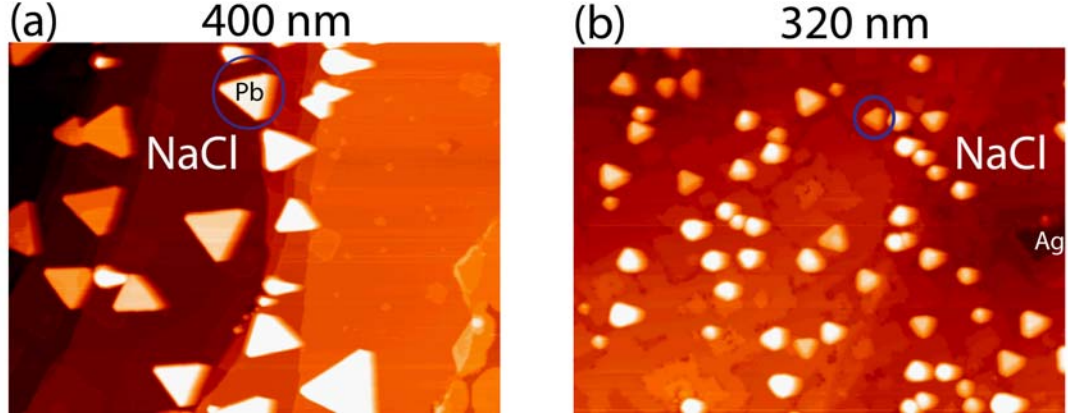


Figure 4.5: STM images of Pb islands grown on NaCl layers on a Ag(111) substrate. The size indicated corresponds to the width of the image. Pb islands are visible in both images, with most of them with triangular shape and few with rounded shape. We obtained larger islands in (a) with higher coverage of Pb, in contrast to smaller islands in (b) with less coverage. In (a), the length of the circled equilateral triangular island is 32 nm , and in (b) it is 6.4 nm . Substrate temperature is $\sim 130\text{ K}$ in both cases.

such as NaCl(111), the surface is not electrically neutral and thus unstable. A surface of NaCl(100) is an *apolar* surface because it consists of equal amounts of Na^+ and Cl^- . A surface of NaCl(111) would consist of either Na^+ or Cl^- only, and becomes a *polar* surface. Therefore, despite the lattice mismatch, NaCl(100) is energetically favorable for growth on various substrates [159, 160]. It was only recently that NaCl is used as a spacer layer for molecule support (*e.g.* [161, 162]), and characterization of NaCl layers became interesting for the STM community. To our knowledge, no STM study of NaCl on Ag(111) has been reported yet. Nevertheless, some studies of NaCl on other substrates can still provide us with details of the NaCl layers (*e.g.* [16, 140, 163, 164] on Ag(100), [161, 162, 165] on Au(111), [159, 166] on Al(111)).

Figure 4.4 shows STM images of NaCl layers grown on a Ag(111) substrate. In Fig. 4.4(a), 1 – 4 *ML* of NaCl islands are found on a Ag(111) substrate. Moiré patterns are observed on 2 and 3 *ML* NaCl layers. Because the crystal structure of the substrate is hexagonal and the structure of the NaCl is rectangular, the Moiré pattern, caused by superposition of the two lattice structures, appears as stripes. In Fig. 4.4(b), a sample with a higher coverage of NaCl is shown. NaCl islands prefer growth starting from 2 *ML*, and 1 *ML* NaCl islands are rarely found.

A determination of the thickness of NaCl layers at a random location is a difficult task without a sight of the Ag substrate during the measurement of STM. One requires a reference of the Ag substrate to do so. The measured apparent height of NaCl layers is not a pure multiplication of single thicknesses. Because NaCl layers are dielectric, the

apparent thickness per ML observed by STM decreases with increasing thickness [16, 166]. Also, the apparent height of NaCl varies depending on tunneling conditions, such as bias voltage and tip conditions, to a large degree [163]. It is possible to use image potential state spectra to determine the thickness on layers without a substrate for comparison, if one has established a database of the spectra for the full range of the thicknesses. However this would require a consistent and good tip condition which is not easily available during the course of scanning on insulating layers. We have tried this approach but no consistent results have been obtained yet.

On top of NaCl, we further deposit Pb by thermal evaporation. By varying the substrate temperature and coverage of Pb, we can control the size distribution of Pb islands. In Fig. 4.5(a), we merely deposit a higher coverage of Pb to obtain larger Pb islands than in Fig. 4.5(b). During each measurement, specific triangular islands like those observed in Fig. 4.5 were selected for further measurements. In Fig. 4.5(a), the length of the equilateral triangular island is in the range of $25 - 60 \text{ nm}$, and in Fig. 4.5(b), $\leq 10 \text{ nm}$.

We expect to produce larger islands than those in Fig. 4.5(a) by increasing the substrate temperature. However for the interest of probing properties in the Coulomb regime, smaller islands are preferred. The size of the smallest triangular island we can produce is around 5 nm in length. One should be aware that the size of the islands is comparable to the dimension of the tip apex. Most of the islands appear in an almost perfect equilateral triangular shape, although one needs a very sharp tip to appreciate its well-defined geometry. With good tip conditions like the one we have in Fig. 4.5(b), one can observe nice triangular islands such as the one we circled. For a blunt tip, one can only observe a triangular shape with rounded edges because the tip radius is convoluted with the geometrical island size yielding the apparent shape.

4.3.2 Spectra of the NaCl surfaces

In the double barrier tunneling junction (DBTJ) shown in Fig. 4.2, we consider that the band gap of the NaCl layers being large enough to cover the voltage range where we measure our spectra. A bulk NaCl crystal is a wide band gap dielectric material with a band gap in the range of $8.5 - 9 \text{ eV}$ ($E_g = 9.0 \text{ eV}$ in [167] and $E_g = 8.5 \text{ eV}$ in [168, 169]). For ultrathin NaCl films, the band gap is reported to be a close to the bulk value [166].

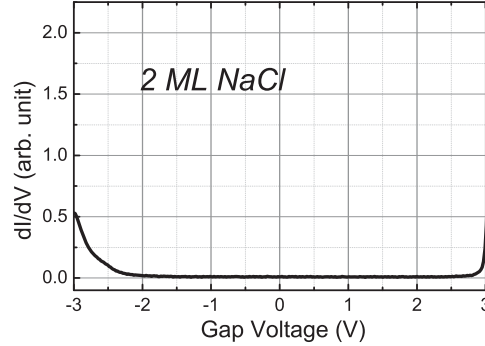


Figure 4.6: dI/dV spectra of a 2 ML NaCl layer on Ag(111). A gap between $\sim -2.5 - 3$ V is visible.

In Fig. 4.2, we indicated the conduction band (CB) of an NaCl ultrathin film which is a little above its work function following the suggestions in [16, 139, 170]. Theoretical investigation also confirmed that the surface work function of NaCl ultrathin film is lower than the bulk value, and that the value approaches the bulk value at higher thickness. The obtained work function value of 1 – 3 ML of NaCl on Ag(100) is 3.2 eV by STM [16] and 3.5 eV by UPS [16, 171].

Figure 4.6 shows a dI/dV spectra measured on top of a 2 ML NaCl film, where an energy between $\simeq -2.5 \sim 3.0$ eV is revealed. In Fig. 4.6, the edge of the gap at 3.2 eV is already close to the conduction band of bulk NaCl [171]. The exponential increase below -2.5 eV is consistent with the *ab initio* calculations of local density of states [166]. It is also consistent with the calculated value $\Delta E = 2.5$ eV that is between the Fermi level (E_F) of the metallic substrate and conduction band of an ultrathin NaCl film [172]. Fig. 4.6 emphasizes that the energy gap of NaCl covers well the range (within ± 2 eV) of our dI/dV spectra of the metallic islands on NaCl.

4.4 STS of metallic Coulomb islands

The tunneling spectra measured on the decoupled metallic Coulomb islands will be presented in this section.

4.4.1 From Coulomb blockade to Coulomb staircase

The tunneling spectra could be a simple Coulomb gap or a staircase depending on the conditions of the Coulomb island. Coulomb staircases are observed in a DBTJ system with

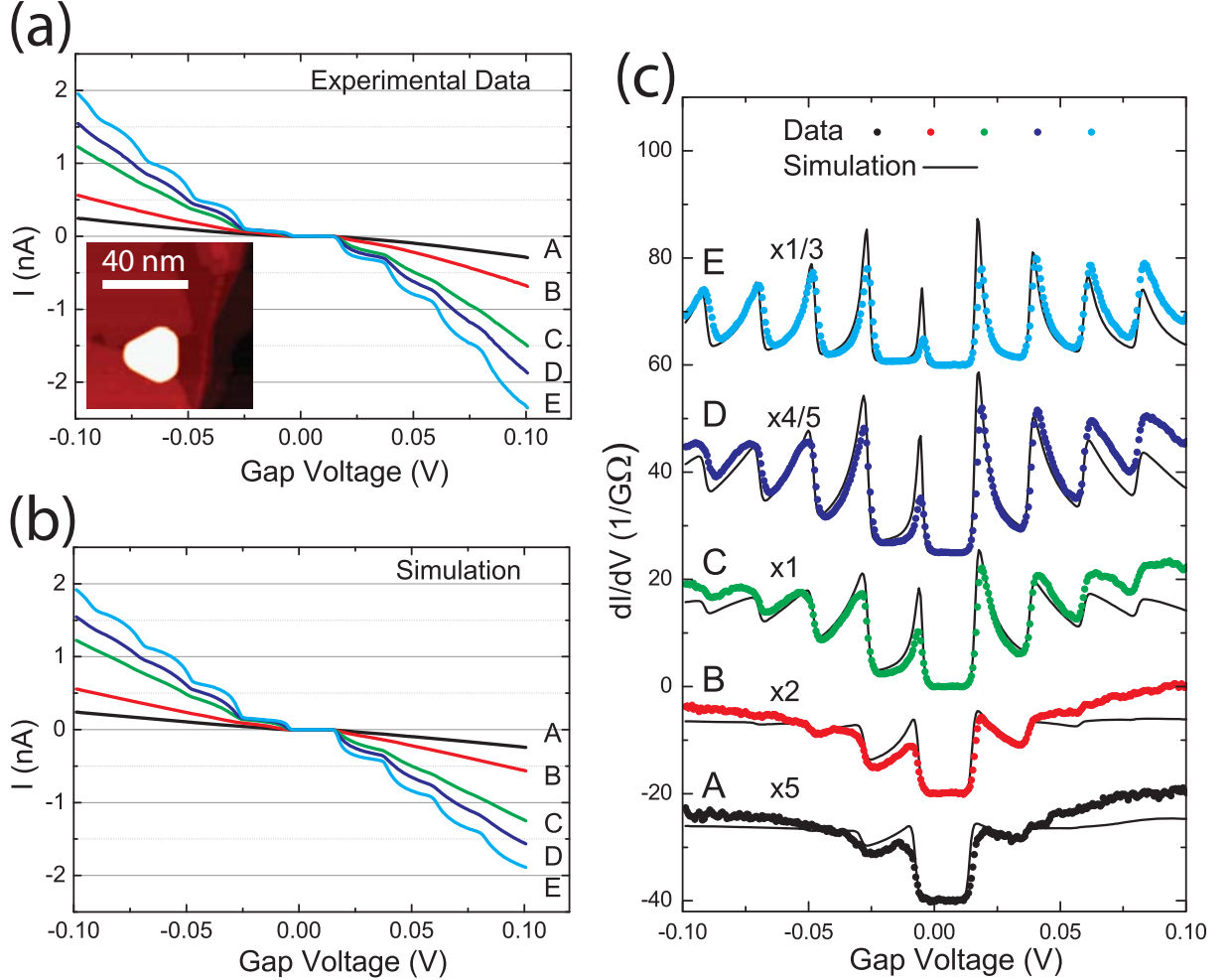


Figure 4.7: Evolution of Coulomb blockade to Coulomb staircase with experimental STS data and simulation. (a) Experimental data of $I(V)$. The tunneling spectra are taken on an island with varying setup current. The length of the island, which is shown in the inset, is $14 nm$ with height $11 ML$. (b) Simulation of $I(V)$. (c) Experimental data (dots) and simulation (black line) of dI/dV . The spectra are offset for clarity since $dI/dV(0V) = 0$ for all spectra. The 5 sets of curves (A-E) in (c) are the differential conductance corresponding to each curve. Experimental dI/dV are measured by the lock-in technique. The parameters of the simulation: $R_{sub} = 39 M\Omega$, $C_{sub} = 7.46 aF$ and $C_{tip} = 0.7 aF$ throughout A-E. $R_{tip,A} = 300 M\Omega$ and $Q_{0,A} = -0.15 e$; $R_{tip,B} = 105 M\Omega$ and $Q_{0,B} = -0.2 e$; $R_{tip,C} = 26 M\Omega$ and $Q_{0,C} = -0.26 e$; $R_{tip,D} = 13 M\Omega$ and $Q_{0,D} = -0.26 e$; $R_{tip,E} = 4.5 M\Omega$ and $Q_{0,E} = -0.28 e$.

both barriers having high resistance and an asymmetric resistance ratio, and a Coulomb gap is observed the otherwise. In Fig. 4.7, we show the evolution from a Coulomb blockade to a Coulomb staircase by simply measuring the spectra with varying initial current. The size of the island, indicated by the length of the equilateral triangle shown in the inset, is $l = 14 \text{ nm}$. An simulation of a similar case is shown in Fig. 4.3. The dI/dV curves measured via lock-in have been calibrated to match the numerical dI/dV curves.

The comparison of the experimental data and the simulated results of both $I(V)$ (by Fig. 4.7(a) and Fig. 4.7(b)) and dI/dV (Fig. 4.7(c)) shows that, we qualitatively reproduce the experimental results with the simulation by varying the resistance between the tip and the island (R_{tip}). This variation is consistent with the experimental condition because we are just varying the initial tunneling current between these curves. In general, R_{tip} decays exponentially with d_{ts} whereas C_{tip} decays linearly. C_{tip} should also vary as we change d_{ts} although to a lesser extent compared to R_{tip} . We indeed have an observation of C_{tip} as a function of d_{ts} in Fig. 4.9. Because the variation is small enough to be neglect, we treat C_{tip} as a constant in the simulation.

A quantitative comparison of calculations and data in Fig. 4.7 shows that the non-linear effect of the conductance is strong. This is not surprising because the tail of a peak of quantum well states near E_F will give a strong background on the spectra. Indeed, for this 11 ML island, there is a QWS peak at $+0.2 \text{ eV}$. Therefore, a quantitative fitting for the spectra must include the DOS of the sample in addition to the orthodox theory. An inclusion of the island DOS and the tunneling transmission coefficient is possible by a more sophisticated theory [158]. Amman *et al.* [173] observed a similar behavior for amorphous metal particles .

If the conditions of the DBTJ are appropriate, we can observe the features of both C_{tip} and C_{sub} at the same time. In Fig. 4.8, STS observations of both C_{tip} and C_{sub} are shown. In Fig. 4.8(a), three spectra with three different Q_0 are obtained on the same island. The Q_0 of the island is changed by applying a $\pm 5 \text{ V}$ bias voltage pulse on the island. It has been proposed [173] that the Q_0 originates from the polarization of the dielectric layers. This observation confirmed this speculation.

As we observe the peaks of C_{tip} , if we approach the tip closer to the island, we should observe C_{tip} to become larger. We demonstrate this in Fig. 4.9(b), the separation of the

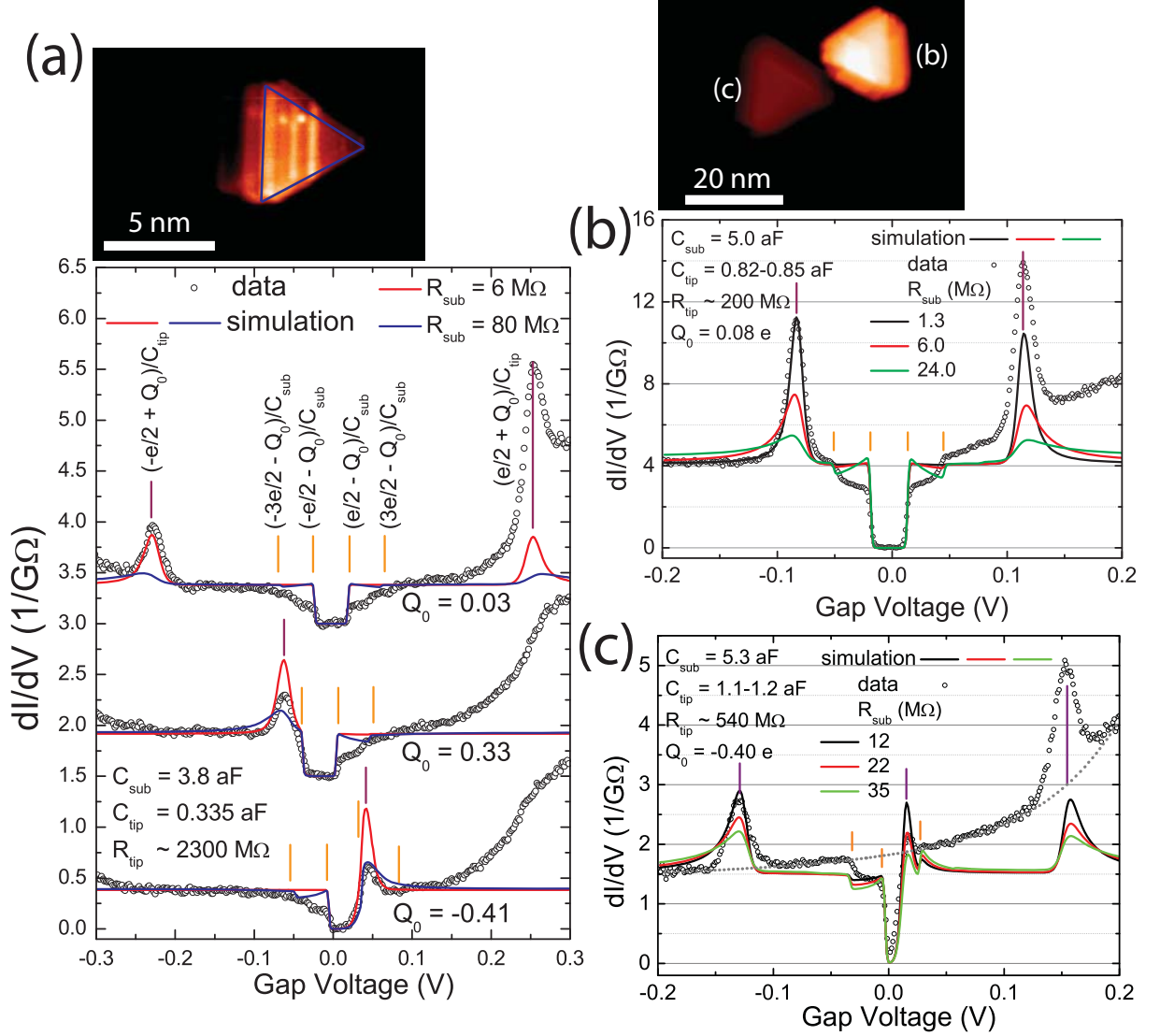


Figure 4.8: dI/dV spectra showing both C_{sub} and C_{tip} , with varying Q_0 . (a) Three spectra measured on the same island with corresponding simulations. We change the residual charge (Q_0) of the island by using a bias voltage pulse. The length of the equilateral triangular island is 7.9 nm . The variation of Coulomb energy concerning C_{sub} and C_{tip} as a function of Q_0 agrees with orthodox theory. (b-c) Additional examples of dI/dV spectra showing both C_{sub} and C_{tip} from two separated islands. The lengths of the equilateral triangular islands are 16 nm in (b) and 16.5 nm in (c). A background, shown by a grey dashed line in (c), originate from the tail of a quantum well states peak at $\sim 0.25 \text{ eV}$ of this 13 ML island. See Fig. 2.11. Although the simulation agrees well with that data qualitatively, we note that the simulation failed to describe the behavior of the spectra quantitatively, which can be observed clearly from the spectra in (b) for the parts of the second step of C_{sub} .

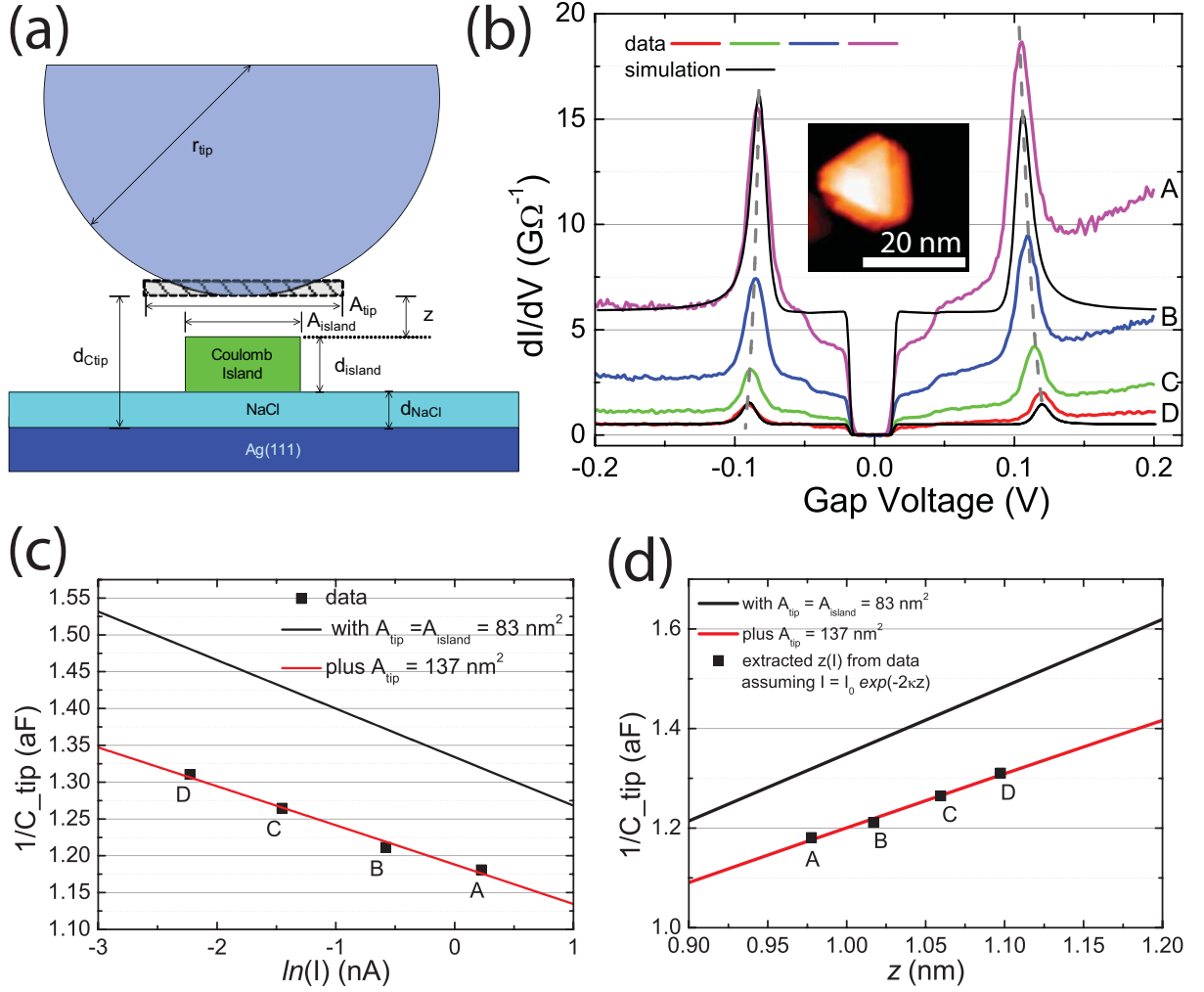


Figure 4.9: C_{tip} becomes larger as the tip is brought closer to the island. Using Coulomb staircase showing C_{tip} , we extract the relationship between C_{tip} and z obtained by varying the tunneling current. (a) The model we employed to extract z from the values of C_{tip} and I . A proposed effective tip area A_{tip} is taken for the calculations of C_{tip} using parallel plate capacitors methods. (b) dI/dV spectra featuring both C_{tip} and C_{sub} . By approaching the tip to the island, the value of C_{tip} decreases (as a of the increased separation of the two C_{tip} peaks) from spectra A to spectra D. The grey dashed curve illustrated this trend. The length of the equilateral triangular island is 16 nm . The gap around E_F comes from C_{sub} and the separation of the two peaks gives us the value of C_{tip} . The fitting curves follow Eq. (4.16) and Eq. (4.17). The parameters of the simulation in (b)– A curve: $C_{sub} = 5.0\text{ aF}$, $C_{tip} = 0.77\text{ aF}$, $R_{sub} = 5\text{ M}\Omega$, $R_{tip} = 1700\text{ M}\Omega$, $Q_0 = 0.07\text{ e}$; D curve: $C_{sub} = 5.0\text{ aF}$, $C_{tip} = 0.86\text{ aF}$, $R_{sub} = 1.0\text{ M}\Omega$, $R_{tip} = 145\text{ M}\Omega$, $Q_0 = 0.062\text{ e}$. The fitting curves follow Eq. (4.16) and Eq. (4.17). The black curves in (c) and (d) are calculated by considering only the capacitance from A_{island} .

two peaks at each curve determine C_{tip} and the gap at the Fermi energy determine C_{sub} . In Fig. 4.9(a), the model we use for the calculations of C_{tip} is shown. It is assumed that we used a hemispherical tip with radius r_{tip} much larger than the size of the island. For convenience, we model the effective tip area A_{tip} by assuming a flat metallic electrode with this size A_{tip} to replace the hemisphere tip. In this way, we can calculate C_{tip} using the parallel plate capacitance method without the complications of calculations of an electric field in an asymmetric geometry. Beside the capacitance between the metallic island and the tip, we include the capacitance between the tip and the substrate which includes the vacuum and NaCl layers. In this case, A_{island} is always smaller than A_{tip} . The value of C_{tip} can be written as:

$$C_{tip} = C_{NaCl} + C_{island} = \frac{\epsilon_0(A_{tip} - A_{island})}{d_{Ctip} - d_{NaCl}(1 - 1/\epsilon_r)} + \epsilon_0 \frac{A_{island}}{z} \quad (4.16)$$

We use $\epsilon_r = 3.2$ for the dielectric constant of NaCl [16] and 0.56 nm (2 ML) for the thickness. Moreover, we consider the relation of current to tunneling distance $I(z)$ by

$$I(z) = I_0 \exp(-2\kappa z) \quad , \text{ where} \quad \kappa = \frac{\sqrt{2m(\phi - E)}}{\hbar} \quad (4.17)$$

We assumed here a work function of $\phi = 4 \text{ eV}$. Given a series of measurement of C_{tip} and I , we fit the data by Eq. (4.16) and Eq. (4.17). One can limit fitting parameters to 2 parameters only, A_{tip} and I_0 . z can be calculated as a by-product.

Figure 4.9(b) shows four dI/dV tunneling spectra with decreasing initial tunneling current from curve A to D. From A to D, we brought the tip farther to the island by decreasing the initial current, that causes smaller C_{tip} and hence larger separation between the peaks. The grey dashed line in Fig. 4.9(b) illustrates this trend. This relation is further confirmed in Fig. 4.9(c-d), which shows $1/C_{tip}$ correlating almost linearly to $\ln(I)$ and z . By fitting the four data points by Eq. (4.16) and Eq. (4.17), we further extract the value of the distance between the tip and the island (z). The agreement of the data and the fit, and the reasonable z value, show that the model is sufficient in this situation.

4.5 Conclusions and outlook

In this chapter, we illustrated the preliminary work on the transport properties of single crystalline metallic quantum dots in the Coulomb regime. Small Pb islands with well-defined geometries are grown on crystalline NaCl layers on Ag(111) substrates. With the ability of recognizing the size of the islands by STM, tunneling spectra obtained at 4.6 K on the nanocrystals exhibit clear Coulomb blockade and Coulomb staircases. The tunneling spectra can be explained by the semi-classical orthodox theory qualitatively despite minor quantitative deviations. The parameters of the DBTJ, the resistances, capacitances, and the residual charges, can be determined from the simulations. By approaching the tip toward the island, we observed the evolution in the tunneling spectra from Coulomb blockade to Coulomb staircase, as well as the change of the tip capacitances.

For future work, we have observed fine structures in the dI/dV spectra showing a Coulomb staircase, which is associated to the discrete levels due to lateral confinement of electrons in the nanostructures. A size-dependent analysis of these energy levels is in progress. We have also observed local variations of the tunneling spectra on the flat top Coulomb islands, suggesting a variation of residual charges Q_0 in the island. The residual charge in the Coulomb island, induced by the polarization of the dielectric layers, is distributed in a profile depending on the charge distribution and on the contour of the island. Seeming to contradict the fact that the screening length of a metal is around few Angstroms, the reason for the local variation of the residual charge is still an open question.

For the previous planar junction experiments, the size and shape of the particle in the DBTJ cannot be determined very precisely. However, in this system, not only the size and shape are well-defined but also can be well determined by STM. This would significantly reduce the uncertainties for estimating the energy spacing ΔE , dimensional conductance or the Thouless energy [174]. The Thouless energy is proportional to the inversed lifetime of the electrons in the energy levels due to the confinement, *i.e.* the linewidth of the energy levels. The superconducting properties have been investigated in small particles by Black *et al.* [175] and a *number parity* property is found for the particles. Experiments of isolated superconducting islands would be interesting for observing the pairing correlation on islands with different parity simultaneously. Theories also [136] suggest that for small

metallic particles containing magnetic Kondo impurities, the Kondo resonance is strongly affected in a parity-dependent way – another experiment fits STM’s strength.

Single electron tunneling for a single crystalline nanostructure with specific size is a difficult task in the previous planar junction studies. Based on studies done by the planar tunneling junctions, we believe future work by STM/STS will give further advantages on studying the mesoscopic physics of nanostructures.

Appendix A

Table of Useful Parameters

Table A.1: These are the some useful parameters and their values in this thesis.

Quantity	Symbol	Value	Unit	Notes
Boltzmann's constant	k_B	8.617	$10^{-5} eV K^{-1}$	[176]
$k_B T$ with $T = 4.2 K$	$k_B T$	3.62	$10^{-4} eV$	
electron charge	e	1.60219	$10^{-19} coulomb$	[176]
permittivity of vacuum	ϵ_0	8.854	$10^{-12} F/m$	
step height of Pb(111)	d	0.286	nm	[25]
lattice parameter of Pb (fcc)	a	0.495	nm	[177]
Fermi energy of Pb	E_F	9.47	eV	^a
Fermi wave length of Pb	λ_F	3.94	$10^{-10} m$	[178]
Fermi velocity of Pb	v_F	1.83	$10^6 m/sec$	^a
r_s of Pb	r_s	1.22	\AA	^a
SC ^b gap of Pb	$2\Delta_{bulk}(0 K)$	2.6	meV	
SC critical temperature of Pb	$T_{C,bulk}$	7.2	K	[177]
$2\Delta/k_B T_c$ of Pb	$2\Delta/k_B T_c$	4.19		
SC coherence length of Pb	$\xi(0 K)$	82	nm	[177]
SC penetration depth of Pb	$\lambda(0 K)$	39	nm	[177]
Debye temperature of Pb	Θ_D	105	K	[78]
Debye Energy of Pb	E_D	9.0	meV	[78]
$e-ph$ coupling constant of Pb	λ	1.55	N/A	[177]
lattice parameter of NaCl	a	5.64	\AA	^c [176]
dielectric constant of NaCl	ϵ	5.90	N/A	[176, 179]

^a A value for bulk crystal [176] using free electron gas approximation.

^b SC stands for superconducting/superconductivity.

^c NaCl is in a structure with two interpenetrating FCC structures of Na and Cl. The lattice constant value stands height of 2 ML step height of NaCl(100) film.

Bibliography

- [1] D. A. Thompson and J. S. Best, *IBM J. Res. Dev.*, **2000**, 44(3), 311, *The future of magnetic data storage technology*.
- [2] J. V. Barth, G. Costantini, and K. Kern, *Nature*, **2005**, 437(7059), 671, *Engineering atomic and molecular nanostructures at surfaces*.
- [3] D. M. Eigler and E. K. Schweizer, *Nature*, **1990**, 344(6266), 524, *Positioning single atoms with a scanning tunneling microscopy*.
- [4] W. Chen, T. Jamneala, V. Madhavan, and M. F. Crommie, *Phys. Rev. B*, **1999**, 60(12), R8529, *Disappearance of the Kondo resonance for atomically fabricated cobalt dimers*.
- [5] C. F. Hirjibehedin, C. P. Lutz, and A. J. Heinrich, *Science*, **2006**, 312(5776), 1021, *Spin coupling in engineered atomic structures*.
- [6] J. V. Barth, *Annu. Rev. Phys. Chem.*, **2007**, 58, 375, *Molecular architectonic on metal surfaces*.
- [7] C. J. Chen, *Introduction to Scanning Tunneling Microscopy*; Oxford, New York, 2008.
- [8] Wiesendanger, *Scanning Probe Microscopy and Spectroscopy, Methods and applications*; Cambridge University Press, New York, 1994.
- [9] J.A. Sctrosccio and W.J. Kaiser, *Scanning Tunneling Microscopy*; Vol. 27; Academic Press, San Diego CA, 1993.
- [10] H.-J. Güntherodt and R. Wiesendanger, *Scanning Tunneling Microscopy I, General Principles and Applications to Clean and Adsorbate-covered surfaces*; Springer-Verlag, Berlin, 1991.
- [11] D.A. Bonnell, *Scanning tunneling microscopy and spectroscopy: theory, techniques, and applications*; VCH Publishers Inc., New York, 1993.
- [12] E. L. Wolf, *Principles of Electron Tunneling Spectroscopy*; Oxford University Press, New York, 1985.
- [13] M. Ternes; *Scanning Tunneling Spectroscopy at the Single Atom Scale*; PhD thesis, **2006**.
- [14] P. Brodard and H. Fukuumura, *Scanning Tunneling Microscopy for Self Assembled Monolayers*; Vol. 14 of *Interface Science and Technology, Advanced Chemistry of Monolayers at Interfaces*; Elsevier, Amsterdam, 2007.

-
- [15] N. D. Lang, *Phys. Rev. B*, **1986**, 34(8), 5947, *Spectroscopy of single atoms in the scanning tunneling microscope*.
 - [16] H. C. Ploigt, C. Brun, M. Pivetta, F. Patthey, and W. D. Schneider, *Phys. Rev. B*, **2007**, 76(19), 195404, *Local work function changes determined by field emission resonances: NaCl/Ag(100)*.
 - [17] R. Gaisch, J. K. Gimzewski, B. Reihl, R. R. Schlittler, M. Tschudy, and W. D. Schneider, *Ultra-microscopy*, **1992**, 42, 1621, *Low-temperature ultra-high-vacuum scanning tunneling microscope*.
 - [18] J. Klein, A. Leger, M. Belin, Defourne.D, and M. J. Sangster, *Phys. Rev. B*, **1973**, 7(6), 2336, *Inelastic-electron-tunneling spectroscopy of metal-insulator-metal junction*.
 - [19] H. Suderow, P. Martinez-Samper, N. Luchier, J. P. Brison, S. Vieira, and P. C. Canfield, *Phys. Rev. B*, **2001**, 64(2), 020503, *Tunneling spectroscopy in the magnetic superconductor TmNi₂B₂C*.
 - [20] W. Ulmer and W. Kaissl, *Phys. Med. Biol.*, **2003**, 48(6), 707, *The inverse problem of a Gaussian convolution and its application to the finite size of the measurement chambers/detectors in photon and proton dosimetry*.
 - [21] Vb. Sandomirskii, *Sov. Phys. JETP*, **1967**, 25(1), 101, *Quantum size effects in a semimetal film*.
 - [22] R. C. Jaklevic, J. Lambe, M. Mikkor, and W. C. Vassell, *Phys. Rev. Lett.*, **1971**, 26(2), 88, *Observation of Electron Standing Waves in a Crystalline Box*.
 - [23] Y. Qi, X. Ma, P. Jiang, S. H. Ji, Y. S. Fu, J. F. Jia, Q. K. Xue, and S. B. Zhang, *Appl. Phys. Lett.*, **2007**, 90(1), 013109, *Atomic-layer-resolved local work functions of Pb thin films and their dependence on quantum well states*.
 - [24] X. C. Ma, P. Jiang, Y. Qi, J. F. Jia, Y. Yang, W. H. Duan, W. X. Li, X. Bao, S. B. Zhang, and Q. K. Xue, *Proc. Natl. Acad. Sci. U. S. A.*, **2007**, 104(22), 9204, *Experimental observation of quantum oscillation of surface chemical reactivities*.
 - [25] W. B. Su, S. H. Chang, W. B. Jian, C. S. Chang, L. J. Chen, and T. T. Tsong, *Phys. Rev. Lett.*, **2001**, 86(22), 5116, *Correlation between quantized electronic states and oscillatory thickness relaxations of 2D Pb islands on Si(111)-(7 x 7) surfaces*.
 - [26] S. C. Li, X. C. Ma, J. F. Jia, Y. F. Zhang, D. M. Chen, Q. Niu, F. Liu, P. S. Weiss, and Q. K. Xue, *Phys. Rev. B*, **2006**, 74(7), 075410, *Influence of quantum size effects on Pb island growth and diffusion barrier oscillations*.
 - [27] F. Calleja, M. C. G. Passeggi, J. J. Hinarejos, A. L. V. de Parga, and R. Miranda, *Phys. Rev. Lett.*, **2006**, 97(18), 186104, *Real-space direct visualization of the layer-dependent roughening transition in nanometer-thick Pb films*.
 - [28] Y. Guo, Y. F. Zhang, X. Y. Bao, T. Z. Han, Z. Tang, L. X. Zhang, W. G. Zhu, E. G. Wang, Q. Niu, Z. Q. Qiu, J. F. Jia, Z. X. Zhao, and Q. K. Xue, *Science*, **2004**, 306(5703), 1915, *Superconductivity modulated by quantum size effects*.
 - [29] J. F. Jia, S. C. Li, Y. F. Zhang, and Q. K. Xue, *J. Phys. Soc. Jpn.*, **2007**, 76(8), 082001, *Quantum size effects induced novel properties in two-dimensional electronic systems: Pb thin films on Si(111)*.

-
- [30] T. C. Chiang, *Surf. Sci. Rep.*, **2000**, 39(7-8), 181, *Photoemission studies of quantum well states in thin films*.
 - [31] M. Milun, P. Pervan, and D. P. Woodruff, *Rep. Prog. Phys.*, **2002**, 65(2), 99, *Quantum well structures in thin metal films: simple model physics in reality?*
 - [32] I. B. Altfeder, K. A. Matveev, and D. M. Chen, *Phys. Rev. Lett.*, **1997**, 78(14), 2815, *Electron fringes on a quantum wedge*.
 - [33] W. B. Jian, W. B. Su, C. S. Chang, and T. T. Tsong, *Phys. Rev. Lett.*, **2003**, 90(19), 196603, *Vertical friedel oscillations in interface-induced surface charge modulations of ultrathin quantum islands*.
 - [34] C. M. Wei and M. Y. Chou, *Phys. Rev. B*, **2002**, 66(23), 233408, *Theory of quantum size effects in thin Pb(111) films*.
 - [35] Z. Y. Zhang, Q. Niu, and C. K. Shih, *Phys. Rev. Lett.*, **1998**, 80(24), 5381, *"Electronic growth" of metallic overlayers on semiconductor substrates*.
 - [36] M. M. Ozer, Y. Jia, B. Wu, Z. Y. Zhang, and H. H. Weitering, *Phys. Rev. B*, **2005**, 72(11), 4, *Quantum stability and reentrant bilayer-by-bilayer growth of atomically smooth Pb films on semiconductor substrates*.
 - [37] D. Barredo, F. Calleja, P. Nieto, J. J. Hinarejos, G. Laurent, A. L. V. de Parga, D. Farias, and R. Miranda, *Adv. Mater.*, **2008**, 20(18), 3492, *A quantum-stabilized mirror for atoms*.
 - [38] M. H. Upton, C. M. Wei, M. Y. Chou, T. Miller, and T. C. Chiang, *Phys. Rev. Lett.*, **2004**, 93(2), 026802, *Thermal stability and electronic structure of atomically uniform Pb films on Si(111)*.
 - [39] J. J. Paggel, T. Miller, and T. C. Chiang, *Science*, **1999**, 283(5408), 1709, *Quantum-well states as Fabry-Perot modes in a thin-film electron interferometer*.
 - [40] Y. F. Zhang, J. F. Jia, T. Z. Han, Z. Tang, Q. T. Shen, Y. Guo, Z. Q. Qiu, and Q. K. Xue, *Phys. Rev. Lett.*, **2005**, 95(9), 096802, *Band structure and oscillatory electron-phonon coupling of Pb thin films determined by atomic-layer-resolved quantum-well states*.
 - [41] P. S. Kirchmann, M. Wolf, J. H. Dil, K. Horn, and U. Bovensiepen, *Phys. Rev. B*, **2007**, 76(7), 075406, *Quantum size effects in Pb/Si(111) investigated by laser-induced photoemission*.
 - [42] B. S. Swartzentruber, Y. W. Mo, M. B. Webb, and M. G. Lagally, *J. Vac. Sci. Technol. A-Vac. Surf. Films*, **1989**, 7(4), 2901, *Scanning tunnelling microscopy studies of structure disorder and steps on Si surfaces*.
 - [43] I. B. Altfeder, D. M. Chen, and K. A. Matveev, *Phys. Rev. Lett.*, **1998**, 80(22), 4895, *Imaging buried interfacial lattices with quantized electrons*.
 - [44] H. H. Weitering, D. R. Heslinga, and T. Hibma, *Phys. Rev. B*, **1992**, 45(11), 5991, *Structure and growth of epitaxial Pb on Si(111)*.
 - [45] I. S. Hwang, R. E. Martinez, C. Liu, and J. A. Golovchenko, *Surf. Sci.*, **1995**, 323(3), 241, *High coverage phases of Pb on the Si(111) surface - structures and phase-transitions*.
 - [46] M. Hupalo, T. L. Chan, C. Z. Wang, K. M. Ho, and M. C. Tringides, *Phys. Rev. B*, **2002**, 66(16),

- 161410, *Atomic models, domain-wall arrangement, and electronic structure of the dense Pb/Si(111)-root 3×3 phase*.
- [47] P. Czoschke, H. Hong, L. Basile, and T. C. Chiang, *Phys. Rev. B*, **2005**, 72(7), 075402, *Quantum size effects in the surface energy of Pb/Si(111) film nanostructures studied by surface x-ray diffraction and model calculations*.
- [48] P. Czoschke, H. Hong, L. Basile, and T. C. Chiang, *Phys. Rev. B*, **2005**, 72(3), 035305, *Surface X-ray-diffraction study and quantum well analysis of the growth and atomic-layer structure of ultrathin Pb/Si(111) films*.
- [49] I. Brihuega, O. Custance, R. Perez, and J. M. Gomez-Rodriguez, *Phys. Rev. Lett.*, **2005**, 94(4), 046101, *Intrinsic character of the (3×3) to $(\text{root } 3 \times \text{root } 3)$ phase transition in Pb/Si(111)*.
- [50] S. Brochard, E. Artacho, O. Custance, I. Brihuega, A. M. Baro, J. M. Soler, and J. M. Gomez-Rodriguez, *Phys. Rev. B*, **2002**, 66(20), 205403, *Ab initio calculations and scanning tunneling microscopy experiments of the Si(111)- $(\text{root } 7 \times \text{root } 3)$ -Pb surface*.
- [51] M. Yakes, V. Yeh, M. Hupalo, and M. C. Tringides, *Phys. Rev. B*, **2004**, 69(22), 224103, *Self-organization at finite temperatures of the devil's staircase in Pb/Si(111)*.
- [52] J. Slezak, P. Mutombo, and V. Chab, *Phys. Rev. B*, **1999**, 60(19), 13328, *STM study of a Pb/Si(111) interface at room and low temperatures*.
- [53] I. S. Hwang, S. H. Chang, C. K. Fang, L. J. Chen, and T. T. Tsong, *Phys. Rev. Lett.*, **2004**, 93(10), 106101, *Observation of finite-size effects on a structural phase transition of 2D nanoislands*.
- [54] O. Custance, J. M. Gomez-Rodriguez, A. M. Baro, L. Jure, P. Mallet, and J. Y. Veuillen, *Surf. Sci.*, **2001**, 482, 1399, *Low temperature phases of Pb/Si(111)*.
- [55] L. Seehofer, G. Falkenberg, D. Daboul, and R. L. Johnson, *Phys. Rev. B*, **1995**, 51(19), 13503, *Structure study of the close-packed 2-dimensional phase of Pb on Ge(111) and Si(111)*.
- [56] M. Hupalo, J. Schmalian, and M. C. Tringides, *Phys. Rev. Lett.*, **2003**, 90(21), 216106, *"Devil's staircase" in Pb/Si(111) ordered phases*.
- [57] K. Horikoshi, X. Tong, T. Nagao, and S. Hasegawa, *Phys. Rev. B*, **1999**, 60(19), 13287, *Structural phase transitions of Pb-adsorbed Si(111) surfaces at low temperatures*.
- [58] I. B. Altfeder, V. Narayanamurti, and D. M. Chen, *Phys. Rev. Lett.*, **2002**, 88(20), 206801, *Imaging subsurface reflection phase with quantized electrons*.
- [59] J. A. Carlisle, T. Miller, and T. C. Chiang, *Phys. Rev. B*, **1992**, 45(7), 3400, *Photoemission-study of the growth, desorption, Schottky-barrier formation, and atomic-structure of Pb on Si(111)*.
- [60] P. B. Howes, K. A. Edwards, D. J. Hughes, J. E. Macdonald, T. Hibma, T. Bootsma, and M. A. James, *Phys. Rev. B*, **1995**, 51(24), 17740, *Influence of interfacial atomics-structure on the Schottky-barrier height of Si(111)-Pb*.
- [61] P. B. Howes, K. A. Edwards, D. J. Hughes, J. E. Macdonald, T. Hibma, T. Bootsma, and M. A. James, *Surf. Sci.*, **1995**, 331, 646, *A surface X-ray-diffraction study of the Si(111)-Pb buried interface*.

-
- [62] P. B. Howes, K. A. Edwards, J. E. Macdonald, T. Hibma, T. Bootsma, M. A. James, and C. L. Nicklin, *Surf. Rev. Lett.*, **1998**, 5(1), 163, *The atomic structure of the Si(111)-Pb buried interface grown on the Si(111)-(root 3 x root 3)-Pb reconstruction.*
 - [63] M. H. Upton, T. Miller, and T. C. Chiang, *Appl. Phys. Lett.*, **2004**, 85(7), 1235, *Absolute determination of film thickness from photoemission: Application to atomically uniform films of Pb on Si.*
 - [64] **I. P. Hong**, C. Brun, F. Patthey, I. Y. Sklyadneva, X. Zubizarreta, R. Heid, V. M. Silkin, P. M. Echenique, K. P. Bohnen, E. V. Chulkov, and W. D. Schneider, *Phys. Rev. B*, **2009**, 80(8), 081409, *Decay mechanisms of excited electrons in quantum-well states of ultrathin Pb islands grown on Si(111): Scanning tunneling spectroscopy and theory.*
 - [65] S. Perraud, K. Kanisawa, Z. Z. Wang, and T. Fujisawa, *Phys. Rev. B*, **2007**, 76(19), 195333, *Imaging the percolation of localized states in a multisubband two-dimensional electronic system subject to a disorder potential.*
 - [66] L. C. Davis, R. C. Jaklevic, and J. Lambe, *Phys. Rev. B*, **1975**, 12(2), 798, *Theory of standing waves in electron tunneling.*
 - [67] J. H. Dil, J. W. Kim, T. Kampen, K. Horn, and Arhf Ettema, *Phys. Rev. B*, **2006**, 73(16), 161308, *Electron localization in metallic quantum wells: Pb versus In on Si(111).*
 - [68] N. Miyata, K. Horikoshi, T. Hirahara, S. Hasegawa, C. M. Wei, and I. Matsuda, *Phys. Rev. B*, **2008**, 78(24), 6, *Electronic transport properties of quantum-well states in ultrathin Pb (111) films.*
 - [69] G. Beuermann, *Z. Phys. B-Condens. Mat.*, **1981**, 44(1-2), 29, *On the directional selectivity of tunneling experiments.*
 - [70] Jędrzej Schmeidel, Herbert Pfnur, and Christoph Tegenkamp, *Phys. Rev. B*, **2009**, 80(11), 115304, *Coulomb blockade effects in Ag/Si(111): The role of the wetting layer.*
 - [71] S. Crampin, *Surf. Sci.*, **2006**, 600, 4280, *Influence of the tip of the scanning tunneling microscope on surface electron lifetimes.*
 - [72] P. M. Echenique and J. B. Pendry, *J. Phys. C Solid State*, **1978**, 11, 2065, *The existence and detection of Rydberg states at surfaces.*
 - [73] N. V. Smith, P. Thiry, and Y. Petroff, *Phys. Rev. B*, **1993**, 47(23), 15476, *Photoemission linewidths and quasi-particle lifetimes.*
 - [74] E. D. Hansen, T. Miller, and T. C. Chiang, *Phys. Rev. Lett.*, **1998**, 80(8), 1766, *Observation of photoemission line widths narrower than the inverse lifetime.*
 - [75] P. S. Kirchmann and U. Bovensiepen, *Phys. Rev. B*, **2008**, 78(3), 035437, *Ultrafast electron dynamics in Pb/Si(111) investigated by two-photon photoemission.*
 - [76] J. T. Li, W. D. Schneider, R. Berndt, O. R. Bryant, and S. Crampin, *Phys. Rev. Lett.*, **1998**, 81(20), 4464, *Surface-state lifetime measured by scanning tunneling spectroscopy.*
 - [77] D. Wegner, A. Bauer, and G. Kaindl, *Phys. Rev. Lett.*, **2005**, 94(12), 126804, *Electronic structure and dynamics of quantum-well states in thin Yb metal films.*

-
- [78] G. Grimvall, *The Electron-Phonon Interaction in Metals*; North-Holland, New-York, 1981.
 - [79] D. Pines and P. Nozieres, *The Theory of Quantum Liquids*; Vol. 1; Addison-Wesley, Red Wood City, California, 1989.
 - [80] E. V. Chulkov, A. G. Borisov, J. P. Gauyacq, D. Sanchez-Portal, V. M. Silkin, V. P. Zhukov, and P. M. Echenique, *Chem. Rev.*, **2006**, 106(10), 4160, *Electronic excitations in metals and at metal surfaces*.
 - [81] C. Brun, **I. P. Hong**, F. Patthey, I. Y. Sklyadneva, R. Heid, P. M. Echenique, K. P. Bohnen, E. V. Chulkov, and W. D. Schneider, *Phys. Rev. Lett.*, **2009**, 102(20), 207002, *Reduction of the Superconducting Gap of Ultrathin Pb Islands Grown on Si(111)*.
 - [82] J. H. Dil, F. Meier, J. Lobo-Checa, L. Patthey, G. Bihlmayer, and J. Osterwalder, *Phys. Rev. Lett.*, **2008**, 101(26), 266802, *Rashba-Type Spin-Orbit Splitting of Quantum Well States in Ultrathin Pb Films*.
 - [83] L. Burgi, O. Jeandupeux, H. Brune, and K. Kern, *Phys. Rev. Lett.*, **1999**, 82(22), 4516, *Probing hot-electron dynamics at surfaces with a cold scanning tunneling microscope*.
 - [84] V. P. Zhukov, E. V. Chulkov, P. M. Echenique, A. Marienfeld, M. Bauer, and M. Aeschlimann, *Phys. Rev. B*, **2007**, 76(19), 193107, *Excited electron dynamics in bulk ytterbium: Time-resolved two-photon photoemission and GW+T ab initio calculations*.
 - [85] M. Tinkham, *Introduction to Superconductivity*; Dover, New-York, 1996.
 - [86] Y. F. Komnik, E. I. Bukhshta, and K. K. Mankovsk, *Sov. Phys. JETP*, **1970**, 30(5), 807, *Quantum size effects in superconducting Tin films*.
 - [87] M. Strongin, R. S. Thompson, O. F. Kammerer, and J. E. Crow, *Phys. Rev. B*, **1970**, 1(3), 1078, *Destruction of Superconductivity in Disordered Near-Monolayer Films*.
 - [88] R. E. Allen, *Phys. Rev. B*, **1975**, 12(9), 3650, *Superconducting transition-temperature and other properties of thin metallic-films*.
 - [89] M. Yu, M. Strongin, and A. Paskin, *Phys. Rev. B*, **1976**, 14(3), 996, *Consistent calculation of boundary effects in thin superconducting films*.
 - [90] B. G. Orr, H. M. Jaeger, and A. M. Goldman, *Phys. Rev. Lett.*, **1984**, 53(21), 2046, *Transition-temperature oscillations in thin superconducting films*.
 - [91] D. B. Haviland, Y. Liu, and A. M. Goldman, *Phys. Rev. Lett.*, **1989**, 62(18), 2180, *Onset of superconductivity in the two-dimensional limit*.
 - [92] A. M. Goldman and N. Markovic, *Phys. Today*, **1998**, 51(11), 39, *Superconductor-insulator transitions in the two-dimensional limit*.
 - [93] M. Jalochowski and E. Bauer, *Phys. Rev. B*, **1988**, 38(8), 5272, *Quantum size and surface effects in the electrical-resistivity and high-energy electron reflectivity of ultrathin lead films*.
 - [94] M. M. Ozer, J. R. Thompson, and H. H. Weiering, *Nat. Phys.*, **2006**, 2(3), 173, *Hard superconductivity of a soft metal in the quantum regime*.

-
- [95] D. Eom, S. Qin, M. Y. Chou, and C. K. Shih, *Phys. Rev. Lett.*, **2006**, 96(2), 027005, *Persistent superconductivity in ultrathin Pb films: A scanning tunneling spectroscopy study.*
 - [96] T. Nishio, M. Ono, T. Eguchi, H. Sakata, and Y. Hasegawa, *Appl. Phys. Lett.*, **2006**, 88(11), 113115, *Superconductivity of nanometer-size Pb islands studied by low-temperature scanning tunneling microscopy.*
 - [97] J. M. Blatt and C. J. Thompson, *Phys. Rev. Lett.*, **1963**, 10(8), 332, *Shape resonances in superconducting thin films.*
 - [98] F. K. Schulte, *Surf. Sci.*, **1976**, 55(2), 427, *Theory of thin metal-films - electron-density, potentials, and work function.*
 - [99] B. Chen, Z. Y. Zhu, and X. C. Xie, *Phys. Rev. B*, **2006**, 74(13), 132504, *Quantum size effects in thermodynamic superconducting properties of ultrathin films.*
 - [100] T. C. Chiang, *Science*, **2004**, 306(5703), 1900, *Physics - Superconductivity in thin films.*
 - [101] B. Abeles, R. W. Cohen, and G. W. Cullen, *Phys. Rev. Lett.*, **1966**, 17(12), 632, *Enhancement of superconductivity in metal films.*
 - [102] M. Strongin, O. F. Kammerer, H. H. Farrell, and D. L. Miller, *Phys. Rev. Lett.*, **1973**, 30(4), 129, *Superconducting properties of crystalline ultra-thin films.*
 - [103] D. G. Naugle, R. E. Glover, and W. Moormann, *Physica*, **1971**, 55, 250, *Thickness dependence of transition temperature of superconducting films.*
 - [104] A. Yazdani, *Nat. Phys.*, **2006**, 2(3), 151, *Lean and mean superconductivity.*
 - [105] H. H. Weitering, *ChemPhysChem*, **2009**, 0000(00), 1, *The World's Thinnest Superconductor.*
 - [106] T. Nishio, T. An, A. Nomura, K. Miyachi, T. Eguchi, H. Sakata, S. Z. Lin, N. Hayashi, N. Nakai, M. Machida, and Y. Hasegawa, *Phys. Rev. Lett.*, **2008**, 101(16), 167001, *Superconducting Pb Island Nanostructures Studied by Scanning Tunneling Microscopy and Spectroscopy.*
 - [107] T. Cren, D. Fokin, F. Debontridder, V. Dubost, and D. Roditchev, *Phys. Rev. Lett.*, **2009**, 102(12), 4, *Ultimate Vortex Confinement Studied by Scanning Tunneling Spectroscopy.*
 - [108] H. Manoharan, C. Lutz, and D. Eigler, *Unpublished, private communications.*, **1999**, *A perspective on the Role of RF noise in STM Measurements.*
 - [109] S. H. Chang, W. B. Su, W. B. Jian, C. S. Chang, L. J. Chen, and T. T. Tsong, *Phys. Rev. B*, **2002**, 65(24), 6, *Electronic growth of Pb islands on Si(111) at low temperature.*
 - [110] W. B. Su, S. H. Chang, H. Y. Lin, Y. P. Chiu, T. Y. Fu, C. S. Chang, and T. T. Tsong, *Phys. Rev. B*, **2003**, 68(3), 4, *Formation of multilayer two-dimensional Pb Islands on Si(111)7x7 at low temperature: From nucleation to growth.*
 - [111] K. Wang, X. Zhang, M.M.T. Loy, T. C. Chiang, and X. Xiao, *Phys. Rev. Lett.*, **2009**, 102(7), 076801, *Pseudogap Mediated by quantum-Sized Effects in Lead Islands.*
 - [112] J. M. Rowell and L. Kopf, *Phys. Rev.*, **1965**, 137(3A), A907, *Tunneling measurement of phonon spectra and density of states in superconductors.*

-
- [113] R. C. Dynes, V. Narayanamurti, and J. P. Garno, *Phys. Rev. Lett.*, **1978**, 41(21), 1509, *Direct measurement of quasiparticle-lifetime broadening in a strong-coupled superconductor*.
 - [114] J. G. Rodrigo, H. Suderow, and S. Vieira, *Eur. Phys. J. B*, **2004**, 40(4), 483, *On the use of STM superconducting tips at very low temperatures*.
 - [115] R. Heid and K. P. Bohnen, *Phys. Rev. B*, **1999**, 60(6), R3709, *Linear response in a density-functional mixed-basis approach*.
 - [116] B. Meyer, C. Elsasser, and M. Fahnle, **1990**, page 4, *FORTTRAN90 Program for Mixed-Basis Pseudopotential Calculations for Crystals*, Max-Planck-Institut für Metallforschung, Stuttgart.
 - [117] D. Vanderbilt, *Phys. Rev. B*, **1985**, 32(12), 8412, *Optimally smooth norm-conserving pseudopotentials*.
 - [118] L. Hedin and B. I. Lundqvist, *J. Phys. C Solid State*, **1971**, 4(14), 2064, *Explicit Local Exchange-correlated Potentials*.
 - [119] J. Simonin, *Phys. Rev. B*, **1986**, 33(11), 7830, *Surface term in the superconductive Ginzburg-Landau free-energy - application to thin-films*.
 - [120] G. Bergmann and D. Rainer, **1973**, 263(1), 59, *Sensitivity of transition temperature to changes in Alpha-2f Omega*.
 - [121] O. Pfennigstorf, A. Petkova, H. L. Guenter, and M. Henzler, *Phys. Rev. B*, **2002**, 65(4), 045412, *Conduction mechanism in ultrathin metallic films*.
 - [122] Shengyong Qin, Jungdae Kim, Qian Niu, and Chih-Kang Shih, **2009**, 324(5932), 1314, *Superconductivity at the Two-Dimensional Limit*.
 - [123] PG De Gennes, *Rev. Mod. Phys.*, **1964**, 36(1), 225, *Boundary Effects in Superconductors*.
 - [124] M. M. Ozer, Y. Jia, Z. Y. Zhang, J. R. Thompson, and H. H. Weitering, *Science*, **2007**, 316(5831), 1594, *Tuning the quantum stability and superconductivity of ultrathin metal alloys*.
 - [125] A. K. Gupta, L. Cretinon, N. Moussy, B. Pannetier, and H. Courtois, *Phys. Rev. B*, **2004**, 69(10), 4, *Anomalous density of states in a metallic film in proximity with a superconductor*.
 - [126] N. Moussy, H. Courtois, and B. Pannetier, *Europhys. Lett.*, **2001**, 55(6), 861, *Local spectroscopy of a proximity superconductor at very low temperature*.
 - [127] M. A. Sillanpaa, T. T. Heikkila, R. K. Lindell, and P. J. Hakonen, *Europhys. Lett.*, **2001**, 56(4), 590, *Inverse proximity effect in superconductors near ferromagnetic material*.
 - [128] H. R. Zeller and I. Giaever, *Phys. Rev.*, **1969**, 181(2), 789, *Tunneling, zero-bias anomalies, and small superconductors*.
 - [129] J. Lambe and R. C. Jaklevic, *Phys. Rev. Lett.*, **1969**, 22(25), 1371, *Charge-quantization studies using a tunnel capacitor*.
 - [130] T. A. Fulton and G. J. Dolan, *Phys. Rev. Lett.*, **1987**, 59(1), 109, *Observation of single-electron charging effects in small tunnel-junctions*.
 - [131] Lydia L. Sohn, Leo P. Kouwenhoven, and Gerd Schon, *Mesoscopic electron transport*; NATO ASI series. Series E, Applied sciences vol. 345 345 0019079. Kluwer Academic Publishers, Dordrecht,

- 1997; (1996 ; CuraÃ§ao) X, 677 S. "Proceedings of the NATO Advanced Study Institute on Mesoscopic Electron Transport, CuraÃ§ao" Published in cooperation with NATO Scientific Affairs Division".
- [132] B. L. Altshuler, P. A. Lee, and R. A. Webb, *Mesoscopic Phenomena in Solids*; Elsevier, Amsterdam, The Netherlands, 1991.
- [133] I. L. Aleiner, P. W. Brouwer, and L. I. Glazman, *Phys. Rep.-Rev. Sec. Phys. Lett.*, **2002**, 358(5-6), 309, *Quantum effects in Coulomb blockade*.
- [134] G. Schon and A. D. Zaikin, *Phys. Rep.-Rev. Sec. Phys. Lett.*, **1990**, 198(5-6), 237, *Quantum coherent effects, phase-transitions, and the dissipative dynamics of ultra small tunnel-junctions*.
- [135] H. Grabert and M. H. Devoret, *Single Charge Tunneling*; Plenum, New York, 1992.
- [136] J. von Delft and D. C. Ralph, *Phys. Rep.-Rev. Sec. Phys. Lett.*, **2001**, 345(2-3), 61, *Spectroscopy of discrete energy levels in ultrasmall metallic grains*.
- [137] K. K. Likharev, *Proc. IEEE*, **1999**, 87(4), 606, *Single-electron devices and their applications*.
- [138] S. Schintke and W. D. Schneider, *J. Phys.-Condes. Matter*, **2004**, 16(4), R49, *Insulators at the ultra-thin limit: electronic structure studied by scanning tunnelling microscopy and scanning tunnelling spectroscopy*.
- [139] S. Schintke, S. Messerli, M. Pivetta, F. Patthey, L. Libiouille, M. Stengel, A. De Vita, and W. D. Schneider, *Phys. Rev. Lett.*, **2001**, 87(27), 276801, *Insulator at the ultrathin limit: MgO on Ag(001)*.
- [140] Marina Pivetta, Franois Patthey, Massimiliano Stengel, Alfonso Baldereschi, and Wolf-Dieter Schneider, *Phys. Rev. B*, **2005**, 72(11), 115404, *Local work function Moir  pattern on ultrathin ionic films: NaCl on Ag(100)*.
- [141] R. Wilkins, E. Benjacob, and R. C. Jaklevic, *Phys. Rev. Lett.*, **1989**, 63(7), 801, *Scanning-tunneling-microscope observations of Coulomb blockade and oxide-polarization in small metal droplets*.
- [142] N. Oncel, A. S. Hallback, H. J. W. Zandvliet, E. A. Speets, B. J. Ravoo, D. N. Reinhoudt, and B. Poelsema, *J. Chem. Phys.*, **2005**, 123(4), 4, *Coulomb blockade of small Pd clusters*.
- [143] B. Koslowski, C. Dietrich, F. Weigl, and P. Ziemann, *Phys. Rev. B*, **2007**, 75(8), 10, *Dynamic charging at room temperature of Au nanoparticles prepared by a micellar technique*.
- [144] U. Banin, Y. W. Cao, D. Katz, and O. Millo, *Nature*, **1999**, 400(6744), 542, *Identification of atomic-like electronic states in indium arsenide nanocrystal quantum dots*.
- [145] Bing Wang, Haiqian Wang, Huixiang Li, Changgan Zeng, J. G. Hou, and Xudong Xiao, *Phys. Rev. B*, **2000**, 63(3), 035403, *Tunable single-electron tunneling behavior of ligand-stabilized gold particles on self-assembled monolayers*.
- [146] B. Wang, K. D. Wang, W. Lu, H. Q. Wang, Z. Y. Li, J. L. Yang, and J. G. Hou, *Appl. Phys. Lett.*, **2003**, 82(21), 3767, *Effects of discrete energy levels on single-electron tunneling in coupled metal particles*.
- [147] B. Wang, K. D. Wang, W. Lu, J. L. Yang, and J. G. Hou, *Phys. Rev. B*, **2004**, 70(20), 6, *Size-dependent tunneling differential conductance spectra of crystalline Pd nanoparticles*.

-
- [148] O. Millo, D. Katz, Y. W. Cao, and U. Banin, *Phys. Rev. Lett.*, **2001**, 86(25), 5751, *Imaging and spectroscopy of artificial-atom states in core/shell nanocrystal quantum dots*.
 - [149] J. G. A. Dubois, J. W. Gerritsen, S. E. Shafranjuk, E. J. G. Boon, G. Schmid, and H. van Kempen, *Europhys. Lett.*, **1996**, (4), 279, *Coulomb staircases and quantum size effects in tunnelling spectroscopy on ligand-stabilized metal clusters*.
 - [150] R. P. Andres, T. Bein, M. Dorogi, S. Feng, J. I. Henderson, C. P. Kubiak, W. Mahoney, R. G. Osifchin, and R. Reifenberger, *Science*, **1996**, 272(5266), 1323, *"Coulomb staircase" at room temperature in a self-assembled molecular nanostructure*.
 - [151] O. Millo, D. Katz, Y. W. Cao, and U. Banin, *Phys. Rev. B*, **2000**, 61(24), 16773, *Scanning tunneling spectroscopy of InAs nanocrystal quantum dots*.
 - [152] K. Schouteden, N. Vandamme, E. Janssens, P. Lievens, and C. Van Haesendonck, *Surf. Sci.*, **2008**, 602(2), 552, *Single-electron tunneling phenomena on preformed gold clusters deposited on dithiol self-assembled monolayers*.
 - [153] J. G. Hou, B. Wang, J. L. Yang, K. D. Wang, W. Lu, Z. Y. Li, H. Q. Wang, D. M. Chen, and Q. S. Zhu, *Phys. Rev. Lett.*, **2003**, 90(24), 4, *Disorder and suppression of quantum confinement effects in Pd nanoparticles*.
 - [154] A. E. Hanna and M. Tinkham, *Phys. Rev. B*, **1991**, 44(11), 5919, *Variation of the Coulomb staircase in a 2-junction system by fractional electron charge*.
 - [155] D. V. Averin and K. K. Likhrev, *Mesoscopic Phenomena in Solids*, Chapter 6; Vol. 30 of *Modern Problems in Condensed Matter Sciences*; North-Holland, Amsterdam, 1991.
 - [156] D. C. Ralph, C. T. Black, and M. Tinkham, *Phys. Rev. Lett.*, **1997**, 78(21), 4087, *Gate-voltage studies of discrete electronic states in aluminum nanoparticles*.
 - [157] I. O. Kulik and R. I. Shekhter, *Sov. Phys. JETP*, **1975**, 41(2), 308, *Kinetic phenomena and charge discreteness effects in granulated media*.
 - [158] U. Banin and O. Millo, *Annu. Rev. Phys. Chem.*, **2003**, 54, 465, *Tunneling and optical spectroscopy of semiconductor nanocrystals*.
 - [159] W. Hebenstreit, M. Schmid, J. Redinger, R. Podloucky, and P. Varga, *Phys. Rev. Lett.*, **2000**, 85(25), 5376, *Bulk Terminated NaCl(111) on Aluminum: A Polar Surface of an Ionic Crystal?*
 - [160] Bo Li, Angelos Michaelides, and Matthias Scheffler, *Phys. Rev. B*, **2007**, 76(7), 075401, *Density functional theory study of flat and stepped NaCl(001)*.
 - [161] E. Cavar, M. C. Blum, M. Pivetta, F. Patthey, M. Chergui, and W. D. Schneider, *Phys. Rev. Lett.*, **2005**, 95(19), 196102, *Fluorescence and phosphorescence from individual C-60 molecules excited by local electron tunneling*.
 - [162] Frédéric Rossel, Marina Pivetta, François Patthey, and Wolf-Dieter Schneider, *Opt. Express*, **2009**, 17(4), 2714, *Plasmon enhanced luminescence from fullerene molecules excited by local electron tunneling*.

-
- [163] H.-C. Ploigt; *Ultra-thin dielectric layers on Metal Substrates studied by Scanning Tunneling Microscopy and Scanning Tunneling Spectroscopy*; PhD thesis, **2007**.
- [164] J. Kramer, C. Tegenkamp, and H. Pfnur, *J. Phys.-Condes. Matter*, **2003**, 15(38), 6473, *The growth of NaCl on flat and stepped silver surfaces*.
- [165] M. E. Cañas Ventura, W. Xiao, P. Ruffieux, R. Rieger, K. Müllen, H. Brune, and R. Fasel, **2009**, 603(15), 2294, *Stabilization of bimolecular islands on ultrathin NaCl films by a vicinal substrate*.
- [166] W. Hebenstreit, J. Redinger, Z. Horozova, M. Schmid, R. Podloucky, and P. Varga, *Surf. Sci.*, **1999**, 424(2-3), L321, *Atomic resolution by STM on ultra-thin films of alkali halides: experiment and local density calculations*.
- [167] A. Goldmann and E.-E. Koch, *Condensed Matter*; Vol. 23a of *Landolt-Bornstein - Group III Condensed Matter*; Springer-Verlag, 1989.
- [168] R. Haensel, G. Keitel, G. Peters, Schreibe.P, B. Sonntag, and C. Kunz, *Phys. Rev. Lett.*, **1969**, 23(10), 530, *Photoemission measurement on NaCl in photon energy range 32-50 eV*.
- [169] R. T. Poole, J. G. Jenkin, J. Liesegang, and R. C. G. Leckey, *Phys. Rev. B*, **1975**, 11(12), 5179, *Electronic band-structure of Alkali-Halides .1. Experimental parameters*.
- [170] U. Malaske, C. Tegenkamp, M. Henzler, and H. Pfnur, *Surf. Sci.*, **1998**, 408(1-3), 237, *Defect-induced band gap states and the contact charging effect in wide band gap insulators*.
- [171] U. Barjenbruch, S. Folsch, and M. Henzler, *Surf. Sci.*, **1989**, 211(1-3), 749, *Surface-states on epitaxial thin-films of NaCl and KCl*.
- [172] S. Prada, U. Martinez, and G. Pacchioni, *Phys. Rev. B*, **2008**, 78(23), 235423, *Work function changes induced by deposition of ultrathin dielectric films on metals: A theoretical analysis*.
- [173] M. Amman, S. B. Field, and R. C. Jaklevic, *Phys. Rev. B*, **1993**, 48(16), 12104, *Coulomb -blockade spectroscopy of gold particles imaged with scanning-tunneling-microscopy*.
- [174] B. L. Altshuler, Y. Gefen, A. Kamenev, and L. S. Levitov, *Phys. Rev. Lett.*, **1997**, 78(14), 2803, *Quasiparticle lifetime in a finite system: A nonperturbative approach*.
- [175] C. T. Black, D. C. Ralph, and M. Tinkham, *Phys. Rev. Lett.*, **1996**, 76(4), 688, *Spectroscopy of the superconducting gap in individual nanometer-scale aluminum particles*.
- [176] N. W. Ashcroft and N. D. Mermin, *Solid State Physics*; Harcourt Brace College Publishers, New York, 1976.
- [177] C. P. Poole, H. A. Farach, and R. J. Creswick, *Superconductivity*; Academic Press, San Diego, California, 1995.
- [178] M. Jalochowski, H. Knoppe, G. Lilienkamp, and E. Bauer, *Phys. Rev. B*, **1992**, 46(8), 4693, *Photoemission from ultrathin metallic-films - quantum size effect, electron-scattering, and film structure*.
- [179] M. C. Robinson and A. C. H. Hallett, *Can. J. Phys.*, **1966**, 44(10), 2211, *Static dielectric constant of NaCl, KCl, and KBr at temperature between 4.2 degrees K and 300 degrees K*.

Curriculum Vitae

I-Po HONG

- Citizenship: Taiwan
- Date of Birth: September 14, 1976

Education and Research Experiences

STM/STS, tunneling spectra analyzing, low-temperature, ultra-high vacuum, electron and heat transport measurement.

Ph.D.

Oct 2005 to present

- EPFL, Lausanne, Switzerland. Group of Prof. Wolf-Dieter Schneider.
- Thesis Title: *Quantum Size Effects in Metallic Islands: A Scanning Tunneling Microscopy/Spectroscopy Study*.
- Superconducting properties of ultrathin lead film in a layer-by-layer way by STM/STS. Published in *Phys. Rev. Lett.* (2009).
- Analysis of quasiparticle lifetime of quantum well states of ultrathin lead film by STM/STS. Published in *Phys. Rev. B* (2009).
- Coulomb blockade phenomena of metallic islands on insulating layers.

Research assistant

Jan 2001 to Jun 2005

- Academia Sinica, Taipei, Taiwan. Group of Prof. Tien Tzou Tsong. Under the subgroup of Prof. Ing-Shouh Hwang.
- Developed and tested of a homemade STM, including the apparatus and electronics.
- Used STM/STS to study quantum properties of nanostructures on silicon substrates.

Masters

Sep 1998 to Jun 2000

- NSYSU (National Sun Yet-Sen University), Kaohsiung Taiwan. Group of Prof. Hung-Duen Yang.
- Thesis Title: *Transport and Magnetic Properties of $Pr_{1-x}Ba_{2+x}Cu_3O_7$* .
- Results of the thesis is published in *Europhys Lett.* 2002.

- Used X-ray absorption spectra near edge (XANES) spectra and transport measurement to investigate the electronic structure and the superconducting mechanism of cuprate high T_c superconductors.

B.Sc. in Physics

Sep 1994 to Jun 1998

NSYSU, Kaohsiung, Taiwan

Languages

English (fluent) *Chinese* (native) *French* (basic)

Publications during this thesis

- C. Brun, **I. P. Hong**, F. Patthey, I. Y. Sklyadneva, R. Heid, P. M. Echenique, K. P. Bohnen, E. V. Chulkov, and W. D. Schneider, *Phys. Rev. Lett.*, **2009**, 102(20), 207002, *Reduction of the Superconducting Gap of Ultrathin Pb Islands Grown on Si(111)*.
- **I. P. Hong**, C. Brun, F. Patthey, I. Y. Sklyadneva, X. Zubizarreta, R. Heid, V. M. Silkin, P. M. Echenique, K. P. Bohnen, E. V. Chulkov, and W. D. Schneider, *Phys. Rev. B*, **2009**, 80(8), 081409, *Decay mechanisms of excited electrons in quantum-well states of ultrathin Pb islands grown on Si(111): Scanning tunneling spectroscopy and theory*.

Publication in Preparation

- **I. P. Hong**, C. Brun, F. Patthey, and W. D. Schneider, in preparation for *Phys. Rev. Lett.*, *Coulomb blockade of single nanocrystals at the atomic scale*.

List of Publications

1. C. Brun, **I. P. Hong**, F. Patthey, I. Y. Sklyadneva, R. Heid, P. M. Echenique, K. P. Bohnen, E. V. Chulkov, and W. D. Schneider, *Phys. Rev. Lett.*, **2009**, 102(20), 207002, *Reduction of the Superconducting Gap of Ultrathin Pb Islands Grown on Si(111)*.
2. **I. P. Hong**, C. Brun, F. Patthey, I. Y. Sklyadneva, X. Zubizarreta, R. Heid, V. M. Silkin, P. M. Echenique, K. P. Bohnen, E. V. Chulkov, and W. D. Schneider, *Phys. Rev. B*, **2009**, 80(8), 081409, *Decay mechanisms of excited electrons in quantum-well states of ultrathin Pb islands grown on Si(111): Scanning tunneling spectroscopy and theory*.
3. **I. P. Hong**, J. Y. Lin, J. M. Chen, S. Chatterjee, S. J. Liu, Y. S. Gou, and H. D. Yang, *Europhysics Letters*, **2002**, 58(1), 126, *Possible evidence for the existence of the Fehrenbacher-Rice band: O K-edge XANES study on $Pr_{1-x}Ca_xBa_2Cu_4O_8$* .
4. S. S. Weng, **I. P. Hong**, C. F. Chang, H. L. Tsay, S. Chatterjee, H. D. Yang, and J. Y. Lin, *Phys. Rev. B*, **1999**, 59(17), 11205, *Pressure effects on the superconductivity and magnetic order of $Y_{1-x}Pr_xBa_2Cu_4O_8$* .
5. J. M. Chen, S. J. Liu, J. M. Lee, **I. P. Hong**, J. Y. Lin, Y. S. Gou, and H. D. Yang, *Chemical Physics Letters*, **2003**, 370(1-2), 180, *Pr-induced superconductivity suppression in $Y_xPr_{1-x}Ba_2Cu_4O_8$ probed by soft-X-ray absorption spectroscopy: a comparative studies of $Y_xPr_{1-x}Ba_2Cu_4O_8$ and $Y_xPr_{1-x}Ba_2Cu_3O_7$* .
6. J. M. Chen, P. Nachimuthu, J. Y. Lin, **I. P. Hong**, C. F. Chang, and H. D. Yang, *Chemical Physics Letters*, **2001**, 337(1-3), 85, *Origin of size effect on superconductivity in $(R_{0.8}Pr_{0.2})Ba_2Cu_3O_7$ studied by soft X-ray absorption spectroscopy*.
7. S. Chatterjee, P. H. Chou, C. F. Chang, **I. P. Hong**, and H. D. Yang, *Phys. Rev. B*, **2000**, 61(9), 6106, *Lattice effects on the transport properties of $(R, Sr)_3Mn_2O_7$ ($R = La, Eu, \text{ and } Pr$)*.
8. W. H. Li, S. Y. Wu, Y. C. Lin, K. C. Lee, J. W. Lynn, S. S. Weng, **I. P. Hong**, J. Y. Lin, and H. D. Yang, *Phys. Rev. B*, **1999**, 60(6), 4212, *Magnetic ordering in double-chain $PrBa_2Cu_4O_8$* .

9. S. Chatterjee, S. S. Weng, **I. P. Hong**, C. F. Chang, H. D. Yang, and J. Y. Lin, *Physica C-Superconductivity and Its Applications*, **1999**, 312(1-2), 55, *Contributions of CuO_2 planes and CuO chains on the transport properties of $\text{YBa}_2\text{Cu}_4\text{O}_8$.*

Acknowledgements

First of all, I am extremely grateful to Prof. Wolf-Dieter Schneider for supervising this thesis and inspiring me both scientifically and personally. The LPS lab is an excellent place for creative scientific work.

I have great thanks to François Patthey for helps both scientific and experimental. His physics intuition and experimental expertise make working in LPS a privilege for a Ph.D. student.

I am very thankful to Christophe Brun for the guidance through every part of the thesis. The stimulating discussions everyday taught me a lot. Without those, my work in Lausanne would not be half as fruitful.

I am also thankful to Frédéric Rossel for the delightful office environment and many assistance in my daily life. I would also like to thank Marina Pivetta for her often heart-warming help. I also want to thank Pierre Brodard, Hans-Christoph Ploigt for sharing their generous assistance and joy. I have to thank Jean-François Jeanneret and for the helps in the lab during my early days.

Although I would have enjoyed more the life in Lausanne if I could learn to speak French better, still days in Lausanne is a fond and unforgettable memory for me. For this I also owe a lot of thanks to the people around me for many things.

